A Precision Measurement of the Ratio of the Effective Vector to Axial-Vector Couplings of the Weak Neutral Current at the Z^o Pole

by

Manuella Greta Vincter
B. Sc., McGill University, 1990
M. Sc., University of Victoria, 1993

A Dissertation Submitted in Partial Fulfillment of the
Requirements for the Degree of

DOCTOR OF PHILOSOPHY

in the Department of Physics and Astronomy

We accept this dissertation as conforming
to the required standard

Dr. R. K. Keeler, Supervisor (Department of Physics and Astronomy)

Dr. A. Astbury, Departmental Member (Department of Physics and Astronomy)

Dr. G. Beer, Departmental Member (Department of Physics and Astronomy)

Dr. J. M. Roney, Additional Member (Department of Physics and Astronomy)

Dr. P. Wan, Outside Member (Department of Chemistry)

Dr. D. Hanna, External Examiner (Department of Physics, McGill University)

Supervisor: Dr. Richard K. Keeler

ABSTRACT

Parity violating effects of the neutral weak current as seen in the process $e^+e^- \rightarrow Z^0 \rightarrow \tau^+\tau^-$ with the OPAL detector at LEP are presented in this thesis. The unequal coupling of the Z^0 to left-handed and right-handed $e^\pm$ and $\tau^\pm$ produces the tau polarization asymmetries, $\langle \mathrm{P}_\tau \rangle$ and $\mathrm{A}_{\mathrm{pol}}^{\mathrm{FB}}$, that are related to the ratios of the effective vector to axial-vector couplings, $\hat{g}_v^\tau/\hat{g}_a^\tau$ and $\hat{g}_v^e/\hat{g}_a^e$. The values resulting from the analysis described in this thesis are,

$$\langle \mathrm{P}_\tau \rangle = -0.1243 \pm 0.0197 \qquad \text{and} \qquad \mathrm{A}_{\mathrm{pol}}^{\mathrm{FB}} = -0.0931 \pm 0.0189$$

giving the ratios of the effective vector to axial-vector couplings

$$\hat{g}_v^\tau/\hat{g}_a^\tau = 0.0639 \pm 0.0100 \qquad \text{and} \qquad \hat{g}_v^e/\hat{g}_a^e = 0.0639 \pm 0.0127.$$

They are in excellent agreement with previous measurements. These results are consistent with the assumption of lepton universality and so are combined to extract

$$\sin^2\theta_{eff}^{lept} = 0.2340 \pm 0.0020.$$

The parameters presented in this thesis are a significant contribution to the world average values that test the validity of the Standard Model theory of the electroweak interaction.

Examiners:

Dr. R. K. Keeler, Supervisor (Department of Physics and Astronomy)

Dr. A. Astbury, Departmental Member (Department of Physics and Astronomy)

Dr. G. Beer, Departmental Member (Department of Physics and Astronomy)

Dr. J. M. Roney, Additional Member (Department of Physics and Astronomy)

Dr. P. Wan, Outside Member (Department of Chemistry)

Dr. D. Hanna, External Examiner (Department of Physics, McGill University)

Contents

List of Tables

List of Figures

ACKNOWLEDGEMENTS

Many thanks go to Mike Roney for supervising my thesis work. I am grateful to Richard Keeler for the critical reading of this thesis. Finally, I very much appreciated the friendship and support of my OPAL collaborators at CERN.

Chapter 1

Introduction

The Standard Model [1, 2] describes the current understanding of the interactions between matter via the electromagnetic, the strong nuclear, and the weak nuclear forces. The interaction between two particles is explained classically by a potential or field due to one particle acting on another particle. However, this macroscopic description of particle interactions is inadequate when explaining the interactions between elementary point-like particles. A quantum mechanical description is needed. The quantum mechanical interpretation has two particles interacting through the exchange of quanta specific to the type of interaction. These quanta exist for a time governed by their energy through the Heisenberg uncertainty principle $\Delta E \Delta t \geq \hbar$. For example, electromagnetic fields are quantized in the form of photons. The strength of the interaction between particles is determined by the coupling of the exchange quanta to matter and the range of the interaction is limited by the mass of the quanta. This thesis investigates aspects of the coupling of the neutral weak force to matter.

1.1 The Standard Model

The Standard Model makes a clear distinction between matter and the exchange quanta which are the mediators of the interactions. Matter and interactions are classified by spin.

Matter consists of half-integer spin particles called fermions that obey Fermi-Dirac statistics so are subject to the Pauli Exclusion Principle. Quarks, q, and leptons, ℓ, are the fermions believed to be the building blocks of matter (see table 1.1). There are six

Quarks	Charge	Mass (MeV/c^2)	Interaction
u	2/3 e	2-8	EM, strong, weak
c		1000-1600	
t		$(168 - 192) \times 10^3$	
d	-1/3 e	5-15	EM, strong, weak
s		100-300	
b		4100-4500	

Leptons	Charge	Mass (MeV/c^2)	Interaction
e^-	$-e$	$0.51099906 \pm 0.00000015$	EM, weak
μ^-		105.658389 ± 0.000034	
τ^-		$1777.1^{+0.4}_{-0.5}$	
ν_e	0	< 0.0051	Weak
ν_μ		< 0.16	
ν_τ		< 31	

Table 1.1: *Table of quarks and leptons of the Standard Model. The current quark masses and lepton masses are taken from [3].*

types of quarks u, d, s, c, b, and t along with their oppositely charged antiparticle partners $\overline{u}, \overline{d}, \overline{s}, \overline{c}, \overline{b}$, and $\overline{t}$. Three quarks can bind to form baryons such as the proton (uud) or quark-antiquark pairs can bind to form mesons such as the π^+ ($u\overline{d}$). Leptons either can be charged ($e^\pm, \mu^\pm$, and $\tau^\pm$) or neutral (the neutrinos ν_e, ν_μ, and ν_τ and their antiparticle partners $\overline{\nu_e}, \overline{\nu_\mu}$, and $\overline{\nu_\tau}$).

The mediators of the interactions are integer-spin particles called bosons. Bosons obey Bose-Einstein statistics so are not subject to the Pauli Exclusion Principle. The exchange quanta for the electromagnetic interaction is the massless particle called the photon. The weak interaction is mediated by massive charged particles, the $W^\pm$, and a massive neutral particle, the Z^0. The mass of the weak bosons implies a limited range of interaction The exchange of bosons between fermions can be calculated using Feynman diagrams. For example, figure 1.1 shows the Feynman diagrams describing muon decay and $\overline{\nu}_\mu - e^-$ scattering, processes that involve the exchange of a W^- and a Z^0.

The effects of the strong force can be observed in several ways. The confinement

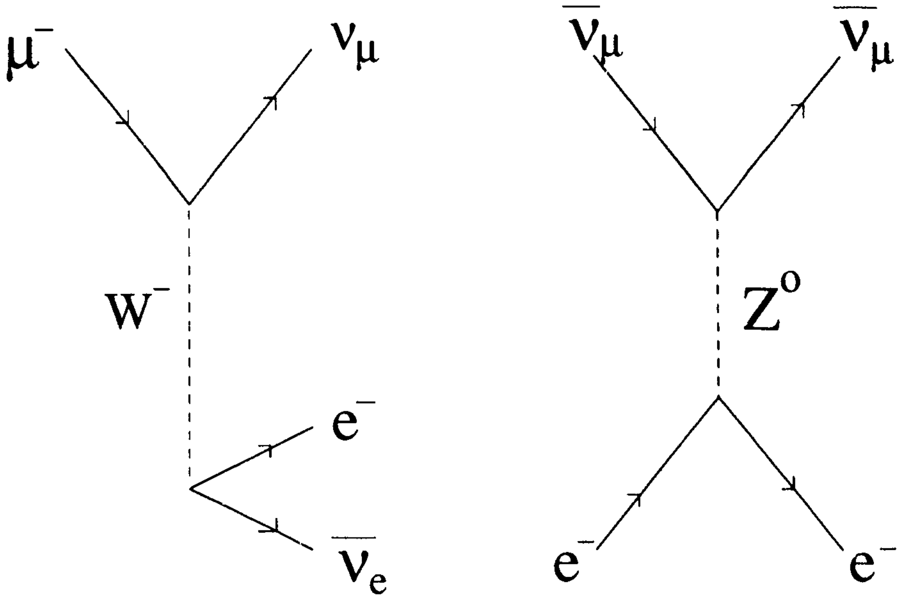

Figure 1.1: *Examples of the charged weak and neutral weak interactions. This figure shows the decay of the muon through W exchange and* $\bar{\nu}_\mu - e^-$ *scattering through* Z^0 *exchange.*

of quarks within the mesons and baryons by the exchange of massless particles called gluons is a manifestation of the "fundamental strong force". Single quarks cannot be extracted from nucleons. They only exist in pairs or triplets. The "residual strong force" is responsible for the binding of protons and neutrons within the nucleus. The force can be described by an effective theory of meson exchange. The mediators of the forces are summarized in table 1.2.

The Standard Model provides mass to the fermions and bosons through the Higgs

Force	Mediator	Mass
EM	γ	0
Weak	$W^\pm, Z^0$	80.33 GeV/c^2, 91.187 GeV/c^2
Strong fundamental	g	0
Strong residual	mesons	$>$ 135 MeV/c^2

Table 1.2: *Table of the mediators of the electromagnetic, weak, and strong forces. Mass values are taken from [3].*

mechanism. This mechanism is based on the idea that there are symmetry relations between the quantum numbers of the quarks and leptons that are broken by choosing an underlying vacuum state that does not preserve the symmetry. The quantum numbers and the symmetry groups will be discussed later in this chapter. As well as giving the particles mass, the Higgs mechanism creates a relationship between the masses of the weak bosons, M_W and M_Z, through the Weinberg mixing angle, θ_W

$$\sin^2\theta_W = 1 - \frac{M_W^2}{M_Z^2} \approx 0.23. \tag{1.1}$$

The Weinberg angle is not predicted by the theory and must be determined experimentally. The Higgs mechanism also results in the existence of a Higgs boson. The mass of the Higgs boson is also not predicted by the theory. It has not been observed yet but its mass, M_H, is expected to be less than 1000 GeV/c^2 and a mass less than 58.4 GeV/c^2 is ruled out by experiment [3].

The interactions between fermions are understood in terms of the exchange of bosons between Dirac currents that represent the fermions. The coupling of bosons to fermions is dependent on the quantum numbers of the fermions such as the charge (q_f). The weak interaction also depends on the helicity of the particle where helicity is the component of the fermion's spin along the direction of motion. Relativistic fermions exist in ±1 helicity states where a positive (negative) helicity fermion is referred to as a right-handed (left-handed) particle.

The coupling strength of bosons to left-handed particles, g_L^f, is not necessarily identical to the coupling strength to right-handed particles, g_R^f. The total coupling strength can be written as

$$g_F\left[g_L^f\gamma^\mu(1-\gamma^5) + g_R^f\gamma^\mu(1+\gamma^5)\right] \tag{1.2}$$

where $g_{L,R}^f$ are the left and right dimensionless coupling constants, γ^μ and $\gamma^\mu\gamma^5$ are Dirac matrices, and g_F is an overall coupling strength. The superscript "f" indicates that the coupling may be different for each type of fermion. The terms in the square brackets can be rearranged to collect all the terms in γ^μ and all the terms in $\gamma^\mu\gamma^5$ giving

$$2g_F\left[g_v^f\gamma^\mu + g_a^f\gamma^\mu\gamma^5\right] \tag{1.3}$$

Force	Couples	Coupling strength
EM	γ to q, ℓ	$g_e = \sqrt{4\pi\alpha}, \alpha \approx 1/129$
Strong	g to q	$g_s = \sqrt{4\pi\alpha_s}, \alpha_s \approx 1/8$
Weak	$W^{\pm}$ to q, ℓ	$g_W = \sqrt{4\pi\alpha_W}, \alpha_W \approx 1/30$
	Z^0 to q, ℓ	$g_Z = \sqrt{4\pi\alpha_Z}, \alpha_Z \approx 1/23$

Table 1.3: *Table of the coupling strengths of bosons to fermions. Values are given at the scale of the mass of the Z^0. The calculation of the coupling strengths g_W and g_Z uses equation 1.4.*

where $g_v^f = \frac{1}{2}(g_R^f + g_L^f)$ and $g_a^f = \frac{1}{2}(g_L^f - g_R^f)$. The terms with γ^μ produce Dirac currents that transform as vectors under spatial inversions (also called parity transformations) while the terms with $\gamma^\mu\gamma^5$ produce axial-vector currents.

The electromagnetic and strong forces conserve parity. They are indifferent to the "handedness" of the fermions, in other words $g_L^f = g_R^f$ in equation 1.2 resulting in a purely vector-like vertex factor. The overall coupling, g_F, represents the electromagnetic coupling constant, g_e, and the strong coupling constant, g_s, listed in table 1.3.

The weak force violates parity. The coupling strength depends on the handedness of the fermion. The charged weak force violates parity maximally because the W boson only couples to left-handed fermions. Therefore, $g_R^f = 0$ and $g_L^f = 1$ in equation 1.2 creating a vector minus axial-vector vertex factor known as V-A. The overall strength is related to the charged weak coupling constant, g_W. For example, the exchange of a W can then be seen as converting a neutrino, which is always left-handed, into the corresponding left-handed charged lepton. The left-handed charged leptons and corresponding neutrinos can therefore be arranged in weak isospin doublets as shown in table 1.4, the third component of the weak isospin, I_3, being given in table 1.4 for each doublet. The three generations of doublets (for example e^-, μ^-, τ^-) are referred to as families. The right-handed charged leptons are included in the theory as weak isospin singlets. The charged weak force interacts identically with all the left-handed fermion doublets. This invariance of the charged weak force under weak isospin is known as the $SU(2)_L$ symmetry.

Left handed fermion doublets	q_f	I_3
$\begin{pmatrix}\nu_e\\ e^-\end{pmatrix}_L \begin{pmatrix}\nu_\mu\\ \mu^-\end{pmatrix}_L \begin{pmatrix}\nu_\tau\\ \tau^-\end{pmatrix}_L$	0 $-e$	$1/2$ $-1/2$
$\begin{pmatrix}u\\ d\end{pmatrix}_L \begin{pmatrix}c\\ s\end{pmatrix}_L \begin{pmatrix}t\\ b\end{pmatrix}_L$	$2/3e$ $-1/3e$	$1/2$ $-1/2$
Right handed fermion singlets	q_f	I_3
$(e^-)_R$ $(\mu^-)_R$ $(\tau^-)_R$	$-e$	0
$(u)_R$ $(c)_R$ $(t)_R$	$2/3e$	0
$(d)_R$ $(s)_R$ $(b)_R$	$-1/3e$	0

Table 1.4: *Table of the fermion charge, q_f, and the weak isospin, I_3.*

The work of Glashow, Weinberg, and Salam [4, 5, 6] showed that θ_W not only relates the masses of the weak bosons, but also unifies the electromagnetic and weak forces into what is referred to as the electroweak force. The coupling strength of the electromagnetic force, g_e, is related to the weak coupling constants, g_W and g_Z, through the Weinberg angle

$$g_W = \frac{g_e}{\sin\theta_W} \qquad g_Z = \frac{g_e}{\sin\theta_W\cos\theta_W}. \tag{1.4}$$

The neutral weak force couples unequally to left-handed and right-handed fermions implying parity violation. The couplings which depend on the Weinberg mixing angle, θ_W are given by

$$g^f_{L,R} = 2I_3^{L,R} - 2q_f\sin^2\theta_W \tag{1.5}$$

where $I_3^{L,R}$ is the third component of the weak isospin for left-handed and right-handed fermions and q_f is the charge for each type of fermion. Another way of presenting the parity violation in weak interactions is in terms of vector and axial-vector components to the couplings. Equation 1.2 can be expressed, in the case of the neutral weak vertex, as

$$\frac{-ig_Z}{2}\gamma^\mu(g^f_v - g^f_a\gamma^5) \tag{1.6}$$

where $g^f_v = \frac{1}{2}(g^f_R + g^f_L)$ and $g^f_a = \frac{1}{2}(g^f_L - g^f_R)$ are the vector and axial-vector coupling constants summarized in table 1.5. They are related to the Weinberg angle through

Fermion	g_R^f	g_L^f	g_v^f	g_a^f
ν_e, ν_μ, ν_τ	0	1	$\frac{1}{2}$	$\frac{1}{2}$
e^-, μ^-, τ^-	$2\sin^2\theta_W = .46$	$-1 + 2\sin^2\theta_W =-.54$	$-\frac{1}{2} + 2\sin^2\theta_W =-.04$	$-\frac{1}{2}$
u, c, t	$-\frac{4}{3}\sin^2\theta_W \approx -.31$	$1 - \frac{4}{3}\sin^2\theta_W \approx .69$	$\frac{1}{2} - \frac{4}{3}\sin^2\theta_W \approx .19$	$\frac{1}{2}$
d, s, b	$\frac{2}{3}\sin^2\theta_W \approx .15$	$-1 + \frac{2}{3}\sin^2\theta_W \approx -.85$	$-\frac{1}{2} + \frac{2}{3}\sin^2\theta_W \approx -.35$	$-\frac{1}{2}$

Table 1.5: *Table of the couplings g_R^f, g_L^f, g_v^f, and g_a^fevaluated at* $\sin^2\theta_W$= *0.23.* $g_R^f \neq g_L^f$ *indicates parity violation for all quarks and leptons.*

equation 1.5

$$\frac{g_v^f}{g_a^f} = 1 - 2\frac{q_f}{I_3^L}\sin^2\theta_W. \tag{1.7}$$

The relative strengths of the charged weak and neutral weak coupling constants, g_W and g_Z, are listed in table 1.3. Note that the neutral weak coupling depends on the charge and the weak isospin of the fermion. The three charged leptons therefore are expected to have the same coupling. This is referred to as lepton universality and will be tested in this thesis.

The Weinberg angle, θ_W, is an important quantity because it relates different quantities to the same parameter of the Standard Model. Measuring $\sin^2\theta_W$ several different ways tests the consistency of the theory. In particular, any physics process which measures the relative coupling strength of vector and axial-vector components of the neutral weak force measures the Weinberg angle.

For example, neutrino-electron scattering, $\overline{\nu}_\mu - e^- \rightarrow \overline{\nu}_\mu - e^-$ as depicted in figure 1.1, measures these relative couplings. The Weinberg angle has been extracted to a precision of four percent [3] from this process. The Weinberg angle can also be determined by measuring the masses of the carriers of the weak force, the $W^\pm$ and the Z^0, with the use of equation 1.1. From this method, the value of the Weinberg angle is known to one percent [3].

The measurements of the ratios of the vector and axial-vector couplings, g_v^τ/g_a^τ and

g_v^e/g_a^e, as given in equation 1.7 from the process $e^+e^- \rightarrow \tau^+\tau^-$ with the OPAL detector at the LEP accelerator are presented in this thesis. The expectation that the Z^0 couples equally to all leptons (known as lepton universality) is tested by comparing the two ratios g_v^τ/g_a^τ and g_v^e/g_a^e. A 0.8 percent measurement of the Weinberg angle is made in this thesis by using equation 1.7 and the expectation of lepton universality. Other measurements of the Weinberg angle through the process $e^+e^- \rightarrow \tau^+\tau^-$ at OPAL are combined to extract this value with a 0.6 percent precision. The results of this thesis are a significant contribution to the measurement of the Weinberg angle.

1.2 Procedure for the Measurement of Parity Violating Effects

The LEP collider in Geneva, Switzerland produces the carrier of the neutral weak currents by colliding electrons and positrons through the process $e^+e^- \rightarrow Z^o \rightarrow f\overline{f}$ where the fermions $f\overline{f}$ can be lepton-antilepton pairs: e^+e^-, $\mu^+\mu^-$, $\tau^+\tau^-$, $\nu_e\overline{\nu}_e$, $\nu_\mu\overline{\nu}_\mu$, and $\nu_\tau\overline{\nu}_\tau$ or quark-antiquark pairs with total mass less than the mass of the Z^0: $u\overline{u}$, $d\overline{d}$, $s\overline{s}$, $c\overline{c}$, and $b\overline{b}$. The final state particles produced in these collisions are observed and recorded by the OPAL detector at LEP. The measurement of the ratio of the vector and axial-vector couplings using the process $e^+e^- \rightarrow \tau^+\tau^-$is presented in this thesis work. The unequal coupling of the Z^0 to left-handed and right-handed $e^\pm$ and $\tau^\pm$ produces an unequal amount of left-handed and right-handed $\tau^\pm$. This asymmetry can be quantified by the tau polarization, P_τ: the difference in the number of τ's with right and left spin orientation over the total number of τ's in the sample. The tau polarization is dependent on the angular separation, θ, between the incoming e^- and the outgoing τ^-. This angular dependence is quantified by the forward-backward polarization asymmetry, $\mathrm{A}_{\mathrm{pol}}^{\mathrm{FB}}$, which is the difference in the polarization of a forward scattered τ^-, $\cos\theta > 0$, and a backward scattered τ^-, $\cos\theta < 0$.

In this thesis, the $\tau^\pm \rightarrow \rho^\pm\nu_\tau$ channel is used to determine these asymmetries because of its large branching ratio and good sensitivity to an extraction of the tau polarization. The tau polarization information is extracted from the kinematics of the tau decay products.

Unlike the other leptons, the tau has a short lifetime and therefore it decays within the OPAL detector. Consequently, it is the only lepton whose polarization can be measured at LEP. Quark-antiquark pairs are unsuitable for a polarization measurement because the transfer of the spin from the quarks to the decay products is perturbed by the strong interaction.

The formalism necessary to extract the polarization asymmetries of the $e^+e^- \rightarrow \tau^+\tau^-$ process is explained in chapter 2. The radiative corrections which affect the $e^+e^- \rightarrow \tau^+\tau^-$ process are also discussed. The polarization asymmetries are extracted from the $\tau^\pm \rightarrow \rho^\pm\nu_\tau$ channel by measuring polarization sensitive observables which depend on the angular distribution of the $\tau^\pm$ decay products. These are also introduced in chapter 2.

A description of the OPAL detector at the LEP accelerator is given in chapter 3. Special emphasis is given to the central tracking detector system and the electromagnetic calorimeter which are essential to the identification of $\tau^\pm \rightarrow \rho^\pm\nu_\tau$ events.

The $\tau^\pm$ pairs are identified with the OPAL detector by isolating events which have the expected topology of $e^+e^- \rightarrow \tau^+\tau^-$ decays. The selection criteria used to identify $\tau^\pm$ pairs are given in chapter 4. The electromagnetic calorimeter is used to identify $\tau^\pm$ particles which have decayed to ρ's. A special emphasis is given to the identification of ρ's through the reconstruction of π°'s, one of the decay products of the ρ. The polarization sensitive variables developed in chapter 2 are reconstructed with the identified $\tau^\pm \rightarrow \rho^\pm\nu_\tau$ events.

The extraction of the asymmetries, $\langle \mathrm{P}_\tau \rangle$ and $\mathrm{A}^{\mathrm{FB}}_{\mathrm{pol}}$, is discussed in chapter 5. Systematic errors of these measurements are assessed by estimating the uncertainties in the response of the OPAL detector and the limitations on the theoretical knowledge of the process.

The ratios of the vector and axial-vector couplings, g_v^τ/g_a^τ and g_v^e/g_a^e, are extracted from the polarization asymmetries in chapter 6. A test of lepton universality is made and the results are then used to measure the Weinberg angle. The results of this thesis are compared to the similar results of the other LEP experiments of the tau polarization and polarization asymmetry. The results reported in this thesis are currently the most precise values.

The results of this thesis are summarized in chapter 7.

Chapter 2

Formalism of the Process $e^+e^- \rightarrow \tau^+\tau^-$

This chapter develops the formalism that describes the production of tau pairs in the reaction $e^+e^- \rightarrow \gamma, Z^o \rightarrow \tau^+\tau^-$ at the LEP collider. The theoretical description of the extraction of the average tau polarization, $\langle \mathrm{P}_\tau \rangle$, and its forward-backward asymmetry, $\mathrm{A}_{\mathrm{pol}}^{\mathrm{FB}}$, from the $\tau^\pm \rightarrow \rho^\pm \nu_\tau$ decay channel is explained.

A Born-level calculation of the differential cross section and total cross section of the process $e^+e^- \rightarrow \tau^+\tau^-$ is related to measured asymmetries and the amount of parity violation in the neutral current weak interaction. The sensitivity of the measured asymmetries to $\sin^2\theta_W$ is given. Radiative corrections to the Born-level cross section are discussed. Finally, an analysis of the spin properties of the decay $\tau^\pm \rightarrow \rho^\pm \nu_\tau$ is made and observables sensitive to the tau polarization are introduced.

2.1 The Born Approximation for the Process $e^+e^- \rightarrow \tau^+\tau^-$

The Feynman diagrams of the first-order (Born approximation) processes contributing to the reaction $e^+e^- \rightarrow \tau^+\tau^-$ are shown in figure 2.1. A $\tau^+\tau^-$ pair can be produced by the annihilation of an e^+e^- pair to a photon, γ, or to the neutral weak boson, Z^0. Both processes can be described in terms of an amplitude which is constructed by the application of the appropriate Feynman rules. The total amplitude for $e^+e^- \rightarrow \gamma, Z^o \rightarrow \tau^+\tau^-$ process is $\mathcal{M} = \mathcal{M}_\gamma + \mathcal{M}_Z$. The amplitude for the photon exchange contribution is given by [7]

$$\mathcal{M}_\gamma = \left(\bar{u}(\tau^-)[ig_\tau\gamma^\nu]v(\tau^+)\right)\left[-\frac{ig_{\mu\nu}}{q^2}\right]\left(\bar{v}(e^+)[ig_e\gamma_\mu]u(e^-)\right). \tag{2.1}$$

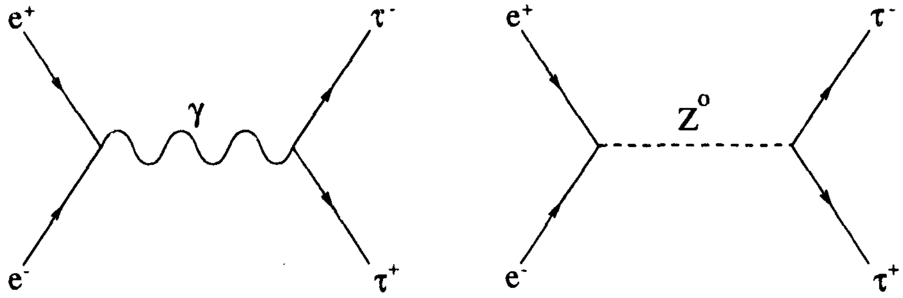

Figure 2.1: *The Born level Feynman diagrams of the process $e^+e^- \rightarrow \tau^+\tau^-$ include photon exchange and Z^0 exchange.*

The first (last) square-bracketed term is the coupling of the $\tau(e)$ to the γ and the middle square-bracketed term is the photon propagator. The u and v terms are the particle and antiparticle wavefunctions of the $e^\pm$ and $\tau^\pm$. Similarly, the amplitude for the $e^+e^- \rightarrow Z^o \rightarrow \tau^+\tau^-$ process is [7]

$$\mathcal{M}_Z = \left(\overline{u}(\tau^-)[-\frac{ig_Z}{2}\gamma^\nu(g_v^\tau - g_a^\tau\gamma^5)]v(\tau^+)\right)\left[\frac{-i(g_{\mu\nu} - q_\mu q_\nu/M_Z^2)}{q^2 - M_Z^2}\right] \times$$

$$\left(\overline{v}(e^+)[-\frac{ig_Z}{2}\gamma_\mu(g_v^e - g_a^e\gamma^5)]u(e^-)\right) \tag{2.2}$$

where the first (last) square-bracketed term is the coupling of the $\tau(e)$ to the Z^0 and the middle square-bracketed term is the Z^0 propagator. The differential cross section for the production of a τ pair is proportional to $|\mathcal{M}|^2 = |\mathcal{M}_\gamma + \mathcal{M}_Z|^2$. There will be terms that depend on $|\mathcal{M}_\gamma|^2$, $|\mathcal{M}_Z|^2$, and interference between the two terms. Averaging over the initial electron spins, as electrons and positrons are unpolarized in this experiment, the differential cross section for $e^+e^- \rightarrow \tau^+\tau^-$ assuming a massless tau[1], is [8]

$$\frac{d\sigma}{d\cos\theta}(\theta, s, h_{\tau^-}) = \frac{\pi\alpha^2}{4s}\left[(F_0(s) - h_{\tau^-}F_2(s))(1 + \cos^2\theta) + 2(F_1(s) - h_{\tau^-}F_3(s))\cos\theta\right] \tag{2.3}$$

where the τ helicity states are $h_{\tau^-} = \pm 1$. There are four nonzero helicity combinations for the exchange of a vector particle in the limit of massless electrons and taus. They are shown in figure 2.2. The scattering angle, θ, also shown in figure 2.2, is defined as the

---

[1] The massless approximation is appropriate for tau leptons produced at LEP where the velocity of a tau is $\beta = v/c = .9992$.

angle between the incoming e^- flight direction and the outgoing τ^-. The four functions in equation 2.3

$$F_0(s) = 1 + 2\Re[\chi(s)]g_v^e g_v^\tau + |\chi(s)|^2({g_v^e}^2 + {g_a^e}^2)({g_v^\tau}^2 + {g_a^\tau}^2)$$

$$F_1(s) = 2\Re[\chi(s)]g_a^e g_a^\tau + |\chi(s)|^2(2g_v^e g_a^e)(2g_v^\tau g_a^\tau)$$

$$F_2(s) = 2\Re[\chi(s)]g_v^e g_a^\tau + |\chi(s)|^2({g_v^e}^2 + {g_a^e}^2)(2g_v^\tau g_a^\tau)$$

$$F_3(s) = 2\Re[\chi(s)]g_a^e g_v^\tau + |\chi(s)|^2(2g_v^e g_a^e)({g_v^\tau}^2 + {g_a^\tau}^2).$$

are dependent on the center-of-mass energy, $\sqrt{s}$, through the Breit-Wigner term

$$\chi(s) = \frac{\sqrt{2}G_F M_Z^2}{4\pi\alpha}\left[\frac{s}{s - M_Z^2 + is\Gamma_Z/M_Z}\right] \tag{2.4}$$

which is introduced to approximate the finite width of the Z^0 boson. The constant, G_F, is the Fermi coupling constant $G_F = \frac{\sqrt{2}}{8}\frac{g_W^2}{M_W^2}$, Γ_Z is the width of the Z^0, and M_Z is its mass. Because the e^+e^- annihilation occurs in a spin 1 state, the τ^+ (with spin 1/2) has the opposite helicity to the τ^- in the same event so the helicity of the τ^+ is the negative of the helicity of the τ^-. The photon exchange contribution appears as the first term in the function $F_0(s)$. The interference terms include a factor $\Re[\chi(s)]$ (where $\Re$ is the real part) and the Z^0 exchange terms have a factor of $|\chi(s)|^2$.

The total cross section of the process $e^+e^- \to \tau^+\tau^-$ is found by summing equation 2.3 over the possible final helicity states and integrating over $\cos\theta$ resulting in

$$\sigma(s) = \frac{4\pi}{3}\frac{\alpha^2}{s}F_0(s). \tag{2.5}$$

The total cross section has contributions from the photon exchange, the Z^0 exchange, and the $\gamma - Z^0$ interference terms

$$\sigma = \sigma_\gamma + \sigma_Z + \sigma_{\gamma Z}$$

as shown in figure 2.3. At the $\sqrt{s} = M_Z$, the Z^0 boson exchange completely dominates the process by a factor

$$\frac{\sigma_Z}{\sigma_\gamma} \approx 200.$$

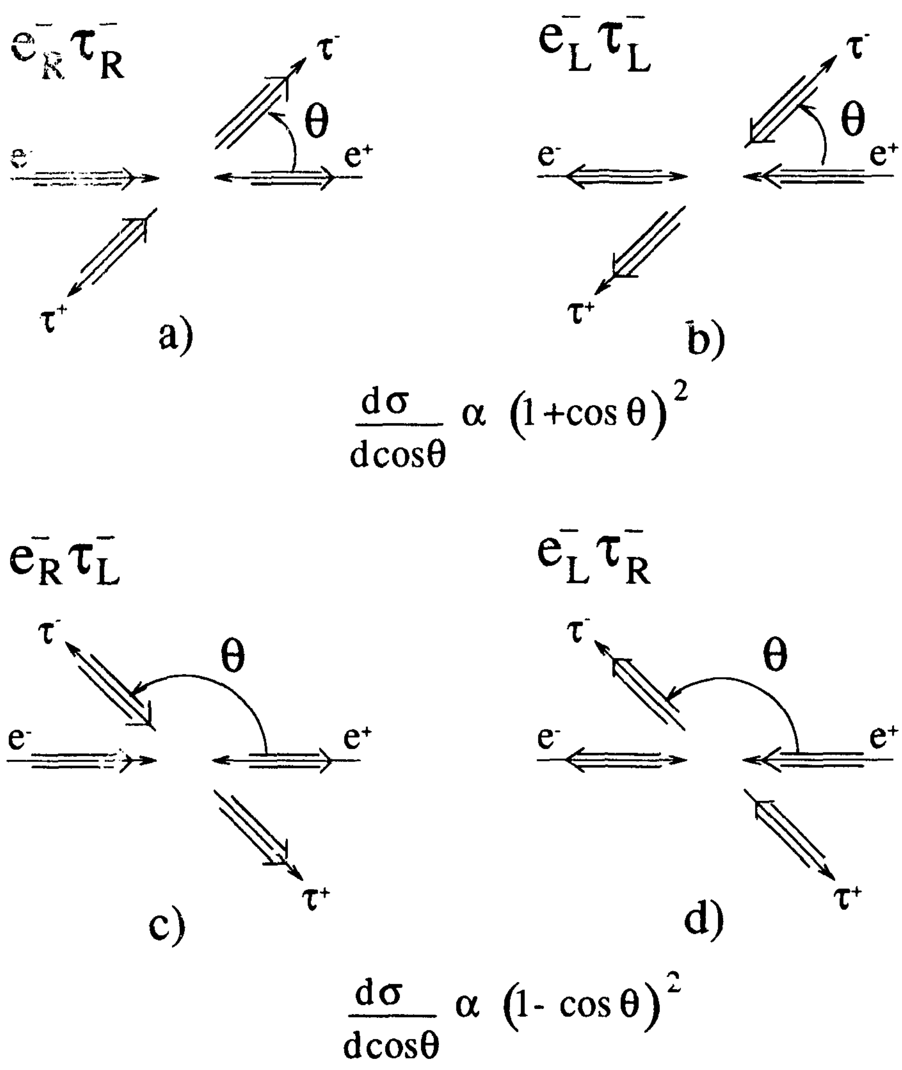

$$\frac{d\sigma}{d\cos\theta} \propto (1+\cos\theta)^2$$

$$\frac{d\sigma}{d\cos\theta} \propto (1-\cos\theta)^2$$

Figure 2.2: *The possible helicity states of the tau. The double arrows indicate the helicity of the $e^\pm$ and the $\tau^\pm$. Figures a) and d) show right-handed (positive helicity) τ^- while figures b) and c) show left-handed (negative helicity) τ^-. The scattering angle, θ, is defined as the angle between the incoming e^- flight direction and the outgoing τ^-. Figures a) and b) show the predominance of the production of forward scattered τ^- for the helicity configurations shown while figures c) and d) show the predominance of the production of backward scattered τ^- for the corresponding helicity configurations.*

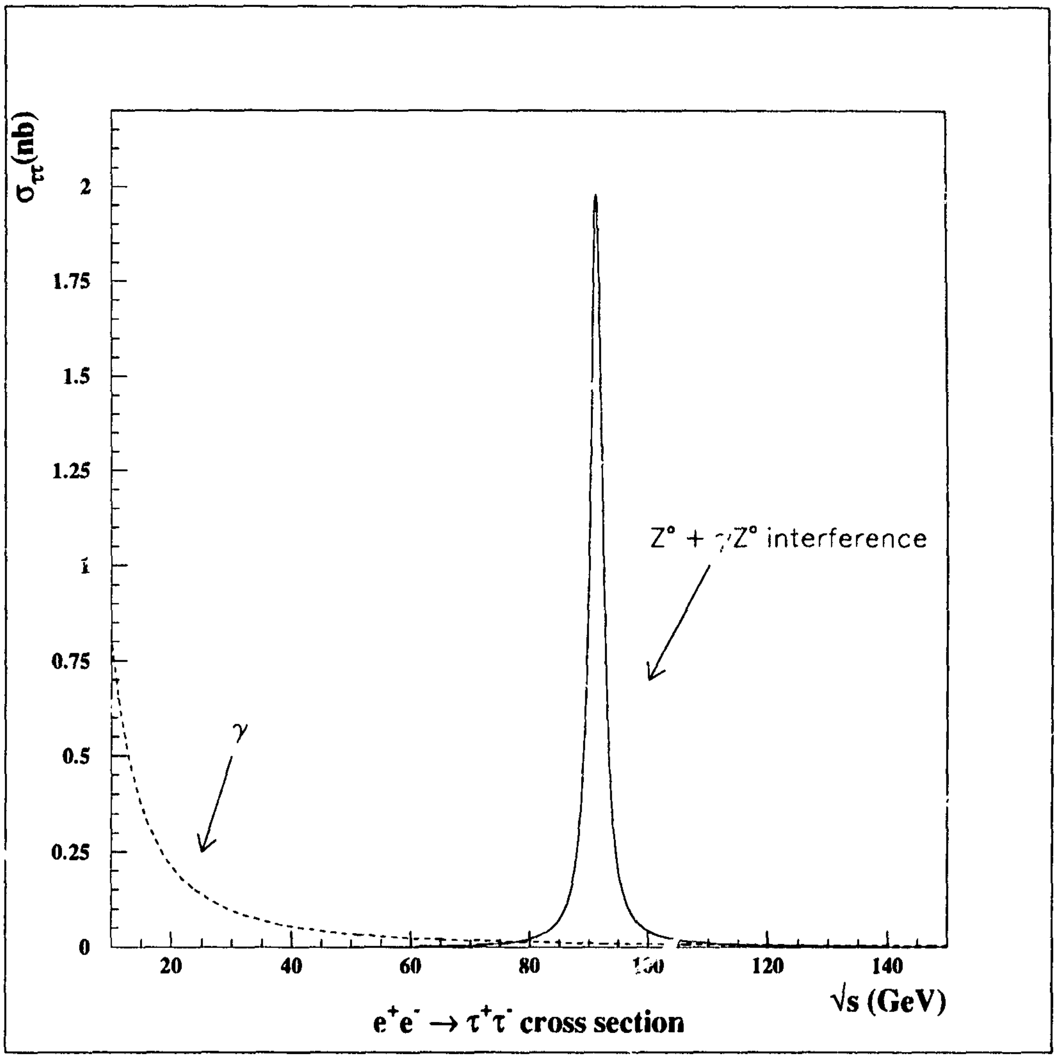

Figure 2.3: *The total cross section of the process* $e^+e^- \to \tau^+\tau^-$. *Near the* Z^0 *pole, the* $\gamma - Z^o$ *interference is a factor of* 10^{-3} *smaller that the* Z^0 *exchange term and is identically zero at the* Z^0 *peak.*

The differential cross section, equation 2.3, can be written as

$$\frac{d\sigma}{d\cos\theta}(\theta) = A(1+\cos\theta^2) + B\cos\theta. \tag{2.6}$$

The first term is symmetric in $\cos\theta$ while the second term is asymmetric. The asymmetric term does not have a contribution from the purely electromagnetic interaction and is a manifestation of the parity violation of the weak interaction. The forward-backward asymmetry is defined as the difference in the cross section for forward scattered final state taus ($\cos\theta > 0$) and backward scattered final state taus ($\cos\theta < 0$) summed over both helicities normalized by the total $e^+e^- \to \tau^+\tau^-$ cross section.

$$\mathrm{A}^{\mathrm{FB}} = \frac{\int_0^1 \frac{d\sigma}{d\cos\theta} d\cos\theta - \int_{-1}^0 \frac{d\sigma}{d\cos\theta} d\cos\theta}{\int_0^1 \frac{d\sigma}{d\cos\theta} d\cos\theta + \int_{-1}^0 \frac{d\sigma}{d\cos\theta} d\cos\theta} = \frac{3}{4}\frac{F_1(s)}{F_0(s)}.$$

At the Z^0 pole, the $\Re[\chi(s)] = 0$. Therefore, only the Z^0 exchange term contributes and the forward-backward asymmetry is given by

$$\mathrm{A}^{\mathrm{FB}} \approx \frac{3g_v^e g_a^e g_v^\tau g_a^\tau}{(g_v^{e2} + g_a^{e2})(g_v^{\tau 2} + g_a^{\tau 2})} = \frac{3}{4}\mathrm{A}_e\mathrm{A}_\tau \tag{2.7}$$

where

$$\mathrm{A}_\ell \equiv \frac{2g_v^\ell g_a^\ell}{(g_v^{\ell 2} + g_a^{\ell 2})} \qquad \text{for } \ell = e, \tau \tag{2.8}$$

is equivalent to the polarization analyzing power of leptonic neutral current decays. Figure 2.4 shows the forward-backward asymmetry as a function of the center-of-mass energy in the Standard Model for a value of $\sin^2\theta_W = 0.23$. Near the Z^0 pole, the approximation $\mathrm{A}_\ell \approx 2\frac{g_v^\ell}{g_a^\ell}$ is valid so it follows that A^{FB} measures the ratio of the vector coupling to the axial-vector coupling, but not the relative signs of the couplings.

The parity violation of the neutral current interaction produces a forward-backward polarization asymmetry because the unequal coupling of the left-handed and right-handed initial state electrons to the Z^0 produces a polarized Z^0. When the Z^0 decays to two fermions, the unequal couplings of the two final state fermions to the Z^0 also produces a polarized final state. In the case of the Z^0 decaying to taus, it is possible to measure this polarization by analyzing the kinematics of the decay products of the tau. If the contribution from photon exchange is neglected, the relations $g_v^\ell = \frac{1}{2}(g_R^\ell + g_L^\ell)$ and

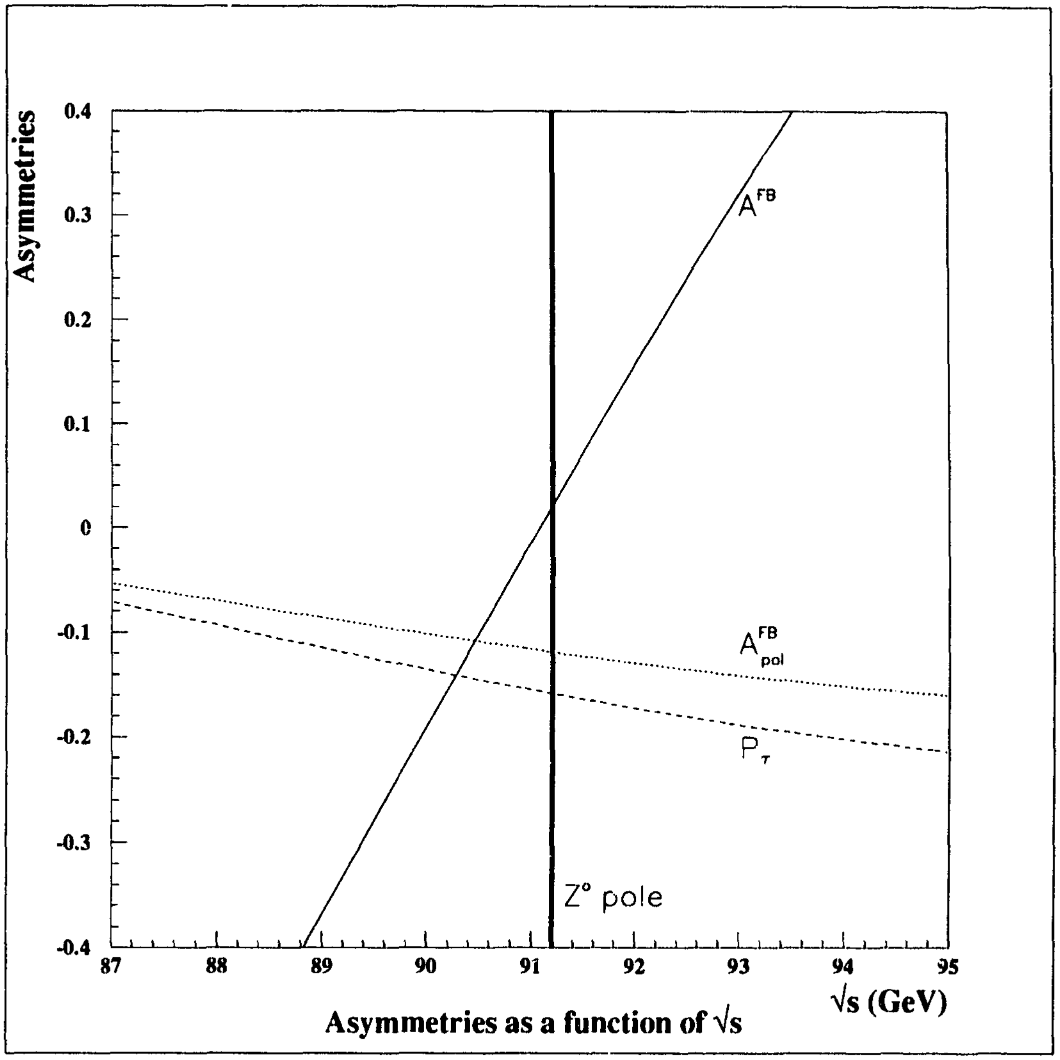

Figure 2.4: *The forward-backward asymmetry,* A^{FB}*, the average tau polarization,* $\langle P_\tau \rangle$*, and the forward-backward polarization asymmetry,* A^{FB}_{pol}*, as a function of the center-of-mass energy. The forward-backward asymmetry is almost zero at* $\sqrt{s} = M_Z$*.* $A^{FB}(\sqrt{s} = M_Z) \approx 0.02$ *for a value of* $\sin^2\theta_W = 0.23$.

$g_a^\ell = \frac{1}{2}(g_L^\ell - g_R^\ell)$ can be used to write the differential cross section explicitly for each helicity combination in terms of left-handed and right-handed couplings. At the Z^0 pole [2]

$$\frac{d\sigma}{d\cos\theta}(e_R^- e_L^+ \rightarrow \tau_R^- \tau_L^+) = \frac{\pi\alpha^2}{2s}(1+\cos\theta)^2 |\chi(s)|^2 |g_R^e g_R^\tau|^2 \tag{2.9}$$

$$\frac{d\sigma}{d\cos\theta}(e_L^- e_R^+ \rightarrow \tau_L^- \tau_R^+) = \frac{\pi\alpha^2}{2s}(1+\cos\theta)^2 |\chi(s)|^2 |g_L^e g_L^\tau|^2 \tag{2.10}$$

$$\frac{d\sigma}{d\cos\theta}(e_R^- e_L^+ \rightarrow \tau_L^- \tau_R^+) = \frac{\pi\alpha^2}{2s}(1-\cos\theta)^2 |\chi(s)|^2 |g_R^e g_L^\tau|^2 \tag{2.11}$$

$$\frac{d\sigma}{d\cos\theta}(e_L^- e_R^+ \rightarrow \tau_R^- \tau_L^+) = \frac{\pi\alpha^2}{2s}(1-\cos\theta)^2 |\chi(s)|^2 |g_L^e g_R^\tau|^2 \tag{2.12}$$

corresponding to the four diagrams in figure 2.2. The polarization of the Z^0 induces an angular dependence in the polarization of the τ which can be expressed as

$$P_\tau(\cos\theta) = \frac{\left.\frac{d\sigma}{d\cos\theta}\right|_R - \left.\frac{d\sigma}{d\cos\theta}\right|_L}{\left.\frac{d\sigma}{d\cos\theta}\right|_R + \left.\frac{d\sigma}{d\cos\theta}\right|_L} \tag{2.13}$$

where $\left.\frac{d\sigma}{d\cos\theta}\right|_{L,R}$ is the differential cross section for producing left-handed (equations 2.10 and 2.11) and right-handed (equations 2.9 and 2.12) τ^- particles. The two taus in the same event have opposite polarizations so in general $P_{\tau^-} = -P_{\tau^+} = P_\tau$. This polarization asymmetry as predicted by the Standard Model for a value of $\sin^2\theta_W = 0.23$ is plotted as a function of $\cos\theta$ in figure 2.5. The figure illustrates two interesting characteristics. At $\cos\theta = -1$, $P_\tau(-1) \propto g_L^{e\,2} g_R^{\tau\,2} - g_R^{e\,2} g_L^{\tau\,2}$. A non-zero value of $P_\tau(-1)$ implies that the Z^0 couples differently to electrons and taus violating lepton universality, i.e. the expectation that the Z^0 couples equally to all leptons. At $\cos\theta = 1$, $P_\tau(1) \propto g_R^{e\,2} g_R^{\tau\,2} - g_L^{e\,2} g_L^{\tau\,2} \neq 0$ which is a clear indication of parity violation. Neglecting radiative corrections and the contribution from photon exchange, at $\sqrt{s} = M_Z$:

$$P_\tau(\cos\theta) \approx -\left[\frac{\mathrm{A}_\tau(1+\cos^2\theta) + 2\mathrm{A}_e\cos\theta}{1+\cos^2\theta + \frac{8}{3}\mathrm{A}^{\mathrm{FB}}\cos\theta}\right]. \tag{2.14}$$

The average tau polarization can be constructed from the differential cross sections for each helicity integrated over the total solid angle

$$\langle \mathrm{P}_\tau \rangle = \frac{\sigma_R - \sigma_L}{\sigma_R + \sigma_L} \tag{2.15}$$

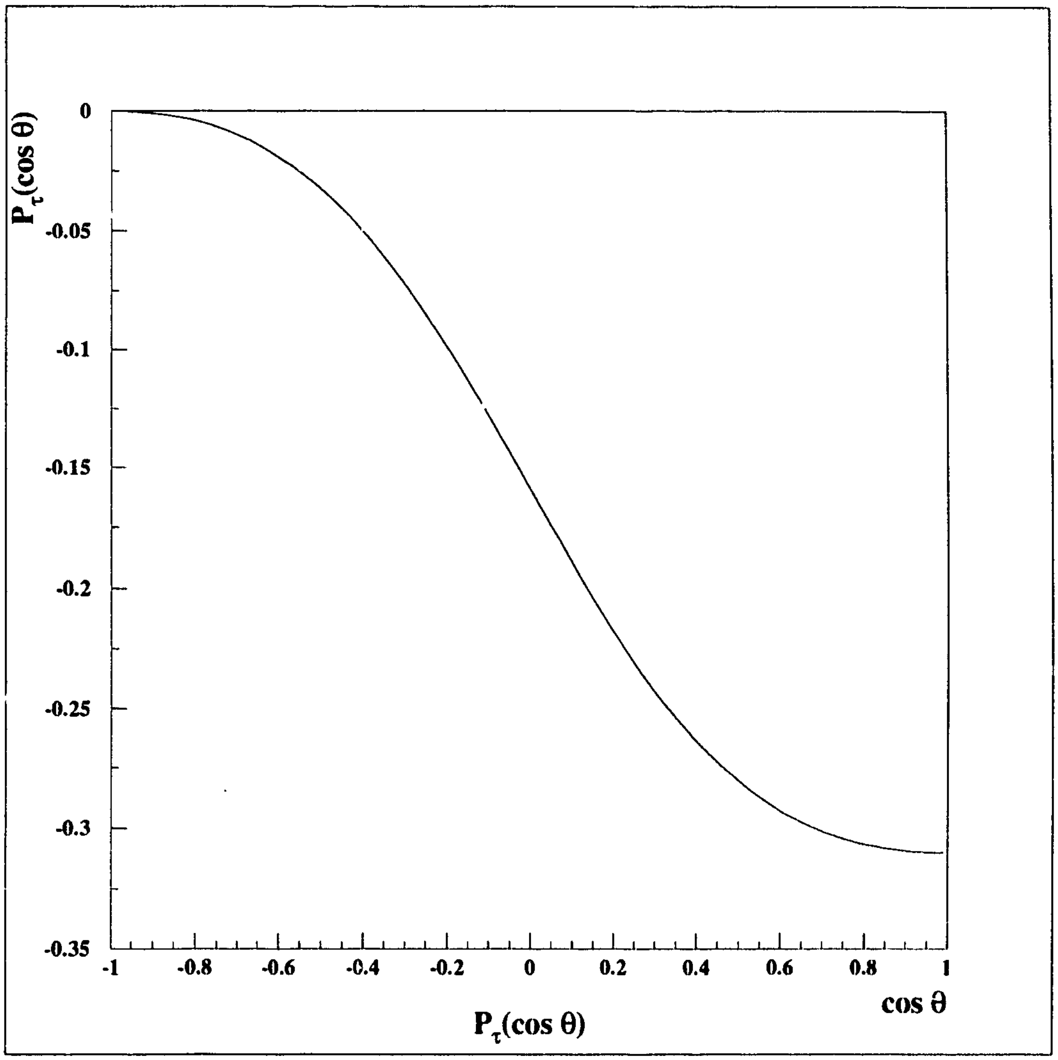

Figure 2.5: *The* τ *polarization as a function of* $\cos\theta$ *for a value of* $\sin^2\theta_W = 0.23$. *Lepton universality requires the function to be zero at* $\cos\theta = -1$. *The general nonzero value of* $P_\tau(\cos\theta)$ *indicates parity violation in the neutral weak interaction.*

where $\sigma_{L,R}$ is the cross section to produce left-handed and right-handed τ^- particles. Near the Z^0 pole

$$\langle \mathrm{P}_\tau \rangle \approx \frac{-2g_v^\tau g_a^\tau}{g_v^{\tau 2} + g_a^{\tau 2}} = -\mathrm{A}_\tau. \tag{2.16}$$

The dependence of $\langle \mathrm{P}_\tau \rangle$ on the center-of-mass energy is shown in figure 2.4. $\langle \mathrm{P}_\tau \rangle$ depends only on the tau coupling strength to the Z^0 as opposed to A^{FB} which also depends on the electron coupling. Moreover, the relative sign of A_τ and A_e is accessible in the measurement of $\langle \mathrm{P}_\tau \rangle$.

Another asymmetry combining A^{FB} and $\langle \mathrm{P}_\tau \rangle$ can be constructed. It is the forward-backward polarization asymmetry defined as the forward-backward asymmetry of the polarization

$$\mathrm{A}^{\mathrm{FB}}_{\mathrm{pol}} = \frac{\left[\int_0^1 \frac{d\sigma}{d\cos\theta}\Big|_R - \int_0^1 \frac{d\sigma}{d\cos\theta}\Big|_L\right] - \left[\int_{-1}^0 \frac{d\sigma}{d\cos\theta}\Big|_R - \int_{-1}^0 \frac{d\sigma}{d\cos\theta}\Big|_L\right]}{\int_0^1 \frac{d\sigma}{d\cos\theta}\Big|_R + \int_0^1 \frac{d\sigma}{d\cos\theta}\Big|_L + \int_{-1}^0 \frac{d\sigma}{d\cos\theta}\Big|_R + \int_{-1}^0 \frac{d\sigma}{d\cos\theta}\Big|_L} \tag{2.17}$$

where $\frac{d\sigma}{d\cos\theta}\Big|_{L,R}$ is the differential cross section for producing left-handed (equations 2.10 and 2.11) and right-handed (equations 2.9 and 2.12) τ^- particles. At $\sqrt{s} = M_Z$

$$\mathrm{A}^{\mathrm{FB}}_{\mathrm{pol}} \approx -\frac{3}{4}\frac{2g_v^e g_a^e}{(g_v^{e2} + g_a^{e2})} = -\frac{3}{4}\mathrm{A}_e. \tag{2.18}$$

$\mathrm{A}^{\mathrm{FB}}_{\mathrm{pol}}$ as a function of the center-of-mass energy is shown in figure 2.4. It only depends on the electron coupling strength.

To summarize, three asymmetries can be constructed from the production of tau pairs through the process $e^+e^- \to \tau^+\tau^-$. Near the Z^0 pole, these asymmetries are

$$\mathrm{A}^{\mathrm{FB}} \approx \frac{3}{4}\mathrm{A}_e\mathrm{A}_\tau \tag{2.19}$$

$$\langle \mathrm{P}_\tau \rangle \approx -\mathrm{A}_\tau \tag{2.20}$$

$$\mathrm{A}^{\mathrm{FB}}_{\mathrm{pol}} \approx -\frac{3}{4}\mathrm{A}_e. \tag{2.21}$$

A measurement of these asymmetries gives the ratio of vector to axial-vector coupling through equation 2.8. Of these measurements, only $\langle \mathrm{P}_\tau \rangle$ and $\mathrm{A}^{\mathrm{FB}}_{\mathrm{pol}}$ provide a relative sign between the couplings. A measurement of $\langle \mathrm{P}_\tau \rangle$ and $\mathrm{A}^{\mathrm{FB}}_{\mathrm{pol}}$ would also expose a violation of lepton universality.

The vector and axial-vector couplings are related to and the Weinberg angle

$$\frac{g_v^\ell}{g_a^\ell} = 1 - 4\sin^2\theta_W \tag{2.22}$$

which can be used with equation 2.8 to relate the asymmetries to $\sin^2\theta_W$ resulting in

$$A_\ell = \frac{(1 - 4\sin^2\theta_W)}{(1 - 4\sin^2\theta_W + 8\sin^4\theta_W)}. \tag{2.23}$$

If $x_w = \sin^2\theta_W$, then the sensitivities of each asymmetry to a measurement of $\sin^2\theta_W$ can be written as

$$\delta A^{FB} \approx \frac{\partial}{\partial x_w}\left(\frac{3}{4}A_\ell^2\right)\delta x_w \approx -1.9\delta x_w \tag{2.24}$$

$$\delta\langle P_\tau\rangle \approx \frac{\partial}{\partial x_w}(-A_\ell)\,\delta x_w \approx -7.8\delta x_w \tag{2.25}$$

$$\delta A_{pol}^{FB} \approx \frac{\partial}{\partial x_w}\left(-\frac{3}{4}A_\ell\right)\delta x_w \approx -5.5\delta x_w \tag{2.26}$$

where lepton universality has been assumed $A_e = A_\tau = A_\ell$. The sensitivity of A_ℓ to $\sin^2\theta_W$ in these equations is calculated for $\sin^2\theta_W = 0.23$. Figure 2.6 shows these asymmetries for a range of values for $\sin^2\theta_W$. The steep slopes at $\sin^2\theta_W = 0.23$ show that $\langle P_\tau\rangle$ and A_{pol}^{FB} are the most sensitive asymmetries to measurements of $\sin^2\theta_W$.

2.2 Radiative Corrections to the Process $e^+e^- \rightarrow \tau^+\tau^-$: The Improved Born Approximation

The Born approximation of the cross section of the process $e^+e^- \rightarrow \tau^+\tau^-$ as given in equation 2.5 is not adequate to describe the measured data. The charged particles in the initial and final states can radiate photons. These photonic corrections will be discussed in the next section followed by a discussion of the non-photonic corrections. The higher-order processes also affect the strength of the photon and Z^0 exchange contributions and there are important vertex corrections where heavy bosons are exchanged between the final and initial state charged particles. The measured cross section of the process $e^+e^- \rightarrow \tau^+\tau^-$ is the sum of the Born level diagram plus all of the radiative corrections.

The electroweak theory is a renormalizable gauge theory which implies that the cross section can be calculated via a perturbation expansion. The QED radiative corrections

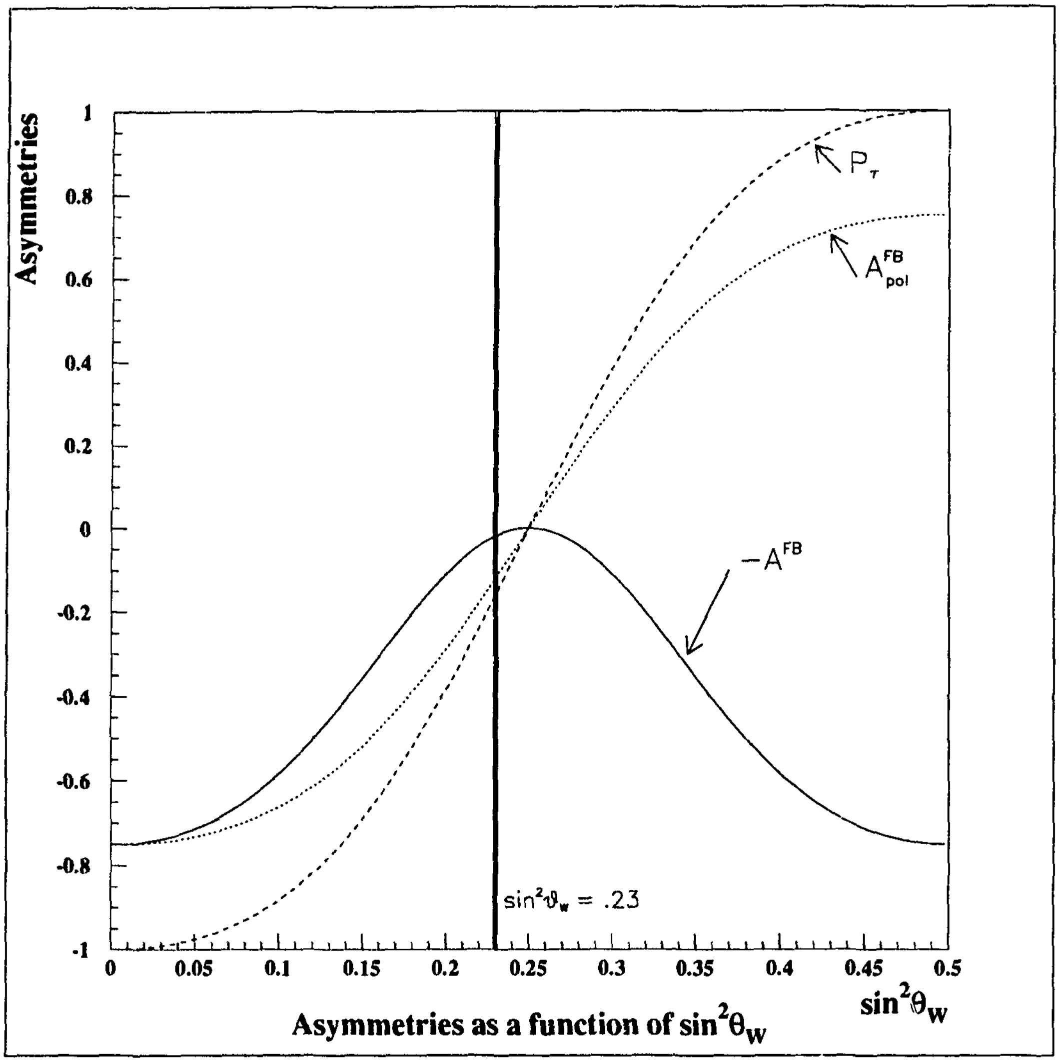

Figure 2.6: *The sensitivity of the forward-backward asymmetry,* A^{FB}, *the* τ *polarization,* $\langle P_\tau \rangle$, *and the forward-backward polarization asymmetry,*A^{FB}_{pol}, *to* $\sin^2\theta_W$*as calculated using equation 2.8 with equations 2.7, 2.16, and 2.18 respectively where no radiative corrections have been included.*

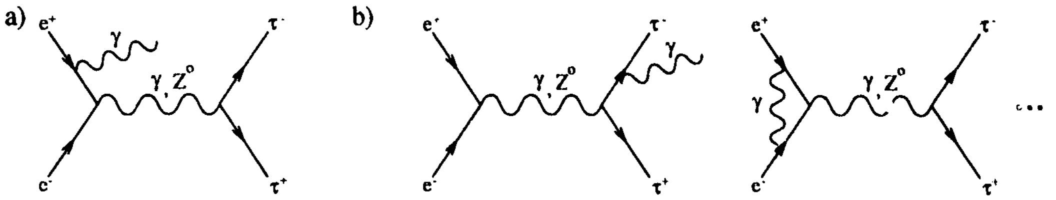

Figure 2.7: *The photonic radiative diagrams associated with the process $e^+e^- \to \gamma, Z^0 \to \tau^+\tau^-$. a) Initial state bremsstrahlung has a 30% effect on the cross section. b) Other less important radiative diagrams.*

which include the initial and final state radiation as well as photon exchange between the fermions depend only on particles whose masses are less than the energy scale of the process. These corrections are exactly calculable to all orders. The weak radiative corrections which include the Z^0 loop corrections as well as the vertex corrections depend on particles of all masses; even above the energy scale of the process. This allows the indirect observation of physics which would not normally be accessible because the energy scale of the physics is above the available energy of colliders.

The photon and Z^0 exchange corrections make the QED and weak coupling constants energy dependent. However, unlike QED, the electroweak theory is non-abelian (i.e. the weak gauge bosons can couple to themselves) and therefore the weak coupling strength decreases with energy while the QED coupling rises with energy.

The diagrams associated with the radiative processes for $e^+e^- \to \tau^+\tau^-$ can be classified into two types: purely photonic corrections and non-photonic corrections. These are described in the next two sections and are incorporated in an Improved Born Approximation of the cross section.

2.2.1 Photonic Corrections

Examples of the photonic diagrams associated with the process $e^+e^- \to \tau^+\tau^-$ are shown in figure 2.7 [9]. The dominant correction at the Z^0 pole is initial state Bremsstrahlung (figure 2.7a) which has a 30% effect [9] on the cross section as shown in figure 2.8. Initial state radiation changes the effective center-of-mass energy of the system. These QED

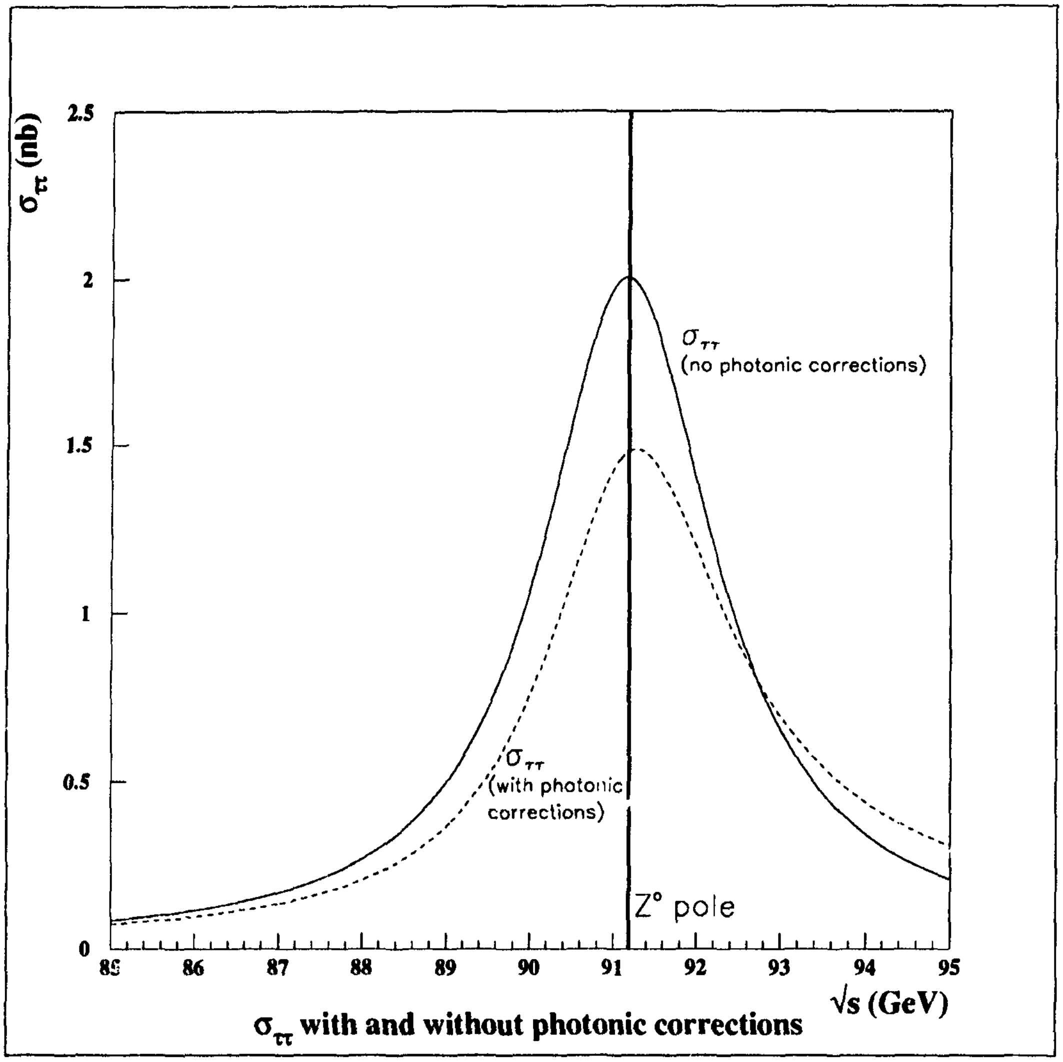

Figure 2.8: *The effect of initial state bremsstrahlung on the cross section of the $e^+e^- \to \tau^+\tau^-$ process is shown with the use of the ZFITTER package [10].*

radiative effects are taken into account by convoluting the $e^+e^- \rightarrow \tau^+\tau^-$ cross section with a radiator function. This function is completely calculated to $\mathcal{O}(\alpha)$ with leading $\mathcal{O}(\alpha^2)$ terms and soft exponentiation. The theoretical uncertainty on this function is of order 0.1% [9].

2.2.2 Non-photonic Corrections

The non-photonic radiative effects are taken into account by using the Improved Born Approximation approach [9]. In this approximation, $\sin^2\theta_W = 1 - M_W^2/M_Z^2$ is taken to be correct to all orders while the coupling constants become energy dependent couplings.

The photon vacuum polarization diagram where a fermion-antifermion pair is created and destroyed is shown in figure 2.9a [9]. The vacuum polarization of the photon makes the QED coupling energy dependent

$$\alpha \rightarrow \alpha(s) = \frac{\alpha}{1 - \Delta\alpha(s)} \tag{2.27}$$

where at the Z^0 pole $\alpha(M_Z^2) = 1/128.82$ [3]. The dominant uncertainty in this correction (of the order of 0.0009 on $\Delta\alpha(s)$ [11]) comes from the contribution of light quarks in the vacuum polarization loop.

The vacuum polarization of the Z^0 is shown in figure 2.9b [9]. The fermion-antifermion pair of the Z^0 vacuum polarization can be either leptons or quarks including the top quark, t, whose mass is above that of the Z^0. This is an interesting aspect of these radiative corrections. Weak radiative corrections provide information about particles whose masses are above the energy scale of the process. An indirect measurement of the mass of the top quark can be made from the weak radiative corrections. A Higgs-antihiggs pair can also be formed in the Z^0 vacuum polarization loop. The Z^0 vacuum polarization correction creates an s-dependent Z^0 width

$$\Gamma_Z(s) = \frac{s}{M_Z^2}\Gamma_Z(s = M_z^2)$$

which causes the Z^0 cross section to peak 17 MeV below the Z^0 pole [12]. The Z^0 vacuum polarization also modifies the weak coupling as do other radiative corrections due

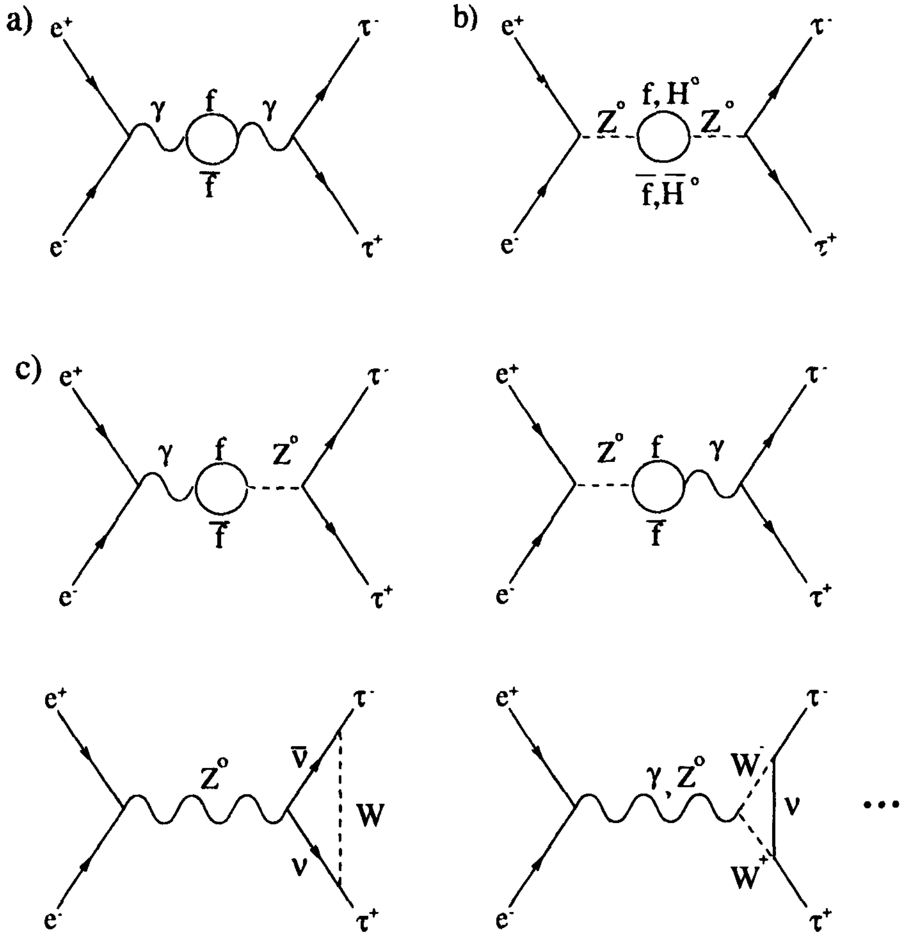

Figure 2.9: *The non-photonic radiative diagrams associated with the process* $e^+e^- \to \gamma, Z^0 \to \tau^+\tau^-$. *a) photon vacuum polarization, b)* Z^0 *vacuum polarization, c)* γ/Z^0 *mixing, heavy gauge boson exchange,* W^+W^- *production, and other diagrams.*

to γ/Z^0 interference and heavy gauge boson exchange shown in figure 2.9c [9]. These can be expressed in terms of a small correction, Δr_w:

$$G_F = \frac{\pi\alpha(M_Z^2)}{\sqrt{2}M_Z^2\sin^2\theta_W\cos^2\theta_W}\left(\frac{1}{1-\Delta r_w}\right). \tag{2.28}$$

The Z^0 vacuum polarization and vertex corrections can be expressed by replacing the vector and axial-vector coupling constants, g_v and g_a, by effective energy dependent couplings or form factors

$$g_v^f \rightarrow \hat{g}_v^f(s) \qquad\qquad g_a^f \rightarrow \hat{g}_a^f(s). \tag{2.29}$$

However, these effective couplings are nearly constant near the Z^0 pole. For leptons on the Z^0 peak, these effective couplings replace the Born level couplings with

$$\hat{g}_a^\ell = \sqrt{\rho}I_3^\ell \qquad\qquad \hat{g}_v^\ell = \sqrt{\rho}(I_3^\ell - 2q_\ell\sin^2\theta_W) \tag{2.30}$$

where at the Born level the ratio of the strength of the neutral current to the strength of the charged current, ρ, is equal to one. In the Improved Born Approximation, ρ becomes [13]

$$\sqrt{\rho} = \sqrt{1+\Delta\rho} \approx 1 + \frac{\Delta\rho}{2} \tag{2.31}$$

where

$$\Delta\rho \approx \frac{3G_F}{4\pi^2\sqrt{2}}\left[\frac{1}{2}M_t^2 - M_Z^2\sin^2\theta_W\ln\left(\frac{M_H}{M_Z}\right)\right]. \tag{2.32}$$

From this, it can be seen that $\Delta\rho$ depends quadratically on the mass of the top quark, M_t, but only logarithmically on the mass of the Higgs boson, M_H. The quadratic dependence of $\Delta\rho$ on the mass of the top quark, M_t, has enabled an indirect determination of the mass of the top quark using measurements made by the LEP experiments[2]: $M_t = 180^{+8}_{-9}{}^{+17}_{-20}$ GeV/c^2 [14] which is in agreement with the recent direct measurement by the CDF collaboration [15] and the D0 collaboration [16] resulting in an average mass of $M_t = 180 \pm 12$ GeV/c^2 [3]. The logarithmic dependence of $\Delta\rho$ on the mass of the Higgs boson is not strong enough to set any stringent limits on M_H. Using the LEP results in conjunction with the direct measurement of M_t from CDF and D0, a limit on M_H of

---

[2] The results reported in this thesis are used in this indirect determination of the top quark mass.

750 GeV/c^2 at a 95 percent confidence level has been set within the context of the Standard Model. Direct searches for the Higgs at LEP set a lower limit of 58.4 GeV/c^2.

The effective lepton vector and axial-vector couplings can be used to generate an effective $\sin^2\theta_W$

$$\frac{\hat{g}_v^\ell}{\hat{g}_a^\ell} = 1 - 4\sin^2\theta_{eff}^{lept} = 1 - 4(1 + \Delta k)s_o^2 \tag{2.33}$$

where s_o^2 is $\sin^2\theta_W$ corrected only for pure QED effects so Δk takes into account only the weak effects. In the limit of the quadratic M_t behavior, the radiative corrections $\Delta\rho$, Δr_w, and Δk are all related

$$\Delta\rho \approx -\frac{s_o^2}{c_o^2}\Delta r_w \approx -\left(\frac{c_o^2 - s_o^2}{c_o^2}\right)\Delta k \tag{2.34}$$

where $c_o^2 = 1 - s_o^2$. These radiative corrections have been completely calculated at the one-loop level including $\mathcal{O}(G_F^2 M_t^4)$ [9].

2.2.3 Summary of the Radiative Corrections

The electroweak non-photonic radiative diagrams modify the Born level cross section of the process $e^+e^- \rightarrow \tau^+\tau^-$ in equation 2.5 by replacing a) the fine structure constant, α, by an s-dependent coupling, b) the vector and axial-vector couplings g_v and g_a by s-dependent effective couplings $\hat{g}_v(s)$ and $\hat{g}_a(s)$ and c) the Z^0 width, Γ_Z, by an s-dependent width. These corrections result in the Improved Born Approximation. This corrected cross section, convoluted by a radiator function to take into account the purely photonic radiative diagrams, compares favorably to the $e^+e^- \rightarrow \tau^+\tau^-$ cross section measured at LEP.

Neglecting photonic corrections and γ and $\gamma - Z^o$ contributions, the asymmetries $\mathrm{A^{FB}}$, $\langle \mathrm{P}_\tau \rangle$, and $\mathrm{A^{FB}_{pol}}$ at the Z^0 pole are

$$\mathrm{A^{FB}} \approx \frac{3}{4}\mathcal{A}_e\mathcal{A}_\tau \equiv \frac{3\hat{g}_v^e\hat{g}_a^e\hat{g}_v^\tau\hat{g}_a^\tau}{(\hat{g}_v^{e2} + \hat{g}_a^{e2})(\hat{g}_v^{\tau 2} + \hat{g}_a^{\tau 2})} \tag{2.35}$$

$$\langle \mathrm{P}_\tau \rangle \approx -\mathcal{A}_\tau \equiv \frac{-2\hat{g}_v^\tau\hat{g}_a^\tau}{\hat{g}_v^{\tau 2} + \hat{g}_a^{\tau 2}} \tag{2.36}$$

$$\mathrm{A^{FB}_{pol}} \approx -\frac{3}{4}\mathcal{A}_e \equiv -\frac{3}{4}\frac{2\hat{g}_v^e\hat{g}_a^e}{(\hat{g}_v^{e2} + \hat{g}_a^{e2})}. \tag{2.37}$$

Tau decay channel	Branching Ratio
$\tau \rightarrow \rho\nu$	0.2488 ± 0.0051
$\tau \rightarrow e\nu\bar{\nu}$	0.1790 ± 0.0017
$\tau \rightarrow \mu\nu\bar{\nu}$	0.1744 ± 0.0023
$\tau \rightarrow 3hn\pi^o\nu$	0.1425 ± 0.0025
$\tau \rightarrow h\nu$	0.125 ± 0.004
$\tau \rightarrow h2\pi^o\nu$	0.0931 ± 0.0034
$\tau \rightarrow K^*\nu$	0.0145 ± 0.0012
$\tau \rightarrow h > 2\pi^o\nu$	0.0142 ± 0.0016

Table 2.1: *Table of the important decay products of the tau taken from the Particle Data group [3] and the Tau 94 Workshop [17]. The particle h refers to both pions and kaons.*

where

$$\mathcal{A}_\ell \equiv \frac{2\hat{g}_v^\ell \hat{g}_a^\ell}{(\hat{g}_v^{\ell^2} + \hat{g}_a^{\ell^2})} \qquad \text{for } \ell = e, \tau. \tag{2.38}$$

Figure 2.10 shows the effects of radiative corrections on these asymmetries. $\langle \mathrm{P}_\tau \rangle$ and $\mathrm{A}_{\mathrm{pol}}^{\mathrm{FB}}$ are the asymmetries least sensitive to radiative corrections because they vary most slowly with energy. This thesis presents a measurement of $\langle \mathrm{P}_\tau \rangle$ and $\mathrm{A}_{\mathrm{pol}}^{\mathrm{FB}}$ at the Z^0 pole.

2.3 Polarization Dependent Observables of the $\tau^\pm \rightarrow \rho^\pm \nu_\tau$ Decay

A calculation of $\langle \mathrm{P}_\tau \rangle$ and $\mathrm{A}_{\mathrm{pol}}^{\mathrm{FB}}$ using equations 2.15 and 2.17 requires the knowledge of the helicity of the tau. This helicity cannot be measured on an event-by-event basis. Instead, $\langle \mathrm{P}_\tau \rangle$ and $\mathrm{A}_{\mathrm{pol}}^{\mathrm{FB}}$ are extracted from kinematical observables sensitive to the polarization.

The most significant decay products of the tau are listed in table 2.1. This work focuses on the extraction of $\langle \mathrm{P}_\tau \rangle$ and $\mathrm{A}_{\mathrm{pol}}^{\mathrm{FB}}$ from the $\tau^\pm \rightarrow \rho^\pm \nu_\tau$ channel because it has a large branching fraction and the decay kinematics are sensitive to the polarization.

The angular distribution of the tau decay products depends on the polarization of the tau. A diagram of the weak decay of the tau to a ρ is shown in figure 2.11. The tau can have either positive (right-handed) or negative (left-handed) helicity. The ρ is a spin 1 meson with three possible spin projections: +1, 0 and -1. However, the requirement that the neutrino helicity is always left-handed implies that a ρ spin projection of +1 is not

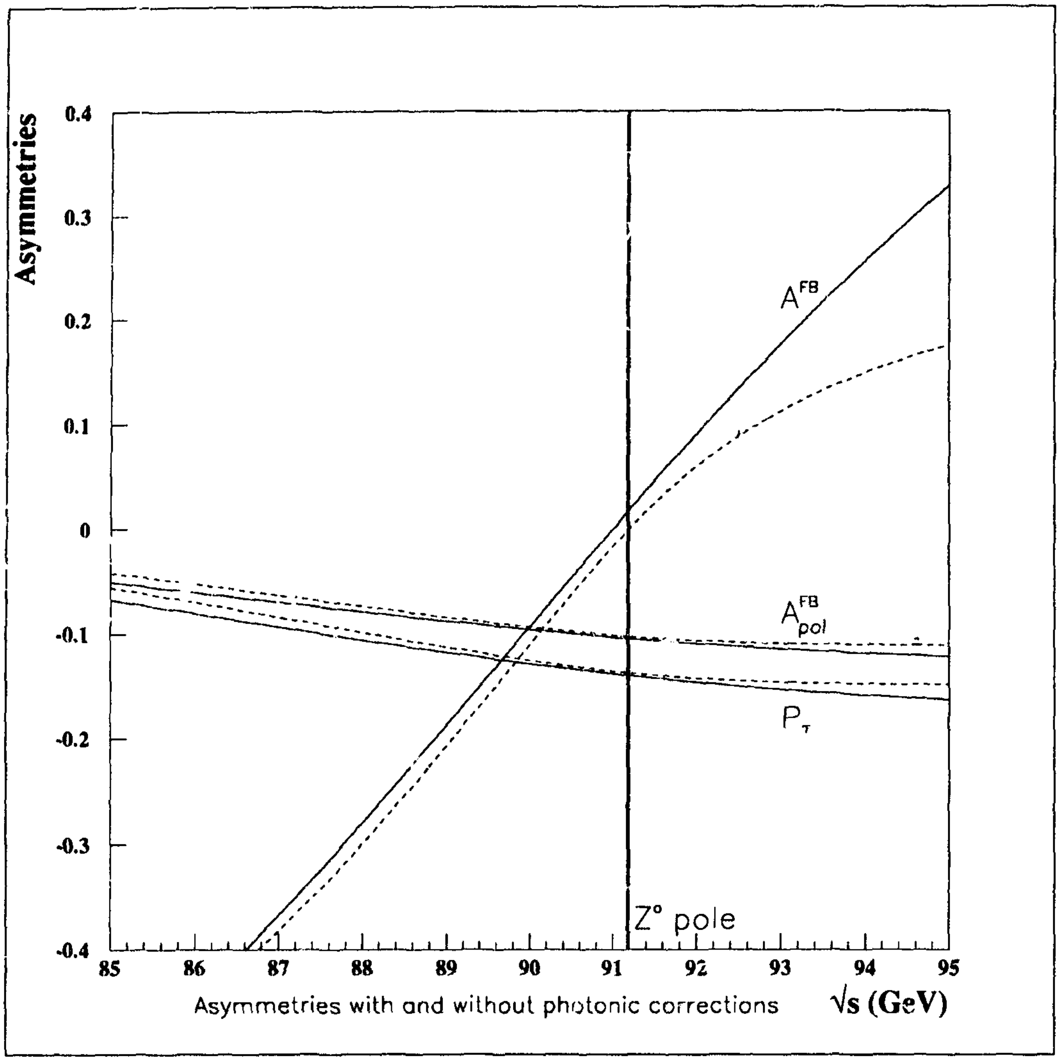

Figure 2.10: *The effect of applying the photonic corrections to the calculation of the asymmetries* A^{FB}, $\langle P_\tau \rangle$, *and* A^{FB}_{pol} *are shown by using the ZFITTER program [10] to calculate radiative corrections (the dashed lines in this figure).*

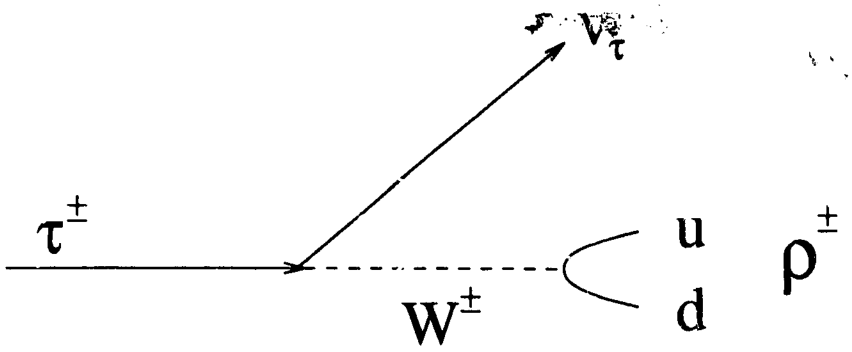

Figure 2.11: *The weak decay* $\tau^\pm \to \rho^\pm \nu_\tau$.

allowed. The possible spin projections of the decay $\tau^\pm \to \rho^\pm \nu_\tau$ are shown in figure 2.12 where θ^* is the opening angle of the ρ with respect to the tau flight direction in the tau rest frame. Figure 2.12a shows that the probabilities of left-handed taus decaying to ρ's with spin projection 0 and -1 are [18]

$$|\mathcal{M}_{-o}|^2 = \left(\frac{m_T}{m_\rho}\right)^2 \left[\frac{1-\cos\theta^*}{2}\right] \qquad |\mathcal{M}_{--}|^2 = 2\left[\frac{1+\cos\theta^*}{2}\right] \tag{2.39}$$

respectively. The subscripts on the $\mathcal{M}$ refer to the helicity of the τ and the spin projection of the ρ. The probabilities of right-handed taus decaying to ρ's with spin projection 0 and -1 as shown in 2.12b are [18]

$$|\mathcal{M}_{+o}|^2 = \left(\frac{m_T}{m_\rho}\right)^2 \left[\frac{1+\cos\theta^*}{2}\right] \qquad |\mathcal{M}_{+-}|^2 = 2\left[\frac{1-\cos\theta^*}{2}\right] \tag{2.40}$$

respectively. The total probability for taus to produce ρ with a spin projection of zero is

$$\frac{\sigma_L}{\sigma_L+\sigma_R}|\mathcal{M}_{-o}|^2 + \frac{\sigma_R}{\sigma_L+\sigma_R}|\mathcal{M}_{+o}|^2 = \frac{1}{2}\left(\frac{m_\tau}{m_\rho}\right)^2 [1 + \langle \mathrm{P}_\tau\rangle \cos\theta^*] \tag{2.41}$$

where $\langle \mathrm{P}_\tau\rangle$ was defined in terms of $\sigma_{L,R}$ in equation 2.15. Similarly, the probability to produce ρ's with a spin projection of -1 is

$$\frac{\sigma_L}{\sigma_L+\sigma_R}|\mathcal{M}_{--}|^2 + \frac{\sigma_R}{\sigma_L+\sigma_R}|\mathcal{M}_{+-}|^2 = 1 - \langle \mathrm{P}_\tau\rangle \cos\theta^*. \tag{2.42}$$

The ρ can be in either spin projection so equations 2.41 and 2.42 must be summed to provide the normalized decay distribution of the process $\tau^\pm \to \rho^\pm \nu_\tau$ [18]

$$\left.\frac{1}{N}\frac{dN}{d\cos\theta^*}\right|_\rho = \frac{1}{2}(1 + \alpha\langle \mathrm{P}_\tau\rangle \cos\theta^*) \qquad \alpha = \frac{m_\tau^2 - 2m_\rho^2}{m_\tau^2 + 2m_\rho^2} = 0.46 \tag{2.43}$$

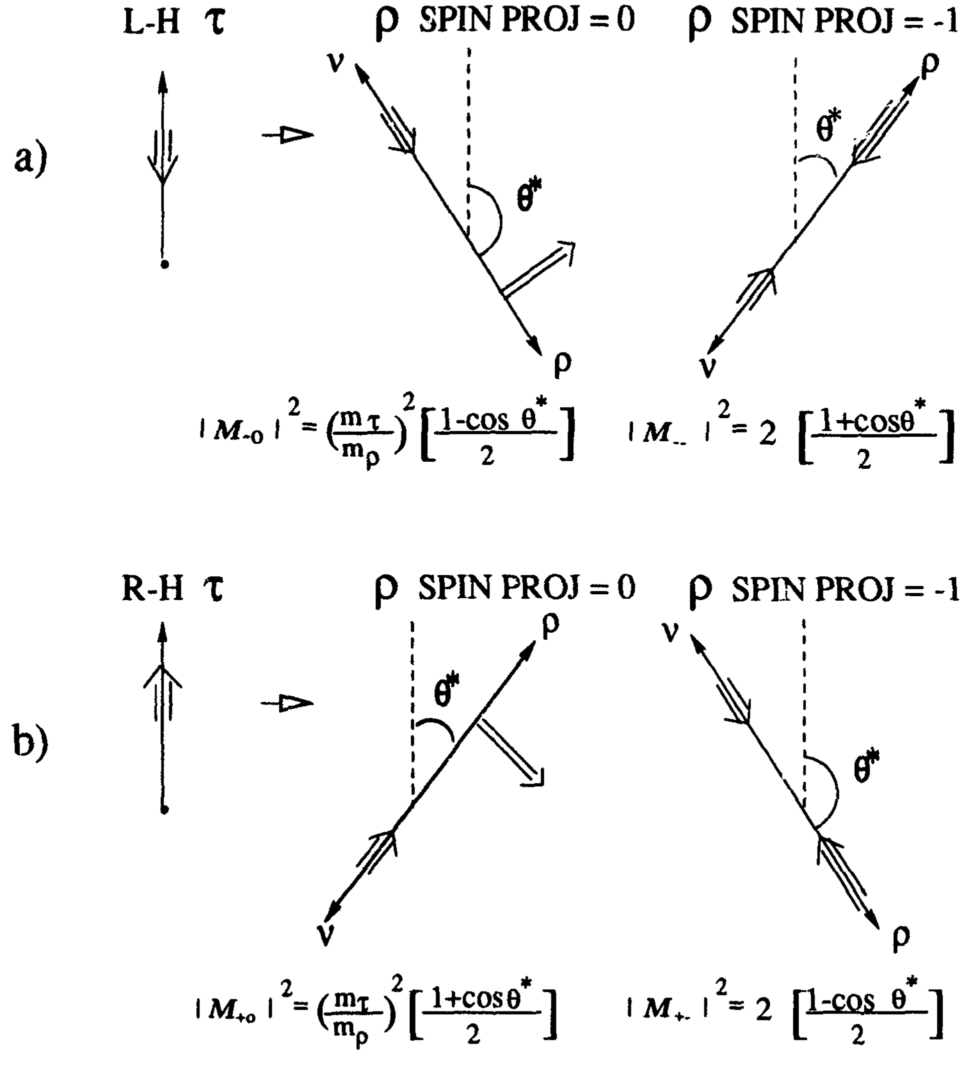

Figure 2.12: *The possible spin projections of the decay $\tau^\pm \rightarrow \rho^\pm \nu_\tau$. The double arrow indicates the spin state of the particle [18]. Taus can be either left-handed (figure a) or right-handed (figure b). $|\mathcal{M}_{-o}|^2$ and $|\mathcal{M}_{+-}|^2$ produce predominantly backward scattered ρ's while $|\mathcal{M}_{--}|^2$ and $|\mathcal{M}_{+o}|^2$ produce predominantly forward scattered ρ's. The subscripts on the $\mathcal{M}$ refer to the helicity of the τ and the spin projection of the ρ.*

where the mass of the ρ is m_ρ = 769.9 MeV/c^2 [3] and the mass of the τ is m_τ = 1777.1 MeV/c^2 [3]. The sensitivity of the variable $\cos\theta^*$ to the tau polarization in the $\tau^\pm \to \rho^\pm\nu_\tau$ channel is diminished relative to a spin zero particle by a factor α because the final spin projection of the ρ is not determined. This is to be compared with the $\tau^\pm \to \pi^\pm\nu_\tau$ channel which has the value $\alpha = 1$ because the charged pion is a spin zero particle. Figure 2.13 shows these decay distributions of the $\tau^\pm \to \pi^\pm\nu_\tau$ and $\tau^\pm \to \rho^\pm\nu_\tau$ channels. The loss of sensitivity in the $\tau^\pm \to \rho^\pm\nu_\tau$ can be regained by determining the spin projection of the ρ. This is accomplished by measuring the angular distribution of the decay products of the ρ. The $\rho^\pm$ decays to $\pi^\pm\pi^o$ with a branching ratio of nearly 100%. Both the charged and neutral pion are spin 0 particles and therefore the final state pions have one unit of orbital angular momentum. The possible spin combinations of the ρ decay are shown in figure 2.14 where ψ is the opening angle of the $\pi^\pm$ to the ρ flight direction in the ρ rest frame. The probability of the $\rho^\pm \to \pi^\pm\pi^o$ decay with a ρ spin projection of zero is [18]

$$|\mathcal{N}_{oo}|^2 \propto \cos^2\psi \tag{2.44}$$

while the probability of a ρ spin projection of -1 is [18]

$$|\mathcal{N}_{-o}|^2 \propto \sin^2\psi \tag{2.45}$$

where the subscripts on the $\mathcal{N}$ refer to the spin projection of the ρ and the spin projection of the $\pi^\pm$.

A Wigner rotation of angle η is performed to transform these amplitudes from the tau rest frame to the laboratory frame where the observables are measured [18]

$$\cos\eta = \frac{(m_\tau^2 - m_\rho^2) + (m_\tau^2 + m_\rho^2)\cos\theta^*}{(m_\tau^2 + m_\rho^2) + (m_\tau^2 - m_\rho^2)\cos\theta^*} \qquad \text{for } E_\tau >> m_\tau.$$

The resulting $\tau^\pm \to \rho^\pm\nu_\tau$ decay distribution is [19]

$$\frac{1}{N}\frac{d^2N}{d\cos\theta^* d\cos\psi} = W^+(1 + \langle \mathrm{P}_\tau \rangle) + W^-(1 - \langle \mathrm{P}_\tau \rangle) \tag{2.46}$$

where

$$W^+ = \frac{3}{8(m_\tau^2 + 2m_\rho^2)} \Bigg[\sin^2\psi \Bigg[(m_\tau \sin\eta\cos\frac{\theta^*}{2} - m_\rho \cos\eta\sin\frac{\theta^*}{2})^2 + m_\rho^2 \sin^2\frac{\theta^*}{2}\Bigg]$$

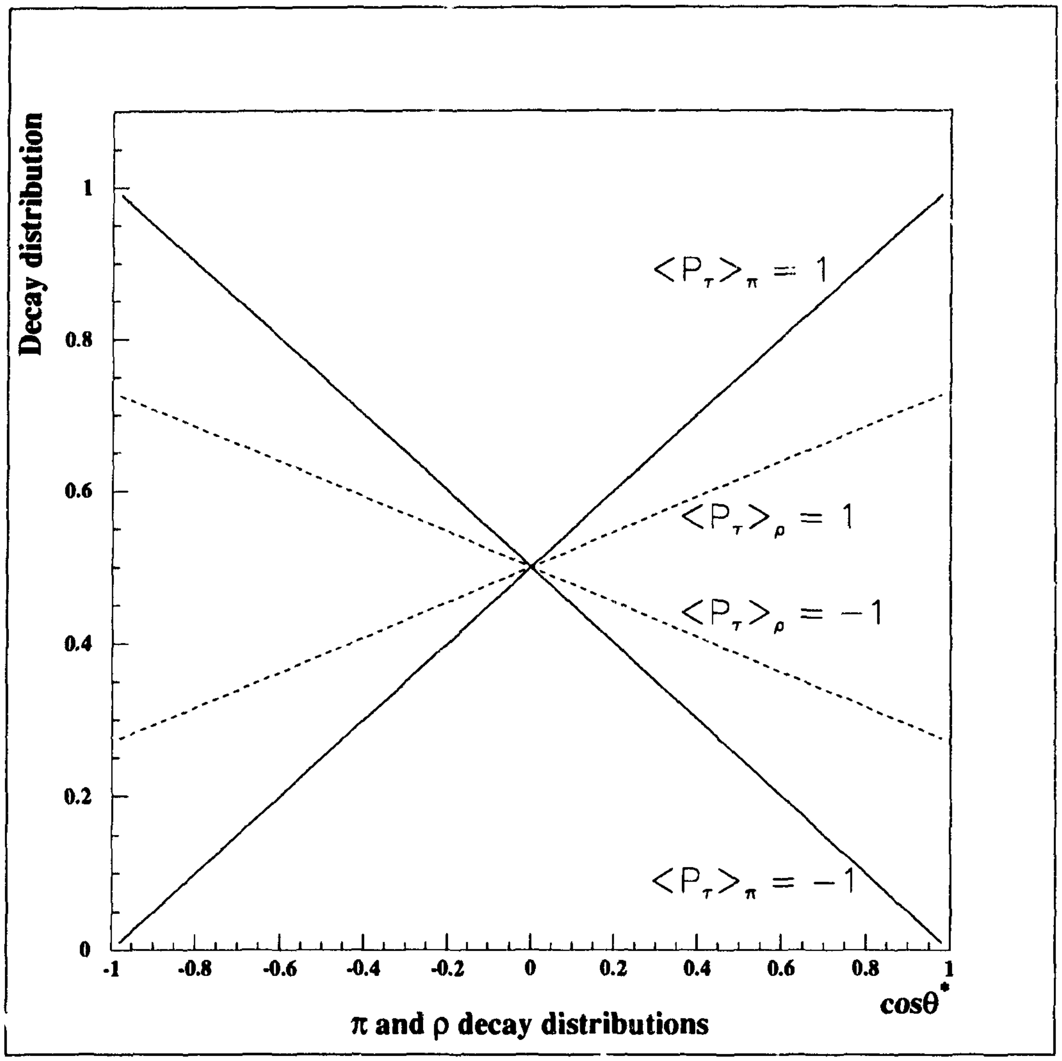

Figure 2.13: *The decay distribution of the* $\tau^\pm \rightarrow \pi^\pm \nu_\tau$ *process where* $\alpha = 1$ *in equation 2.43 (solid line) and the* $\tau^\pm \rightarrow \rho^\pm \nu_\tau$ *process with* $\alpha = 0.46$ *from equation 2.43 (dashed line) for* $\langle P_\tau \rangle = \pm 1$. *The sensitivity of the* $\tau^\pm \rightarrow \rho^\pm \nu_\tau$ *channel is diminished because the spin projection of the* ρ *is not determined.*

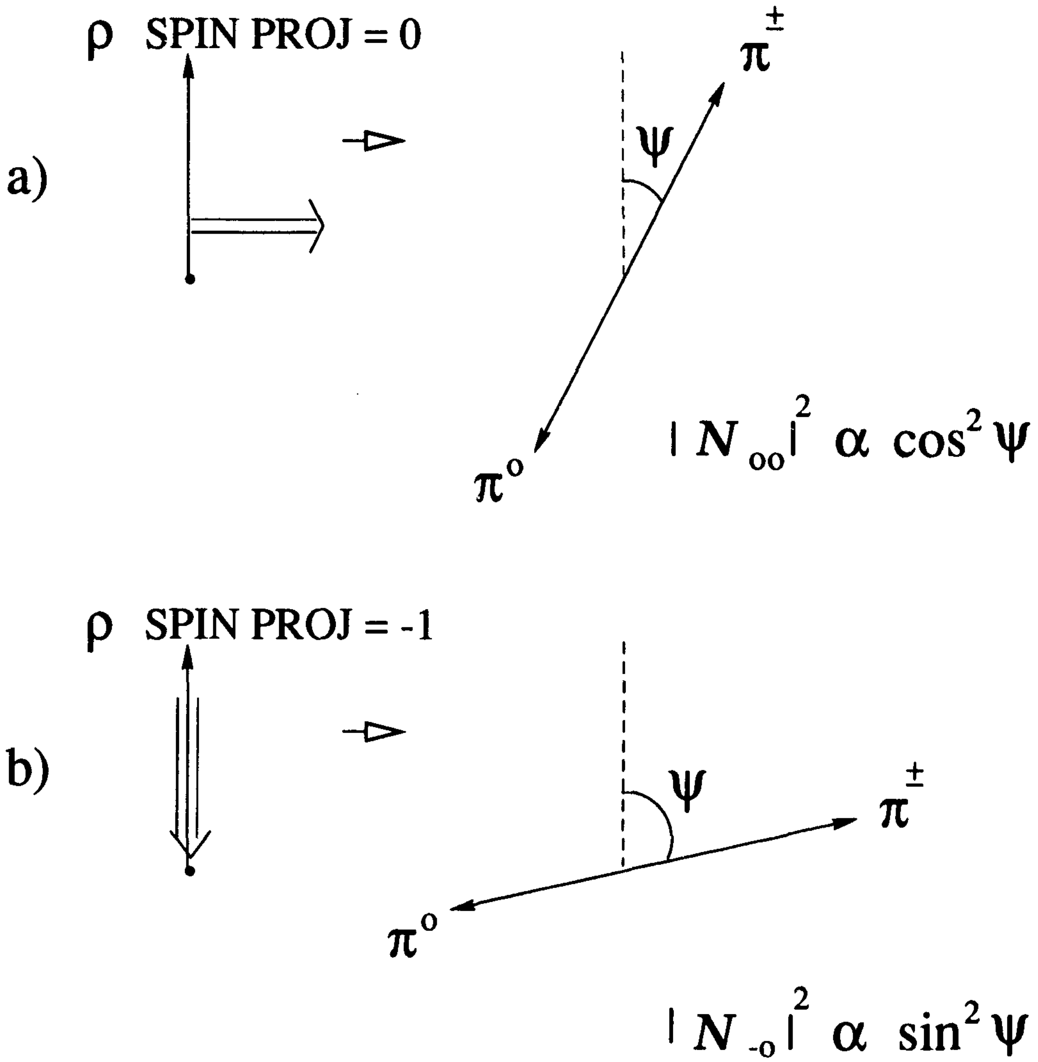

Figure 2.14: *Possible spin projections of the $\rho^{\pm} \rightarrow \pi^{\pm}\pi^{o}$ decay [18]. The ρ can have either a spin projection of zero (figure a) or a spin projection of -1 (figure b). The final state has one unit of angular momentum. The subscripts on the $\mathcal{N}$ refer to the spin projection of the ρ and the spin projection of the $\pi^{\pm}$.*

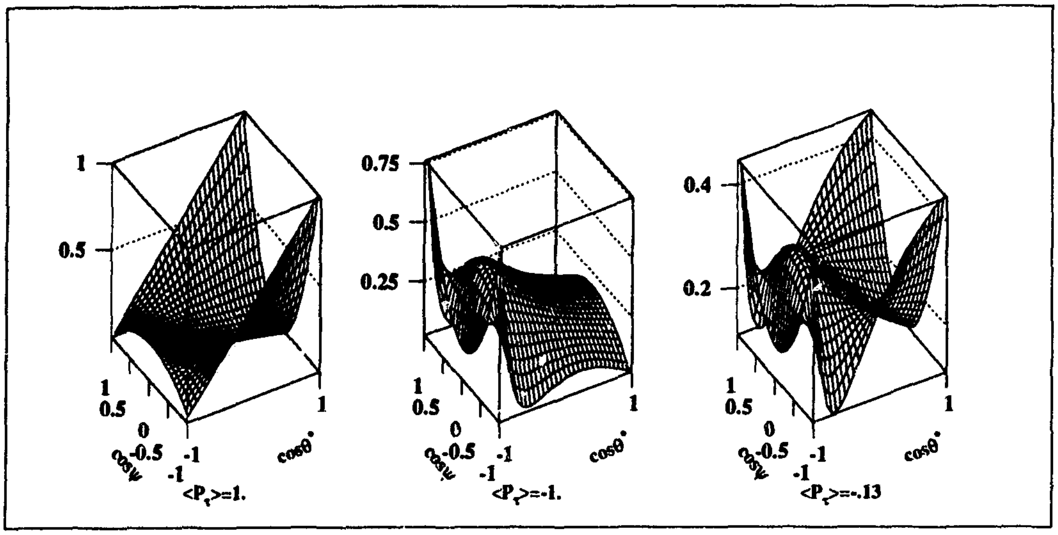

Figure 2.15: *The two-dimensional distribution of equation 2.46 when* $\langle \mathrm{P}_\tau \rangle = 1$, $\langle \mathrm{P}_\tau \rangle = -1$ *and* $\langle \mathrm{P}_\tau \rangle = -.13$. *The greatest sensitivity of* $\cos\theta^*$ *and* $\cos\psi$ *to a measurement of* $\langle \mathrm{P}_\tau \rangle$ *is at* $|\cos\theta^*| = 1$ *and* $|\cos\psi| = 1$.

$$+2\cos^2\psi\left(m_\tau\cos\eta\cos\frac{\theta^*}{2}+m_\rho\sin\eta\sin\frac{\theta^*}{2}\right)^2\Bigg]$$

$$W^- = \frac{3}{8(m_\tau^2+2m_\rho^2)}\left[\sin^2\psi\left[(m_\tau\sin\eta\sin\frac{\theta^*}{2}+m_\rho\cos\eta\cos\frac{\theta^*}{2})^2+m_\rho^2\cos^2\frac{\theta^*}{2}\right]\right.$$

$$\left.+2\cos^2\psi\left(m_\tau\cos\eta\sin\frac{\theta^*}{2}-m_\rho\sin\eta\cos\frac{\theta^*}{2}\right)^2\right].$$

The angles $\cos\theta^*$ and $\cos\psi$ in the $\tau^\pm \to \rho^\pm \nu_\tau$ decay can be expressed in terms of laboratory frame energies, the energy of the ρ (E_ρ) and the energy of the tau (E_τ),

$$\cos\theta^* = \frac{(2E_\rho/E_\tau - 1)m_\tau^2 - m_\rho^2}{(m_\tau^2 - m_\rho^2)} \approx 2E_\rho/E_{beam} - 1 \tag{2.47}$$

$$\cos\psi = \frac{2m_\rho^2 E_{\pi^\pm} - (m_\rho^2 + m_{\pi^\pm}^2 - m_{\pi^0}^2)E_\rho}{p_\rho\left(\left[m_\rho^2 - (m_{\pi^\pm} - m_{\pi^0})^2\right]\left[m_\rho^2 - (m_{\pi^\pm} + m_{\pi^0})^2\right]\right)^{\frac{1}{2}}} \approx \frac{E_{\pi^\pm} - E_{\pi^0}}{E_\rho} \tag{2.48}$$

assuming $E_\tau = E_{beam} >> m_\tau$.

Figure 2.15 shows the decay distribution of equation 2.46 when $\langle \mathrm{P}_\tau \rangle = \pm 1$ and -.13. This figure shows that right-handed taus peak at $\cos\theta^* = 1$ characterized by the existence of high energy ρ's while left-handed taus create softer ρ's. Equation 2.44 shows that a ρ

Tau decay channel	Sensitivity	Branching ratio	Weight
$\tau \to h\nu$	.60	.125	.33
$\tau \to \rho\nu$	.52	.250	.50
$\tau \to h2\pi^o\nu$	.24	.0931	.04
$\tau \to e\nu\bar{\nu}$	.22	.1788	.06
$\tau \to \mu\nu\bar{\nu}$	.22	.1746	.06

Table 2.2: *Table of sensitivities of some decay products of the tau to an extraction of* $\langle \mathrm{P}_\tau \rangle$ *taken from [19]. The weight is the sensitivity* $^2\times$ *branching ratio.*

with a spin projection of zero favors large $|\cos\psi|$ indicating a large difference in the energy between the $\pi^\pm$ and the π^o while equation 2.45 shows that a ρ with a spin projection of -1 favors small $|\cos\psi|$ and hence equal splitting between $\pi^\pm$ and π^o energy.

Table 2.2 shows the sensitivity of different tau decay channels to an extraction of the tau polarization [19]. Although $\tau^\pm \to \pi^\pm\nu_\tau$ is the most sensitive channel to an extraction of $\langle \mathrm{P}_\tau \rangle$, the large $\tau^\pm \to \rho^\pm\nu_\tau$ branching ratio dominates to give this channel the greatest weight of all decay channels. This work will extract $\langle \mathrm{P}_\tau \rangle$ and $\mathrm{A}^{\mathrm{FB}}_{\mathrm{pol}}$ from the $\tau^\pm \to \rho^\pm\nu_\tau$ channel. This will be accomplished by fitting the reconstructed $\cos\theta^*$ and $\cos\psi$ distributions from the OPAL data set with Monte Carlo samples which obey equation 2.46 and extracting $\langle \mathrm{P}_\tau \rangle$ in five bins of the tau scattering angle, $\cos\theta$. The values of the tau polarization, $\langle \mathrm{P}_\tau \rangle$, and the forward-backward polarization asymmetry, $\mathrm{A}^{\mathrm{FB}}_{\mathrm{pol}}$, of the $\tau^\pm \to \rho^\pm\nu_\tau$ data sample are extracted by fitting the resulting $\langle \mathrm{P}_\tau \rangle$ vs $\cos\theta$ distribution to a modified version of equation 2.14. Equation 2.14, which gives the dependence of the tau polarization as a function of the angle θ, can be rewritten as

$$P_\tau(\cos\theta) \approx -\left[\frac{\mathcal{A}_\tau(1+\cos^2\theta)+2\mathcal{A}_e\cos\theta}{1+\cos^2\theta+\frac{8}{3}\mathrm{A}^{\mathrm{FB}}\cos\theta}\right] \approx \left[\frac{\langle \mathrm{P}_\tau \rangle(1+\cos^2\theta)+2\left(\frac{4}{3}\mathrm{A}^{\mathrm{FB}}_{\mathrm{pol}}\right)\cos\theta}{1+\cos^2\theta+\frac{8}{3}\mathrm{A}^{\mathrm{FB}}\cos\theta}\right]. \tag{2.49}$$

A two parameter χ^2 fit is made of the OPAL $\tau^\pm \to \rho^\pm\nu_\tau$ tau polarization data as a function of $\cos\theta$ to extract $\langle \mathrm{P}_\tau \rangle$ and $\mathrm{A}^{\mathrm{FB}}_{\mathrm{pol}}$.

Chapter 3

The OPAL Detector at LEP

The European Centre for Nuclear Research (CERN) is located in Geneva, Switzerland. Several particle accelerators have been operated at the CERN complex including the $p\bar{p}$ collider which first produced the weak vector bosons $W^{\pm}$ and Z^0 in 1983 and the Large Electron Positron collider, LEP [20], which was commissioned in 1989. The 27 km circumference LEP accelerator, shown in figure 3.1, was designed to accelerate electrons and positrons to center-of-mass energies between 80 and 200 GeV. So far, it has operated with center-of-mass energies in the range 88 to 95 GeV producing particles through the reaction $e^+e^- \rightarrow \gamma, Z^o \rightarrow f\bar{f}$ where the fermions, f, are quarks or leptons. The electrons and positrons accelerated in LEP collide at four equally spaced interactions points around the LEP ring where the collisions are recorded by the four general-purpose detectors ALEPH [21], DELPHI [22], L3 [23] and OPAL [24]. This chapter will provide details on the LEP accelerator and the OPAL detector.

3.1 Injection into LEP

Positrons are produced by pair production using a 200 MeV e^- beam directed onto a target. The positrons are stripped off and stored with electrons from a second source in the electron-positron accumulator (EPA). The particles emerge from the EPA collected into bunches and are accelerated in the proton synchrotron ring (PS) to an energy of 3.5 GeV and then in the super proton synchrotron ring (SPS) to 20 GeV where they are then injected in to the LEP accelerator. LEP accelerates these electron and positron bunches

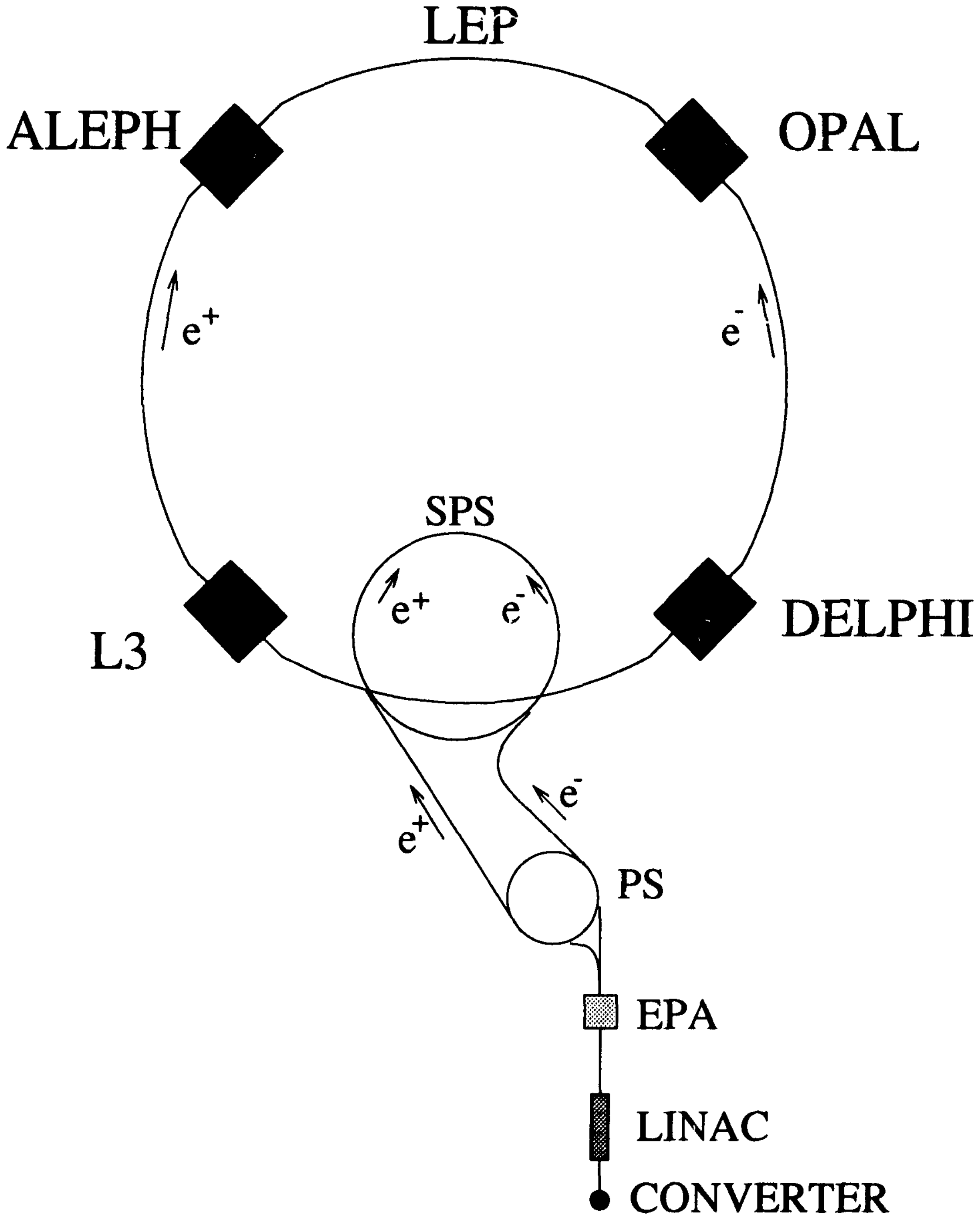

Figure 3.1: *Diagram of the LEP accelerator complex at the CERN laboratory in Geneva (Not to scale). The LEP accelerator is a nearly circular ring with a 27 km circumference. There are four instrumented interaction points: ALEPH, DELPHI, L3, and OPAL.*

to energies of approximately 45 GeV before they are brought into collision. The beams are constrained to a nearly circular orbit by dipole magnets while quadrupole magnets with alternating poles have the net effect of focusing the beam in both the horizontal and vertical plane.

3.2 LEP Operation

The rate, R, of the process $e^+e^- \rightarrow f\bar{f}$ depends on the cross section, σ, of the process and the property of the beam of particles called the luminosity, $\mathcal{L}$. The luminosity of the electron-positron collisions in LEP varies linearly with the current of the beams and depends on the revolution frequency of LEP (11.25 kHz), on the number of particles in each beam, and on the size of the beams. A typical luminosity for LEP is 1×10^{31} cm^{-2}s^{-1} with a record peak luminosity of 2.2×10^{31} cm^{-2}s^{-1}. The rate of the process $e^+e^- \rightarrow f\bar{f}$ is $R = \mathcal{L}\sigma$. A detector at LEP typically records 1 multihadronic Z^0 decay every 2 seconds when LEP is operating at its design luminosity of 1.6×10^{31} cm^{-2}s^{-1}.

From 1989 to 1992, LEP operated in the "4 × 4 bunch mode" where four bunches of electrons 22 μs apart and 4 bunches of positrons with the same spacing were accelerated in opposite directions and collided at each of the four interaction points simultaneously. There were typically approximately 10^{12} particles per bunch. LEP operated from 1992-1994 with the "8 × 8 pretzel scheme" where the number of bunches was increased from four to eight. Outside of the four interaction regions, the bunches were separated to prevent unwanted collisions.

The LEP collider has operated at various energies near and on the Z^0 pole but most of the data has been collected at the Z^0 peak (91.3 GeV) and at ±2 GeV from the Z^0 peak (at 89.4 GeV and 93.0 GeV).

The measurement of the mass of the Z^0 and its width depends on an accurate determination of the LEP beam energy. Since 1993, the LEP beam energy has been calibrated using the method of resonant depolarization [25]. Synchrotron radiation causes a transverse polarization of the electrons in a direction opposite to the dipole magnetic field (Sokolov-Ternov effect [26]). The electron spin precesses in the magnetic field with a characteristic frequency. The number of spin precessions per orbit around LEP is given by the spin tune ν which is related to the beam energy

$$\nu = a_e\gamma = a_e\frac{E_{beam}}{m_e} \tag{3.1}$$

where a_e is the electron anomalous magnetic moment. An oscillating radial magnetic field from an RF magnet is used to perturb the spin alignment. If this radial field is in phase with the precession of the electron spin vector, the polarization vector is rotated into the horizontal plane and the vertical polarization is lost. The energy is determined through equation 3.1 because the spin tune is related to the ratio of the depolarization frequency to the revolution frequency. This method of obtaining the beam energy has an intrinsic resolution of about 200 keV. The largest errors come from extrapolating the value of the beam energy in between the measurements with resonant depolarization. This gives an uncertainty on the beam energy of 1 to 2 MeV.

3.3 The OPAL Detector

The OPAL detector was designed as a magnetic spectrometer capable of measuring the momentum of charged particles and capable of identifying particles through their mass and as a hermetic apparatus which provides calorimetry information to determine the energy of leptons, photons, and hadrons. It is a cylindrically shaped detector with a barrel region covering approximately $0 \leq |\cos\theta| \leq 0.81$ and two endcap regions covering the remaining solid angle (see figure 3.2). The e^+e^- collisions occur within a vacuum which is contained by a 10.7 cm diameter berylium pipe at the core of the OPAL detector. The inner detector operates within a 4.36 m diameter solenoidal magnet providing a 0.435 T magnetic field along the z-axis[1] of the detector. The charged particle tracking detectors which make up the inner detector operate within this magnetic field. The electromagnetic and hadronic calorimetry and the muon detectors make up the outer detector.

---

[1] The z-axis is along the e^- beam direction while θ and ϕ are the polar and azimuthal angle as shown in figure 3.3.

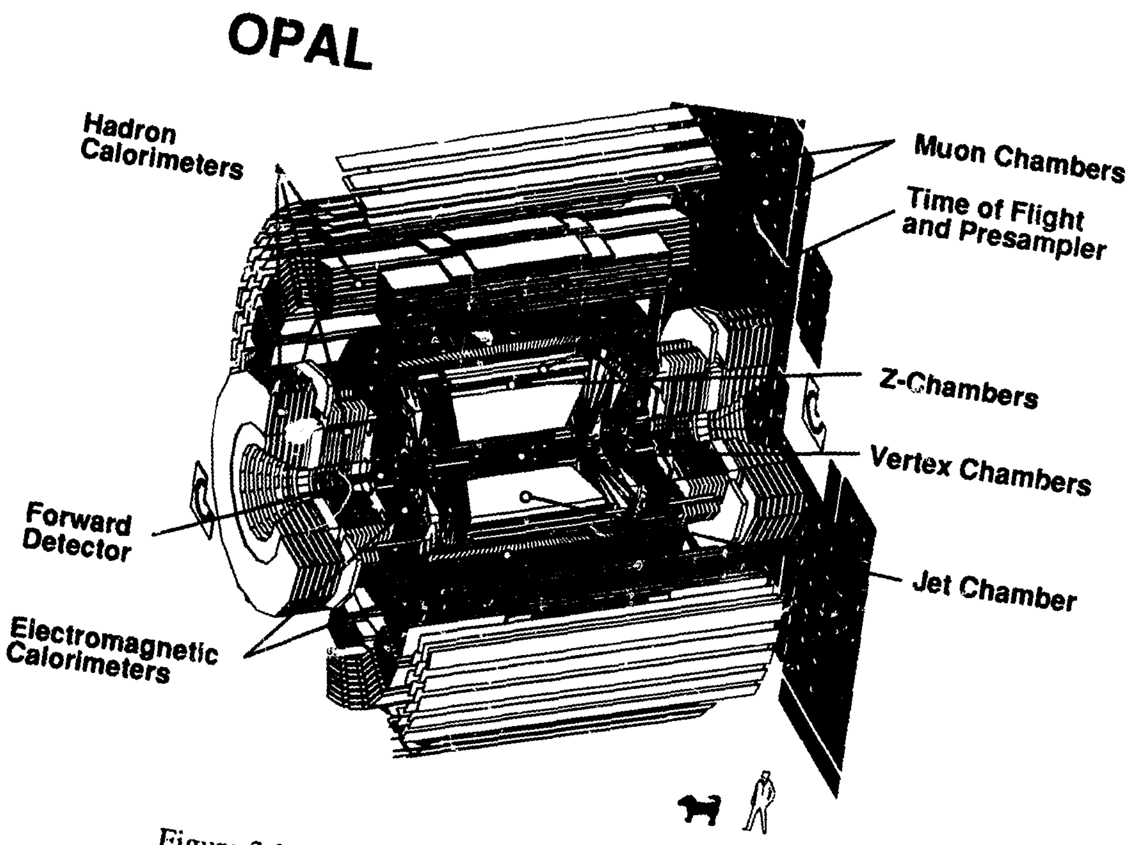

Figure 3.2: *A schematic of the OPAL detector at LEP.*

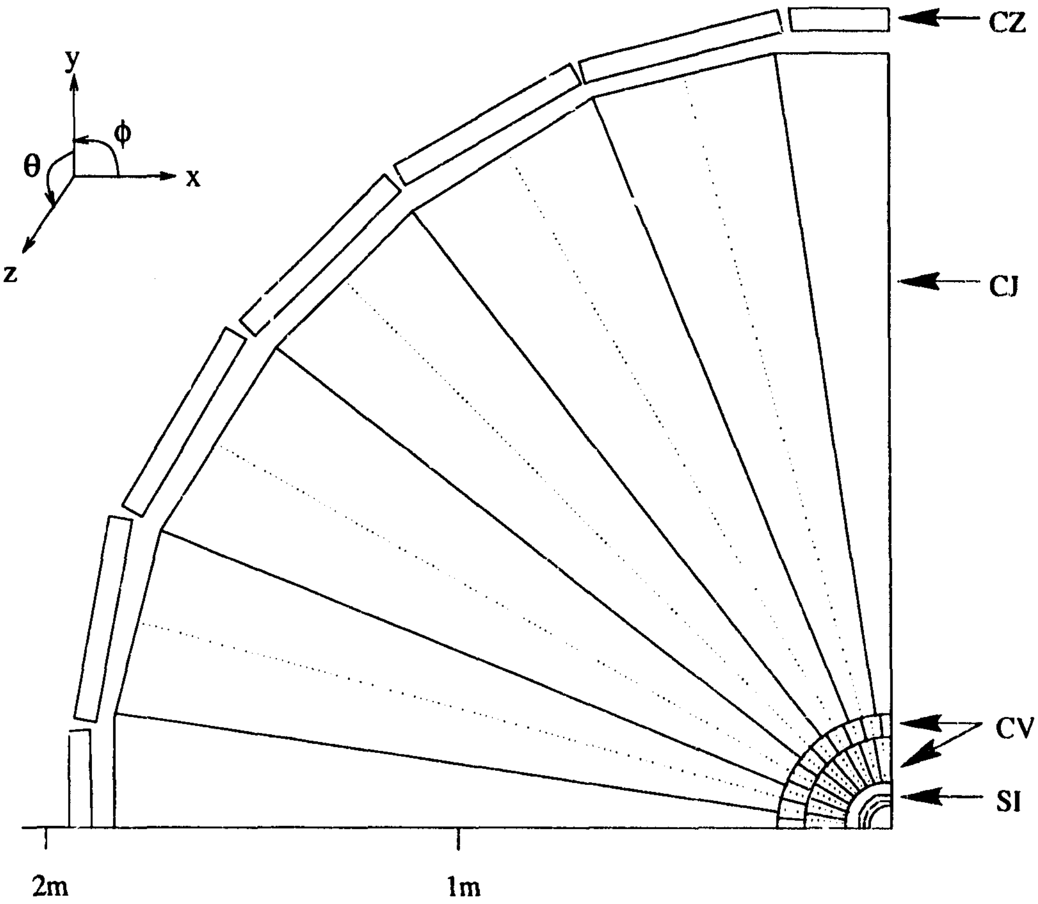

Figure 3.3: *x-y projection of a quarter of the central tracking detector system. The coordinate system of the OPAL detector is also shown.*

3.3.1 Central Tracking Detector System

The central tracking detectors are a series of cylindrical, concentric charged particle trackers surrounding the beam pipe. Diagrams showing the x-y and r-z projections of the central tracking detectors are shown in figures 3.3 and 3.4 respectively. The central detectors measure or "track" the trajectory of charged particles as they curve under the influence of the solenoid's magnetic field. A straight line extrapolation of the trajectory is made when the charged particles leave the influence of the magnetic field. The trajectory of the charged particle is referred to as its track.

Nearest to the beam pipe is the silicon strip microvertex detector (SI) consisting of

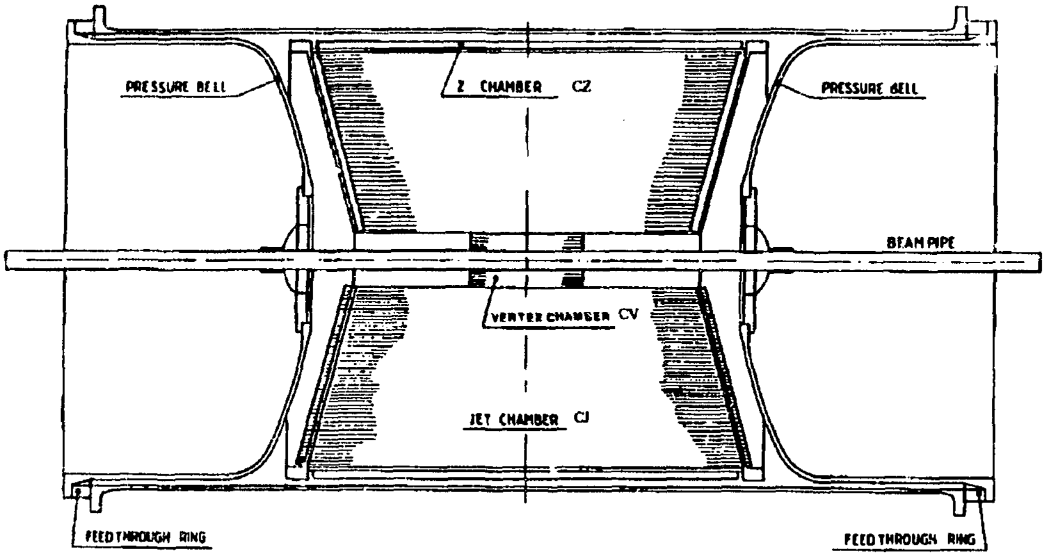

Figure 3.4: *r-z projection of the OPAL central tracking detector system. This assembly is approximately 8 meters long.*

two concentric barrels of silicon wafers. The inner barrel contains eleven ladders of three wafers while the outer barrel has fourteen similar ladders. Incident charged particles passing through the wafers are measured in the x-y coordinates with an intrinsic resolution of 4 μm. The silicon microvertex detector was upgraded in 1994 with back-to-back silicon wafers providing both an r-ϕ and r-z measurement of charged particles.

Surrounding the silicon microvertex detector is the central vertexing detector (CV), a one meter long cylindrical drift chamber extending in radius from 10 cm to 24 cm. It consists of an inner layer of 36 cells with axial wires (parallel to the beam) and an outer layer of 36 cells with stereo wires at a 4^{o} angle to the z-axis. It operates in a 88.2% argon, 9.8% methane, 2.0% isobutane gas mixture within a 4 bar pressure vessel. An r-ϕ measurement of charged particles is made with the axial wires with a resolution $\sigma_{r\phi} \approx 55$ μm while a z measurement of $\sigma_{rz} \approx 700$ μm can be made with the stereo wires.

Concentric to CV and operating in the same pressure vessel is the central jet chamber (CJ). It is a drift chamber approximately 4 m in length with an inner radius of 25 cm and an outer radius of 185 cm. There are 24 identical sectors where each sector consists of an anode plane of 159 sense wires separated by two cathode planes. The wire planes are radial and the wires run parallel to the z-axis. CJ can provide r, ϕ, and z information on charged tracks from the position of the wire collecting the charge, the drift time to the wire, and the ratio of charge accumulated at both ends of the wire respectively. CJ has an r-ϕ resolution of 135 μm and an z resolution of 6 cm. The 159 sense wires provide multiple sampling of the position of the charged particles as they curve through the jet chamber due to the influence of the magnet. This enables a measurement of the curvature of the particle and, knowing the strength of the magnetic field, the particle's momentum. CJ has a momentum resolution of

$$\frac{\sigma_p}{p^2} \approx 10^{-3}\text{GeV}^{-1}.$$

The sum of all the charge accumulated gives a measurement of the specific energy loss, dE/dx, of a charged particle passing through the gas of the chamber. The specific energy loss of a charged particle is velocity dependent. Therefore, a measurement of dE/dx combined with a measurement of the momentum provides a measure of the mass of the charged particle and hence particle identification over the momentum range of approximately 0.1 GeV/c to 45 GeV/c.

A precise measurement of the z-coordinate of charged particles is made with the z-chambers (CZ) also contained within the pressure vessel. CZ consists of twenty four 4 m long by 50 cm wide by 59 mm thick drift chambers arranged concentrically about CJ. Each chamber is divided into 8 cells along the z direction. There are 6 sense wires at the the center of each cell running perpendicular to the z direction. Drift time and ire position provide a z measurement with a resolution of approximately 300 μm. Charge division along the wire hit can provide an approximate ϕ measurement with a resolution of 1.5 cm.

3.3.2 The Outer Detector

The solenoidal coil surrounds the central tracking chambers. The first detector outside the coil is the Time-of-Flight (TOF). The TOF consists of 160 scintillating counters arranged concentrically around the inner detector. The TOF records the time of flight of particles coming from the interaction point. The TOF's primary function is to identify cosmic ray background which will have a different timing than particles originating from the e^+e^- interaction point.

The remaining subdetectors in the barrel region also have analogs in the endcap. These are the electromagnetic calorimeters followed by hadronic calorimeters and muon chambers. The hadronic calorimeters are made of 8 layers of iron slabs interleaved with 9 layers of streamer tubes. The iron provides a return yoke for the magnetic field. The barrel electromagnetic calorimeter is magnetically shielded by the barrel hadronic calorimeter. This is not the case for the endcap electromagnetic calorimeter.

The electromagnetic calorimeter (ECAL) is designed primarily to measure the energy and position of electrons, positrons, and photons. The barrel calorimeter (EB), shown in figure 3.5, consists of a cylindrical array of 9440 10 cm $\times$ 10 cm $\times$ 37 cm lead glass Cerenkov counters of 24.6 radiation lengths in depth surrounding the TOF detector and covering the region $|\cos\theta| < 0.82$. These blocks are oriented in a near-pointing geometry such that the face of each block points to 3 cm to the side of the interaction region. EB is segmented into 59 blocks along the z-axis and 160 blocks in ϕ; each block covers 40 mrad in ϕ with similar coverage in θ. The endcap electromagnetic calorimeters (EE) are dome-shaped arrays of 1132 lead glass blocks oriented along the z-axis covering the region $0.81 < |\cos\theta| < 0.98$.

Particles entering the lead glass undergo electromagnetic interactions that produce dense showers of photons and electron-positron pairs due to bremsstrahlung radiation of the particles and pair production of the photons. The charged particles from the showers emit Cerenkov radiation if the velocity of the particle is greater than c/n (the speed of light/index of refraction of the lead glass blocks) which is observed by the phototubes. The lead glass blocks have an intrinsic energy resolution of $\sigma_E/E \approx 5 - 6\%/\sqrt{E}$. However, the two radiation lengths of the solenoidal coil in front of the ECAL can cause particles to start showering before entering the ECAL thereby degrading the resolution to $\sigma_E/E \approx 12\%/\sqrt{E}$. For this reason, presampling devices exist in front of the ECAL blocks in both the barrel and endcaps to sample the energy, measure the position, and identify

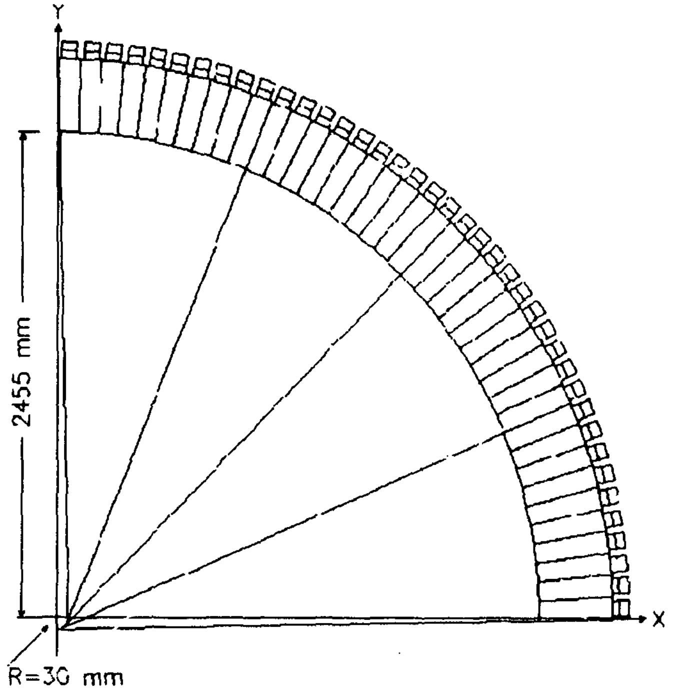

Figure 3.5: *An r-ϕ quadrant of the OPAL barrel electromagnetic calorimeter. The ECAL blocks point 30 mm to the side of the interaction point to avoid the loss of particles through the cracks of the ECAL.*

the electromagnetic showers which were initiated in the coil. The barrel electromagnetic presampler (PB) consists of a cylinder of 16 chambers having two layers of limited streamer mode tubes with the wires running along the beam direction. The endcap electromagnetic presampler (PE) has 32 thin multiwire chambers arranged in an umbrella shape.

The electrons and photons generally are completely absorbed in the ECAL. However hadrons may or may not interact in the ECAL and usually emerge from the ECAL. Immediately after the ECAL, the iron return yoke of the solenoidal coil is instrumented to provide hadronic calorimetry (HCAL). Hadronic showers result from the interaction of hadrons with nuclei. The hadronic calorimeter consists of 8 alternating layers of 10 cm thick iron and 9 layers of limited streamer chambers both in the barrel and endcaps of OPAL providing approximately 4 interaction lengths of absorber. The energy resolution of this calorimeter is approximately $\sigma_E/E \approx 140\%/\sqrt{E}$.

Most hadrons are absorbed by the HCAL, but some may leak out or "punch through" to the muon chambers. Muons do not interact strongly and are massive enough that electromagnetic showers are suppressed at LEP energies. A system of wire chambers surrounds the HCAL to detect the penetrating muons. The barrel muon detector (MB) consists of 110 large area drift chambers surrounding the HCAL while the endcap muon detectors (ME) have four layers of limited streamer tubes perpendicular to the beam. Muons are identified by matching tracking information with muon chamber detection information providing a position measurement of muons of $\sigma_\phi \approx 1.5$ mm and $\sigma_z \approx 2$ mm in the barrel and a resolution of 3 mm in the endcaps.

3.3.3 Luminosity Detectors

The luminosity of the electron-positron beams is measured in the forward and backward region of OPAL from the small angle Bhabha scattering process $e^+e^- \rightarrow e^+e^-$. A lead-scintillator forward detector FD was first installed in OPAL providing a luminosity measurement with an error of 0.6%. In 1993, a high precision silicon-tungsten sampling calorimeter was installed which reduced the luminosity error to $< 0.1\%$. A precise measurement of the luminosity is crucial to the proper determination of the overall normalization of cross sections. It will however cancel out of the calculation of the polarization and forward-backward polarization asymmetry.

3.3.4 Data Acquisition

A triggering system selects e^+e^- collisions and synchronizes the recording of information from various subdetectors into what is referred to as an event. The central tracking chambers, TOF, ECAL, and muon chambers provide signals to the triggering system which decides if a collision has occurred at the interaction point. Each subdetector has one or more local system crates (LSC) which read in the data coming from the subdetector for every triggered event. The information from each detector's LSC is sent to an "event builder" which collates the data into a single event record. The event is passed on to the "filter system" where a partial interpretation of the information or "reconstruction" of the event is performed to classify the event as a valid physics event or as a background event, such as a cosmic ray or the interaction of a particle with residual gas in the beam pipe. Events are stored onto recording media. A full reconstruction of the event is performed with the ROPE system (Reconstruction of OPAL Events) both during data taking (online), to verify data quality, or later with the latest calibration constants. The data are subject to multiple passes of the ROPE system with the most recent calibration constants.

3.3.5 OPAL Performance

The OPAL detector first started recording e^+e^- collisions in August 1989 and has continued to accumulate data until the end of phase I of LEP in October 1995. It has collected data at center-of-mass energies between 88 GeV and 95 GeV. The e^+e^- collisions generated by LEP in 1992 and 1994 were produced solely at the Z^0 peak. A total of 5.1 million visible Z^0's (4.5 million multihadronic events and 0.6 million charged leptons) were produced at the OPAL interaction point for a total integrated luminosity of 173 pb^{-1}. Figure 3.6 shows the integrated luminosity recorded at OPAL as a function of time. This thesis studies $e^+e^- \rightarrow \tau^+\tau^-$ events recorded at OPAL between 1990 and 1994.

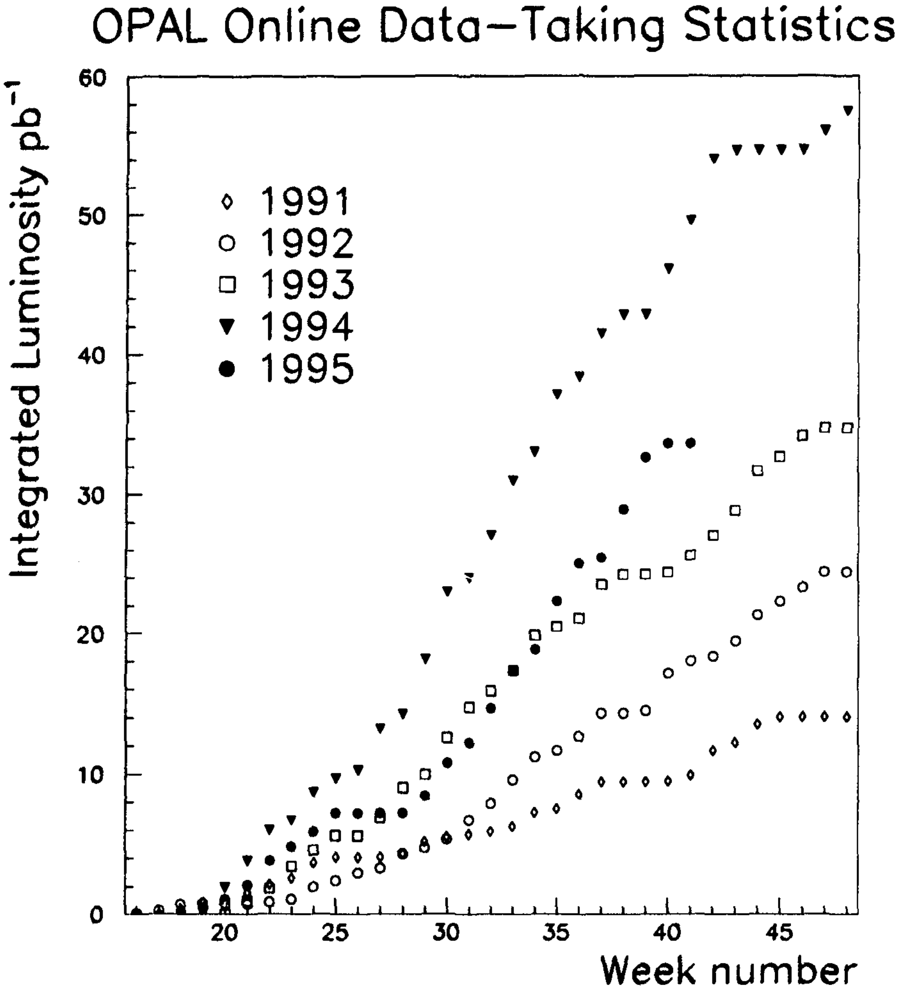

Figure 3.6: *Integrated luminosity recorded at the OPAL detector between 1991 and 1995. The "Week number" refers to the number of weeks since the start of the LEP run in a particular year.*

Chapter 4

The $\tau^{\pm} \rightarrow \rho^{\pm}\nu_{\tau}$ Selection

An event selection is presented which isolates the resonance $\rho^{\pm}(770)$ in the barrel region ($|\cos\theta| \leq 0.68$) of the OPAL detector. The decay chain of the $\rho^{\pm}$ is shown in figure 4.1. A colliding $e^{+}e^{-}$ pair can produce a $\tau^{+}\tau^{-}$ pair where a tau can decay to a $\rho^{\pm}$ and a neutrino with a branching ratio of 25 percent. The $\rho^{\pm}$ almost exclusively decays to a charged pion and a neutral pion. The neutral pion subsequently decays to two photons nearly 100 percent of the time.

The two photons coming from the decay of the π^{0} deposit all of their energy in the electromagnetic calorimeter while the charged pion may or may not deposit a measurable amount of energy in the ECAL. The event selection identifies clusters of energy in the ECAL and associates these clusters either to the charged pion or the neutral pion of the ρ decay. Whenever possible, a π^{0} is reconstructed based on information from the ECAL and the barrel presampler. The ρ events are reconstructed based on the tracking information for the charged pion and ECAL information from the neutral pion.

A tau preselection defined by OPAL [27] isolating the $e^{+}e^{-} \rightarrow \tau^{+}\tau^{-}$ decays from the $e^{+}e^{-} \rightarrow f\bar{f}$ process is first presented followed by the $\tau^{\pm} \rightarrow \rho^{\pm}\nu_{\tau}$ event selection.

4.1 The Tau Preselection

The first step in identifying $\tau^{\pm} \rightarrow \rho^{\pm}\nu_{\tau}$ events from the $e^{+}e^{-} \rightarrow f\bar{f}$ process at LEP is to isolate a pure sample of $e^{+}e^{-} \rightarrow \tau^{+}\tau^{-}$ events. The tau preselection [27] is based on the expected appearance of the topology of tau pair events. Tau pair events coming

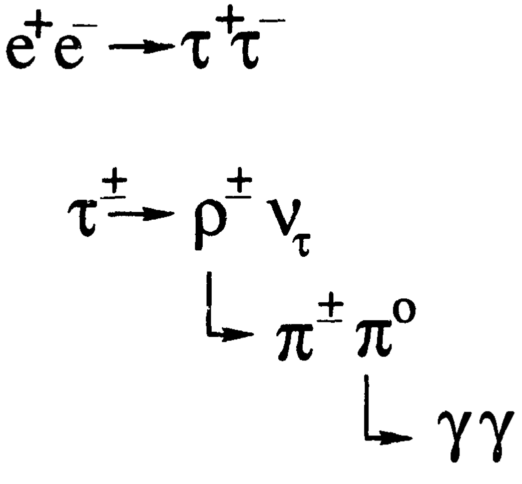

Figure 4.1: *The decay chain of the $\rho^\pm(770)$ to a charged pion and neutral pion with the subsequent decay of the neutral pion to two photons.*

from the decay $e^+e^- \rightarrow \tau^+\tau^-$ are observed in the OPAL detector as two back-to-back narrow jets of particles with a charged particle multiplicity of one to six per jet. There is a sizable missing energy and an unbalanced transverse momentum due to the presence of undetectable neutrinos in the decay of the tau.

Therefore, the following selection criteria are used to identify tau pairs coming from the process $e^+e^- \rightarrow \tau^+\tau^-$. All candidate tau events must have exactly two jets of particles where the tracks of charged particles and clusters of energy observed in the ECAL are found inside a cone with a half-angle of 35°. Each tau jet must have at least one charged track with the following quality criteria: it must have a) at least 20 hits in the CJ detector with the first hit occurring at a distance $r < 75$ cm, b) a minimum momentum transverse to the beam axis of 100 MeV/c, c) the distance of closest approach to the beam axis in the $r - \phi$ plane of $|d_o| < 2$ cm and the distance along the beam axis of the closest approach to the interaction point of $|z_o| < 20$ cm. The total track momentum and ECAL energy associated with a candidate tau jet must be greater than one percent of the beam energy. The average $|\cos\theta|$ of the jets is required to be less than 0.68 corresponding to the barrel region of the OPAL detector. This fiducial requirement discards over 40% of the tau pair events but ensures a region of uniform calorimeter response.

Several requirements are imposed to reject background events contaminating the $e^+e^- \rightarrow \tau^+\tau^-$ preselection.

Cosmic Ray Rejection

Cosmic ray particles do not come from the interaction point so are rejected by requiring tracks to originate at the interaction point. A tau candidate is kept if at least one of the charged tracks has a $|d_o| < 0.5$ cm, a $|z_o| < 20$ cm, and the magnitude of the average of the z measurements of all tracks at their closest approach to the beam is less than 20 cm. There must be at least one TOF signal occurring within 10 ns of the expected value for a track originating from the interaction point. All events which have a pair of TOF signals separated by more than 165° in ϕ and have a time difference more than 10 ns are discarded. This ensures that back-to-back tracks are not created by the same cosmic ray particle.

Two Photon and Extreme Radiation Rejection

Two photon events and events with extreme radiation are removed by exploiting the fact that the tau pair jets are back-to-back or "collinear". These background events are rejected by requiring that the acollinearity of candidate tau events be less than 15° where the direction of the jets is given by the momentum sums of the tracks and clusters. An event is rejected if the visible energies of the jets (the maximum of the scalar sum of the momenta of the charged tracks plus the ECAL energy) is less than 3% of the center-of-mass energy (E_{CM}) or if the visible energies of the jets is less than $0.2E_{CM}$ and the missing transverse momentum of the event is less than 2 GeV/c.

Rejection of Multihadronic Events: $e^+e^- \rightarrow q\bar{q}$

The expected low charged track multiplicity of tau pair events is used to reject the multihadronic background $e^+e^- \rightarrow q\bar{q}$. The number of charged tracks in a candidate tau jet must be less than seven with no more than 10 ECAL energy clusters associated with a jet. The average charged particle multiplicity of a $e^+e^- \rightarrow q\bar{q}$ event at LEP is approximately 20.

Rejection of Electron Pair Events: $e^+e^- \rightarrow e^+e^-$

Electron pair events $e^+e^- \rightarrow e^+e^-$ leave a considerable fraction of the beam energy in the ECAL. Candidate tau events are rejected if the total ECAL cluster energy is greater than $0.8E_{CM}$ or if the total ECAL cluster energy plus 30% of the sum of the charged track energy is greater than the center-of-mass energy.

Rejection of Mu Pair events: $e^+e^- \rightarrow \mu^+\mu^-$

A candidate tau pair event is rejected if both jets satisfy a muon hypothesis and if the scalar sum of the charged track momenta plus the sum of the most energetic ECAL cluster in each jet is greater than $0.6E_{CM}$. The muon hypothesis requires at least one charged track in a jet and one of the three requirements a) more than one signal in the muon chambers associated with the highest momentum track in the jet, b) more than 3 signals in the HCAL with at least one in the outer three layers and the total number of HCAL signals in the jet divided by the number of layers hit less than two, and c) less than 2 GeV of ECAL energy associated with the track.

4.2 The Monte Carlo Data Set

Monte Carlo simulated data are used to estimate the efficiency and purity of the tau preselection as well as that of the $\tau^\pm \rightarrow \rho^\pm\nu_\tau$ selection. The $e^+e^- \rightarrow \tau^+\tau^-$ Monte Carlo is generated with the KORALZ [28] generator using versions 3.8 and 4.0. Version 3.8 (dataset MC1508) takes into account initial state bremsstrahlung to $\mathcal{O}(\alpha^2)$, final state bremsstrahlung and electroweak corrections to $\mathcal{O}(\alpha)$ as well as single bremsstrahlung in tau decays to leading log approximation. Version 4.0 (datasets MC1513, MC1515, and MC1516) encompasses all of the radiative corrections of version 3.8 but extends the final state bremsstrahlung correction to $\mathcal{O}(\alpha^2)$ and calculates the leptonic decay radiation to $\mathcal{O}(\alpha)$.

The multihadronic decay $e^+e^- \rightarrow q\bar{q}$ is simulated with the JETSET [29] Monte Carlo generator with tuned parameters based on OPAL multihadronic data [30]. Muon pair and

Non-tau background	Percent
$e^+e^- \to e^+e^-$	0.24 ± 0.07
$e^+e^- \to \mu^+\mu^-$	1.00 ± 0.28
$e^+e^- \to q\bar{q}$	0.42 ± 0.08
Two photon	0.17 ± 0.03
TOTAL	1.83 ± 0.30

Table 4.1: *Table of the non-tau contamination of the* $e^+e^- \to \tau^+\tau^-$ *preselection from [34].*

electron pair events are generated with the KORALZ and BABAMC [31] generators.

The response of the OPAL detector is simulated with the GOPAL [32] simulator program which is based on the GEANT [33] package. GOPAL simulation is applied to all Monte Carlo generated particles.

4.3 Estimation of Tau Preselection Efficiency

The application of the tau preselection given in this chapter to the tau pair as well as non-tau pair Monte Carlo events predicts a tau preselection efficiency of 93% within the fiducial acceptance of $|\cos\theta| \leq 0.68$. The composition of the estimated non-tau background totaling 1.8% is listed in table 4.1 [34].

169000 tau events are selected from the 1990-94 OPAL data sample measured near the Z^o pole of which 3% of the events are collected at a center-of-mass energy of 89.4 GeV, 93% of the events at 91.3 GeV, and 4% of the events at 93.0 GeV. 708000 Monte Carlo tau events generated in the same proportions at each of the three center-of-mass energies are used to compare with the data (MC1515 at 89.4 GeV, MC1508 and MC1513 at 91.3 GeV, and MC1516 at 93.0 GeV). The different tau decay channels of the Monte Carlo are reweighted to reflect the most up to date branching ratio measurements of each tau channel (see appendix A).

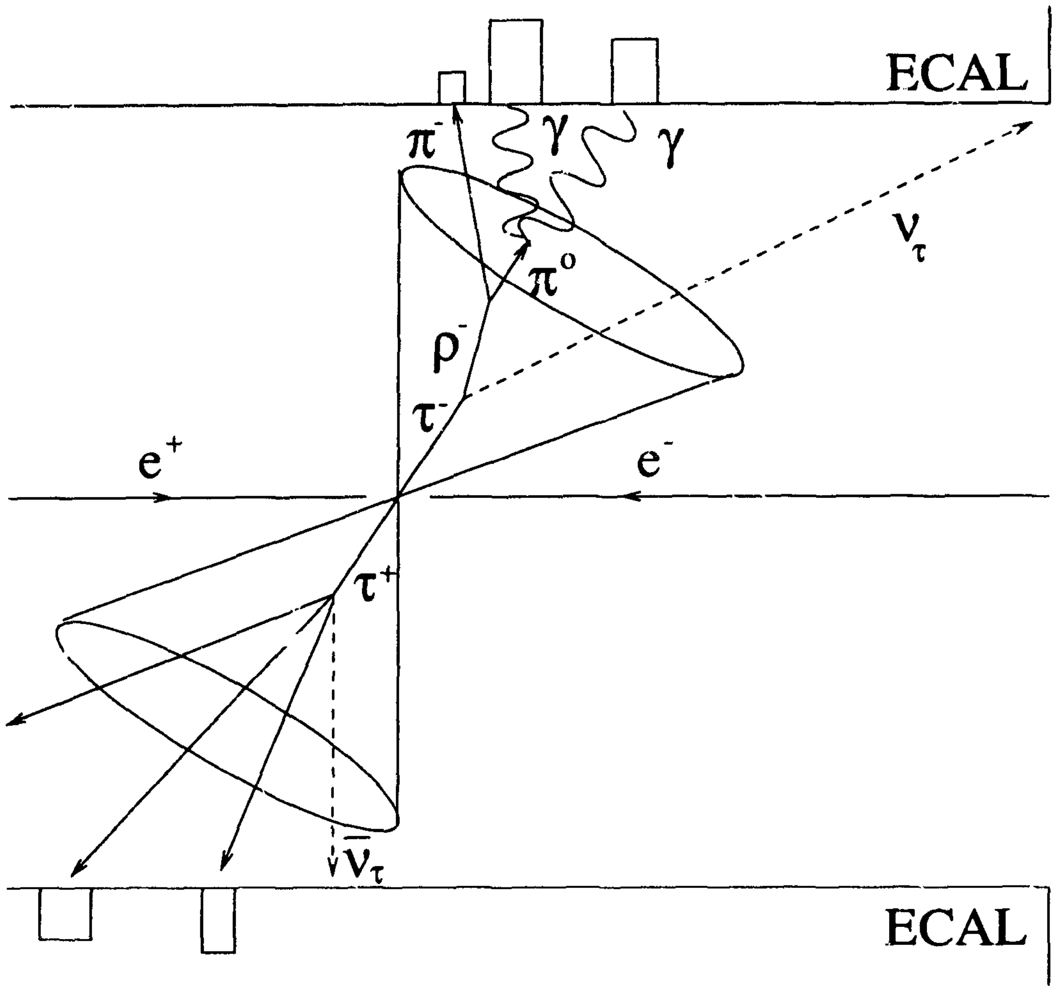

Figure 4.2: *A schematic of the decay* $e^+e^- \to \tau^+\tau^-$ *with the* $\tau^\pm \to \rho^\pm\nu_\tau$ *decay in one tau jet and a three-prong tau decay in the other jet.*

4.4 The Identification of $\tau^\pm \to \rho^\pm\nu_\tau$ Events

The tau lepton decays to the $\rho^\pm(770)$ with a branching ratio of approximately 25%. The ρ then immediately decays hadronically to a charged pion and neutral pion with the subsequent electromagnetic decay of the neutral pion to two photons. This decay chain is shown schematically in figure 4.2. The two photons interact in the electromagnetic calorimeter depositing all of their energy and creating clusters of energy. The charged pion on average deposits one third of its energy in the electromagnetic calorimeter but may deposit as much as 100% or as little as an undetectable amount.

An algorithm which identifies clusters of energy in the electromagnetic calorimeter is presented in this section. When possible, the tracks of the charged pions in the central tracking system are associated with the clusters of energy in the ECAL while the remaining clusters are candidate photons coming from the decay of the π^0. The ECAL cluster energies are corrected to account for the possible loss of energy by the photon before it reaches the ECAL. The momentum and energy resolutions of the Monte Carlo data are adjusted to match the resolutions of the OPAL data. When possible, the corrected energy of the candidate photons are used to reconstruct the π^0. The $\rho^{\pm}(770)$ is reconstructed with ECAL information generated by the π^0 and the central tracking information produced by the charged pion.

Electromagnetic Clustering Algorithm

The kinematics of the decay to two bodies indicate that the minimum opening angle in the laboratory frame of two photons coming from the decay of the π^0 is

$$\theta^{\pi^o}_{open} = 2\tan^{-1}\left(\frac{m_{\pi^o}}{p_{\pi^o}}\right)$$

as shown in figure 4.3a. The mass of the π^0, m_{π^o}, is 135 MeV/c^2 and p_{π^o} is the momentum of the π^0. The decay of the $\rho^{\pm}$ to a charged pion and neutral pion has no minimum opening angle in the laboratory frame because the decay products of the $\rho^{\pm}$ are massive. However, the majority of the $\rho^{\pm} \longrightarrow \pi^{\pm}\pi^o$ events do have an effective minimum opening angle of

$$\theta^{\rho}_{open} \approx 2\tan^{-1}\left(\frac{m_{\rho}\sqrt{1 - 4m_{\pi}^2/m_{\rho}^2}}{p_{\rho}}\right)$$

shown in figure 4.3b. The mass of the ρ, m_{ρ} is 770 MeV/c^2. The mass of the charged and neutral pions are approximately the same, m_{π}=135 MeV/c^2, and p_{ρ} is the momentum of the ρ. Most of the charged and neutral pions are always separated by at least 30 mrad. However, the photons will be less than half an EB block apart if the π^0 energy exceeds approximately 15 GeV thereby overlapping the showers and making the two photon separation difficult or impossible. A clustering algorithm had been devised [35] to optimize

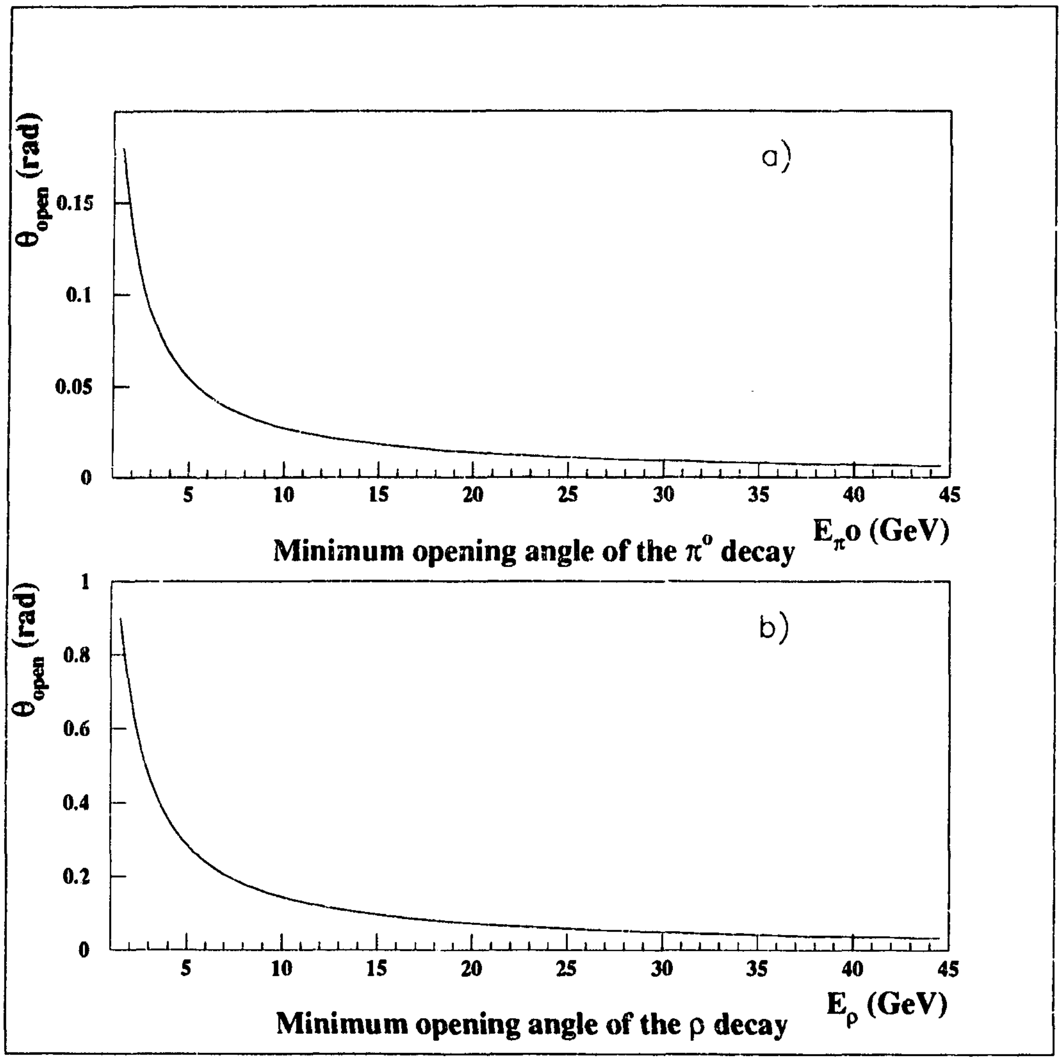

Figure 4.3: *The minimum laboratory frame opening angle as a function of energy of a) the decay of the neutral pion to two photons and b) the majority of the decays of the ρ to a charged pion and neutral pion.*

the identification of photons in the ECAL coming from the decay of the π^0. Electron electromagnetic showers in the lead glass leave on average 94% of their energy in two EB blocks while pion showers leave 96% of their deposited energy in four blocks. The clustering algorithm limits the size of ECAL clusters to a 2×2 grid (2 blocks in $\theta \times 2$ blocks in ϕ).

The clustering algorithm is applied to the ECAL for all events which meet the tau preselection criteria. The centroid of each cluster $(\langle\theta\rangle_{cl}, \langle\phi\rangle_{cl})$ is determined through a weighted average over the n blocks in the cluster

$$\langle\theta\rangle_{cl} = \frac{\sum_{i=1}^{n} \theta_i W_i}{\sum_{j=1}^{n} W_j} \qquad \langle\phi\rangle_{cl} = \frac{\sum_{i=1}^{n} \phi_i W_i}{\sum_{j=1}^{n} W_j}$$

where θ_i and ϕ_i are the center coordinates of block i in the cluster and $W_{i,j} = E_{i,j}^{\frac{1}{3}}$ is the weighted energy in each block.

Track-cluster Association

All clusters found in the ECAL are classified as either hadronic clusters associated with the charged pions or electromagnetic, neutral clusters associated with the photons coming from the decay of the π^0. Hadronic clusters are identified by matching position information from the central tracker to the calculated position of clusters in the ECAL. A $\tau^\pm \to \rho^\pm \nu_\tau$ produces one charged track in the central tracker or possibly two or three tracks if one of the photons from the π^0 decay converts in the material of the detector to an electron-positron pair. For this reason the $\tau^\pm \to \rho^\pm \nu_\tau$ selection requires only one charged track or less than four charged tracks if the extra tracks are consistent with coming from a displaced vertex identifying them as a conversion. The charged track of the candidate $\pi^\pm$ is matched to all clusters in the ECAL through a χ^2 criterion

$$\chi_\theta^2 = \frac{(\theta_{tk} - \langle\theta\rangle_{cl})^2}{\sigma_\theta^2} \qquad \chi_\phi^2 = \frac{(\phi_{tk} - \langle\phi\rangle_{cl})^2}{\sigma_\phi^2} \tag{4.1}$$

where θ_{tk} and ϕ_{tk} are the measured θ and ϕ coordinates of the charged particle at the entrance to the ECAL based on central tracking information. The denominators of the two χ^2 are determined by a special study made in this thesis of the tau decay to a single hadron.

Tracks with no CZ Information		
Data Set	σ_θ (mrad)	σ_ϕ (mrad)
1990-92	24.6	9.5
1993	29.6	10.4
1994	29.7	8.3
MC1508	26.0	8.9
MC1513	24.5	8.9
Tracks with CZ Information		
Data Set	σ_θ (mrad)	σ_ϕ (mrad)
1990-92	8.9	8.9
1993	8.9	8.8
1994	8.9	9.0
MC1508	8.7	9.2
MC1513	8.7	9.1

Table 4.2: *Table of widths of the Gaussian fit to the distributions $\theta_{tk} - \langle\theta\rangle_{cl}$ and $\phi_{tk} - \langle\phi\rangle_{cl}$ of $\tau^\pm \rightarrow \pi^\pm\nu_\tau$ events for the different years of data taking and Monte Carlo detector configuration.*

The clustering algorithm is applied to a $\tau^\pm \rightarrow \pi^\pm\nu_\tau$ selection. The difference between the tracking information and the cluster centroid information is shown in figure 4.4 for pion events where only one ECAL cluster is found by the clustering algorithm. These distributions are fit to Gaussian distributions to extract their widths for the different years of data taking and Monte Carlo detector configurations shown in table 4.2. These widths are the σ_θ and σ_ϕ used in the χ^2 criterion of equation 4.1. Both χ^2_θ and χ^2_ϕ must be less than 8 for an ECAL cluster to be associated with a track. If several ECAL clusters satisfy this criterion, then the cluster with the smallest χ^2 is taken to be the hadronic cluster. All remaining ECAL clusters are candidate neutral clusters from the decay of the π^0 to two photons. Approximately 70% of all $\tau^\pm \rightarrow \rho^\pm\nu_\tau$ events satisfy this track association criterion. Half of the remaining events fail the association mostly because a photon located near the charged pion is skewing the centroid of the hadronic cluster. The remaining hadronic events fail to leave enough energy in the ECAL to form a cluster.

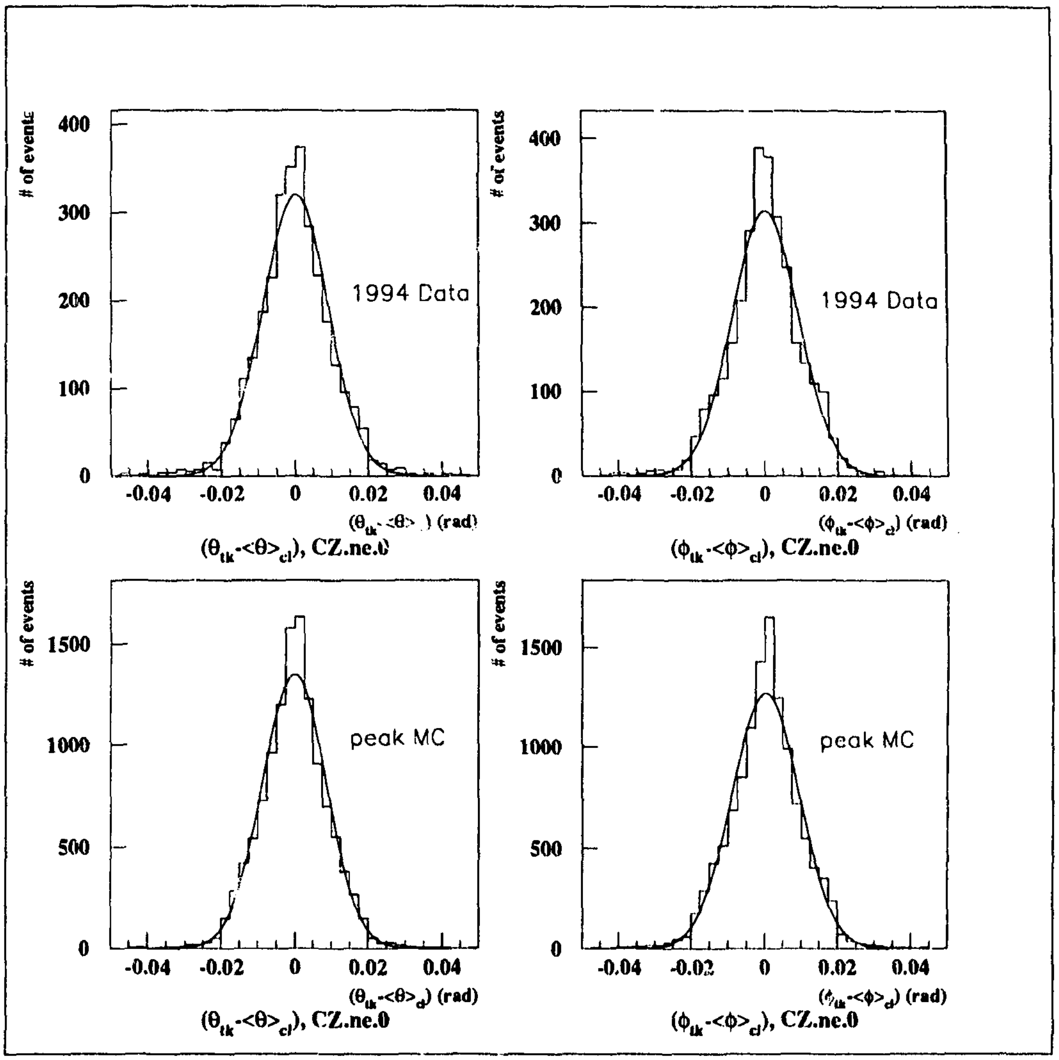

Figure 4.4: *This figure shows the difference between the tracking information and the cluster centroid information in θ and ϕ (top two plots) for pions which have z information from the CZ chambers from the 1994 data set and some pion events from the on peak Monte Carlo (bottom two plots).*

Photon Energy Measurement Correction

Some photons begin producing an electromagnetic shower in the coil located in front of the ECAL and hence lose some of their energy before reaching the ECAL. The ECAL energy clusters of these photons must be corrected for this energy loss. The barrel presampler, PB, is used to determine if the showering occurs before the ECAL. It is assumed that a shower in the coil has occurred if there is activity in PB within 120 mrad of an ECAL neutral cluster centroid.

A study has been made by the OPAL collaborators responsible for the electromagnetic calorimeter [36] to determine a corrected energy, E_c, for the raw ECAL energy, E_{raw}, if an electron showers in the coil. A separate study is made in this thesis to establish a correction factor, a_γ, for the corrected energy, E_c, when photons instead of electrons shower in the coil. This separate study is based purely on Monte Carlo events and compares "generator level quantities" (kinematic quantities before detector effects are applied, also referred to as "four-vector quantities") with raw ECAL cluster energies. A sample of isolated photons is identified in $\tau^\pm \rightarrow \rho^\pm \nu_\tau$ Monte Carlo events by requiring that

- the four-vector angle between the charged pion and the candidate isolated photon be greater than 100 mrad
- the four-vector angle between the candidate isolated photon and the other π^0 photon be greater than 100 mrad.

Figure 4.5a shows the difference, $(E_{4v} - E_{raw})/E_{raw}$, between the four-vector energy of the isolated photon, E_{4v}, and the uncorrected energy it deposits in the ECAL, E_{raw}, when some PB activity is associated with this isolated photon. A Gaussian fit to this distribution shows a mean shifted from zero and that the data is from an asymmetric distribution. Replacing the raw energy by the corrected energy, E_c, yields a more symmetric distribution (figure 4.5b) but a mean still displaced from zero. The shift of the mean is reduced if the corrected energy is scaled down by a factor $a_\gamma = 0.91$. Figure 4.5c shows a Gaussian fit to the distribution $(E_{4v} - .91E_c)/E_c$. The corrected energy, E_c, although appropriate for electrons showering in the coil, requires a scale factor of $a_\gamma = 0.91$ to be appropriate

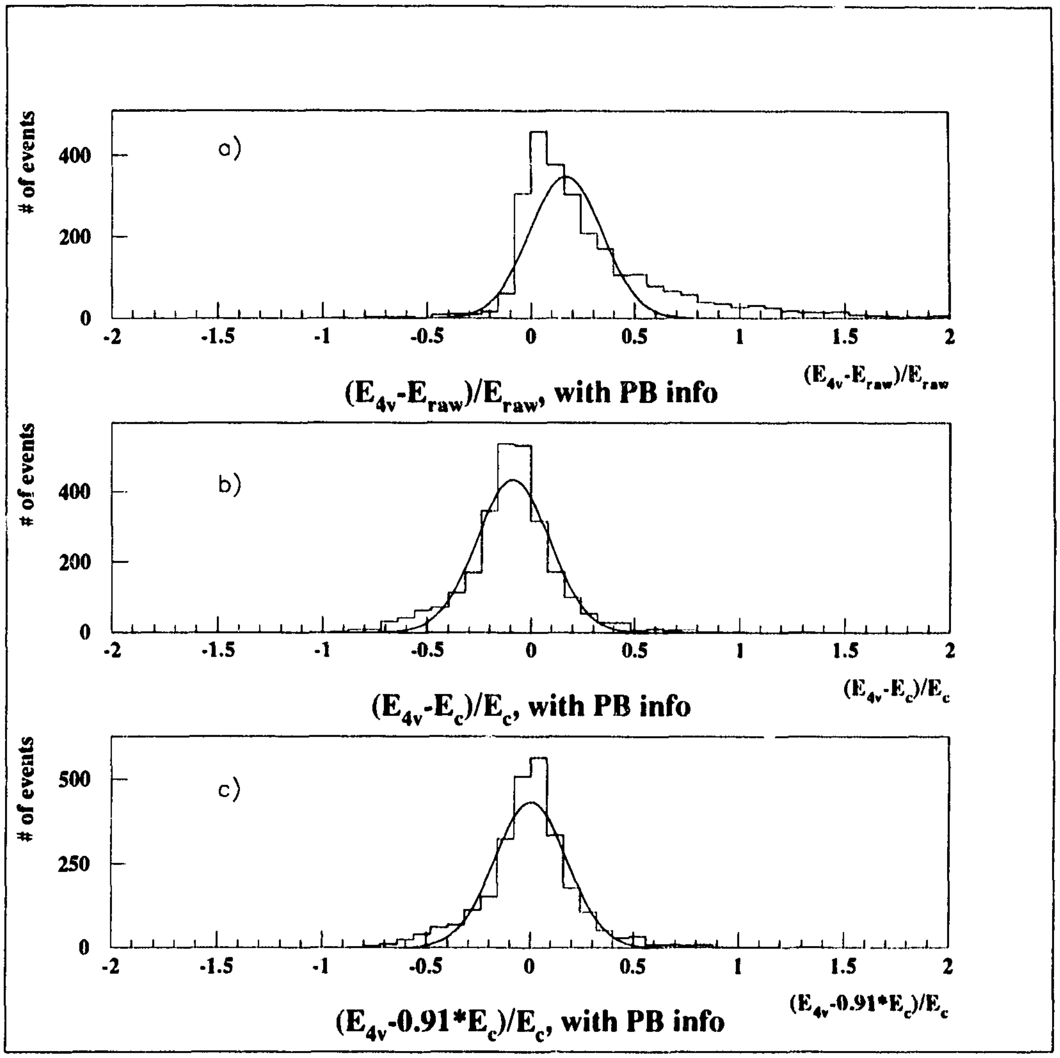

Figure 4.5: *Figure of the isolated photon study comparing generator level energies with ECAL cluster energies which have PB activity associated with them. a)* $(E_{4v} - E_{raw})/E_{raw}$ *b)* $(E_{4v} - E_c)/E_c$ *c)* $(E_{4v} - .91E_c)/E_c$.

<table>
<tr><th colspan="4">PB information available</th></tr>
<tr><th>Number of neutral clusters</th><th>PB information</th><th>Percent of events</th><th>Corrected neutral cluster energy</th></tr>
<tr><td>2</td><td>No PB hits for either cluster</td><td>10</td><td>$E_1 = E_{raw1}$ $E_2 = E_{raw2}$</td></tr>
<tr><td></td><td>PB hits for one cluster</td><td>48</td><td>$E_1 = 0.91E_{c1}$ $E_2 = E_{raw2}$</td></tr>
<tr><td></td><td>PB hits for both clusters</td><td>42</td><td>$E_1 = 0.91E_{c1}$ $E_2 = 0.91E_{c2}$</td></tr>
<tr><td>1</td><td>No PB hits</td><td>9</td><td>$E_1 = E_{raw1}$</td></tr>
<tr><td></td><td>PB hits</td><td>91</td><td>$E_1 = E_{c1}$</td></tr>
<tr><th colspan="4">No PB information available</th></tr>
<tr><td>2</td><td></td><td></td><td>$E_{1,2} = 0.34E_{raw} + 0.66 * 0.91E_c$</td></tr>
<tr><td>1</td><td></td><td></td><td>$E_1 = 0.09E_{raw1} + 0.91E_{c1}$</td></tr>
</table>

Table 4.3: *Table of the energy correction scheme for two neutral clusters with raw energies, E_{raw1} and E_{raw2}, and corrected energies, E_{c1} and E_{c2}, or one neutral cluster with raw energy, E_{raw1}, and corrected energy, E_{c1}, with and without PB information being available.*

for photons showering in the coil. This is likely due to the electrons beginning to shower earlier on average in the coil than the photons.

The topologies of the decay of the π^0 to two photons must be understood before the scale factor a_γ found from the isolated photon shower study can be applied to all photons of the π^0 decay. Figure 4.3a shows that the two photons may appear as well separated clusters in the ECAL or they may overlap producing only one cluster in the ECAL. Table 4.3 shows the breakdown of these topologies based on whether or not there is PB activity associated with the neutral cluster and gives the corrected energy for the neutral cluster. This study has shown that two overlapping photon showers interact in the coil in a similar way as an electron in the coil so the full corrected energy, E_c, is applied when there is only one neutral cluster with PB activity associated with it. An estimate of the energy correction is made when the barrel presampler is not functioning based on the probability of PB information when it was functioning. Table 4.3 shows that when PB information is available and two neutral clusters are found then (10 +48/2)% = 34% of the time one of the two neutral clusters will not interact in the coil while (48/2+42)% = 66%

of the time a neutral cluster will interact in the coil. Hence, when two neutral clusters are found but PB information is not available, the energy of each cluster is corrected to be $E = 0.34E_{raw} + 0.66 * (0.91E_c)$. Similarly, when only one neutral cluster is found and no PB information is available, the neutral cluster energy is corrected to be $E = 0.09E_{raw} + 0.91E_c$. Figure 4.6 shows the improvement in the reconstructed mass of the π^0 when using the energy correction scheme.

A further correction of the ECAL energy is made. The energy from the electromagnetic calorimeter is corrected to agree with a $\tau \rightarrow e\nu\bar{\nu}$ sample by forcing the ECAL energy associated with the electron divided by its momentum (E/p) of the Monte Carlo data to match that of the data as a function of energy. This correction factor modifies the Monte Carlo energy to be:

$$\begin{gathered} 0.978 \times E \text{ for } E < 3\,\text{GeV} \\ 0.993 \times E \text{ for } (3 < E < 21)\,\text{GeV}. \end{gathered} \tag{4.2}$$

where E is the corrected energy. There is a 0.28 percent statistical error associated with this energy correction

Tracking and ECAL Resolutions

The Monte Carlo track momentum and ECAL energy resolutions are generated to be better than those of the data so that any later recalibration of the data does not result in resolutions better than that of the Monte Carlo. Therefore, an ad-hoc correction must be made to adjust or smear the Monte Carlo resolutions to match those of the data.

The tau working group at OPAL has calculated extra smearing factors for the Monte Carlo track momentum. These are determined by comparing the generated (gen) and measured ($meas$) values of x_t, the transverse momentum of the track divided by the beam energy, for $e^+e^- \rightarrow \mu^+\mu^-$ events [37]. A scaling factor is determined from the $1/x_t^{gen} - 1/x_t^{meas}$ distribution when $x_t^{gen} - x_t^{meas} > 0$ and the $x_t^{gen} - x_t^{meas}$ distribution when $x_t^{gen} - x_t^{meas} < 0$. These scaling factors are determined for the different years of data taking and different Monte Carlo detector configurations. The magnitude of the scaling

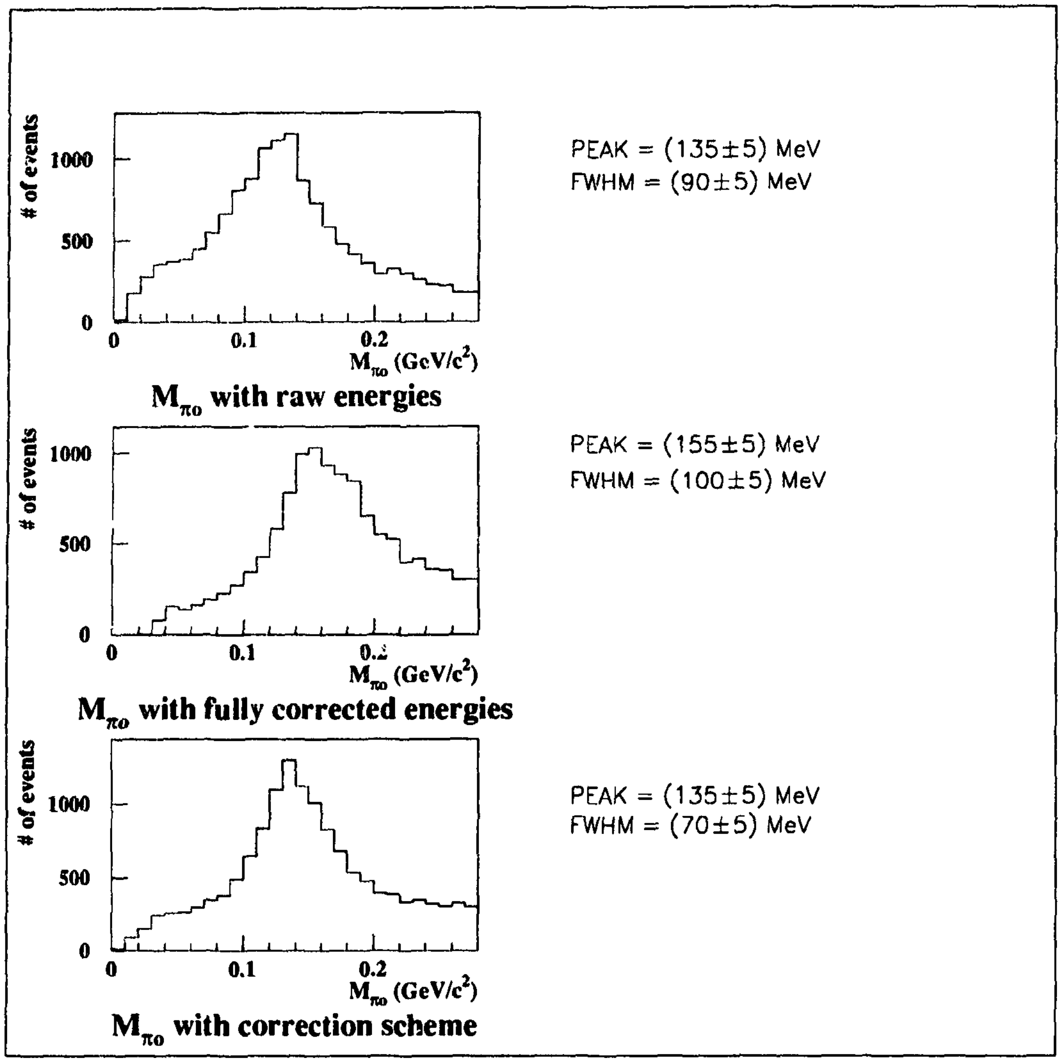

Figure 4.6: *Figure of the reconstructed mass of the* π^0 *from* $\tau^{\pm} \rightarrow \rho^{\pm}\nu_{\tau}$ *decay when a) only raw energies* (E_{raw}) *are used, b) only corrected energies* (E_c) *are used, and c) the energy correction scheme of table 4.3 is used.*

factor is momentum dependent but a typical scaling factor for the difference between generated and measured resolutions is 1.40 ± 0.05.

A separate study [38] is made in this thesis to determine the ECAL energy smearing terms specific to the clustering algorithm used in this work. The barrel electromagnetic calorimeter energy resolution is extracted from a $\tau^{\pm} \rightarrow e^{\pm}\nu\nu$ sample with the energies of the electromagnetic showers in the ECAL ranging from 0.1 GeV up to 45 GeV. This is accomplished by comparing the difference between the ECAL cluster energy associated with the electron and its momentum $(E - p)$. The energy resolution is extracted by subtracting in quadrature the momentum resolution from the $(E - p)$ resolution. The momentum resolution of the jet chamber is measured from the momentum distribution of muons pairs from a $e^+e^- \rightarrow \mu^+\mu^-$ sample. The availability of the z-coordinate of tracks from the z-chambers is taken into account in this study.

The momentum resolution of the data is extracted from the width of the distribution

$$\left(\frac{1}{p}\right)_{\mu^+} - \left(\frac{1}{p}\right)_{\mu^-} \tag{4.3}$$

where p_{μ^+} and p_{μ^-} are the momenta of the positively charged and negatively charged muons respectively. The distributions for the 1993 data are shown in figure 4.7a for tracks with no z-chamber information (CZ = 0) which applies to approximately 13 percent of the data and figure 4.7b for tracks with z-chamber information (CZ > 0) and are compared to the equivalent distributions coming from the $e^+e^- \rightarrow \mu^+\mu^-$ Monte Carlo in figures 4.7c and 4.7d. The momentum resolution is taken as the standard deviation of a Gaussian fit to the distributions. In figures 4.7a and 4.7c, the non-Gaussian tails for events with no z-chamber information are evident. These tails are ignored when extracting the momentum resolution. The momentum resolutions, σ_p, are extracted as a function of data taking years and for the $e^+e^- \rightarrow \mu^+\mu^-$ Monte Carlo sample. An additional term which estimates the multiple scattering term, σ_{MS}, dominant at lower momenta, is included in the momentum resolutions

$$(\sigma_p)^2_{tot} = (\sigma_p)^2 + (\sigma_{MS})^2, \qquad \text{where} \qquad \sigma_{MS} = 1.0 \times 10^{-3}\text{GeV/c}. \tag{4.4}$$

An iterative Gaussian fit is performed to the difference between the ECAL cluster

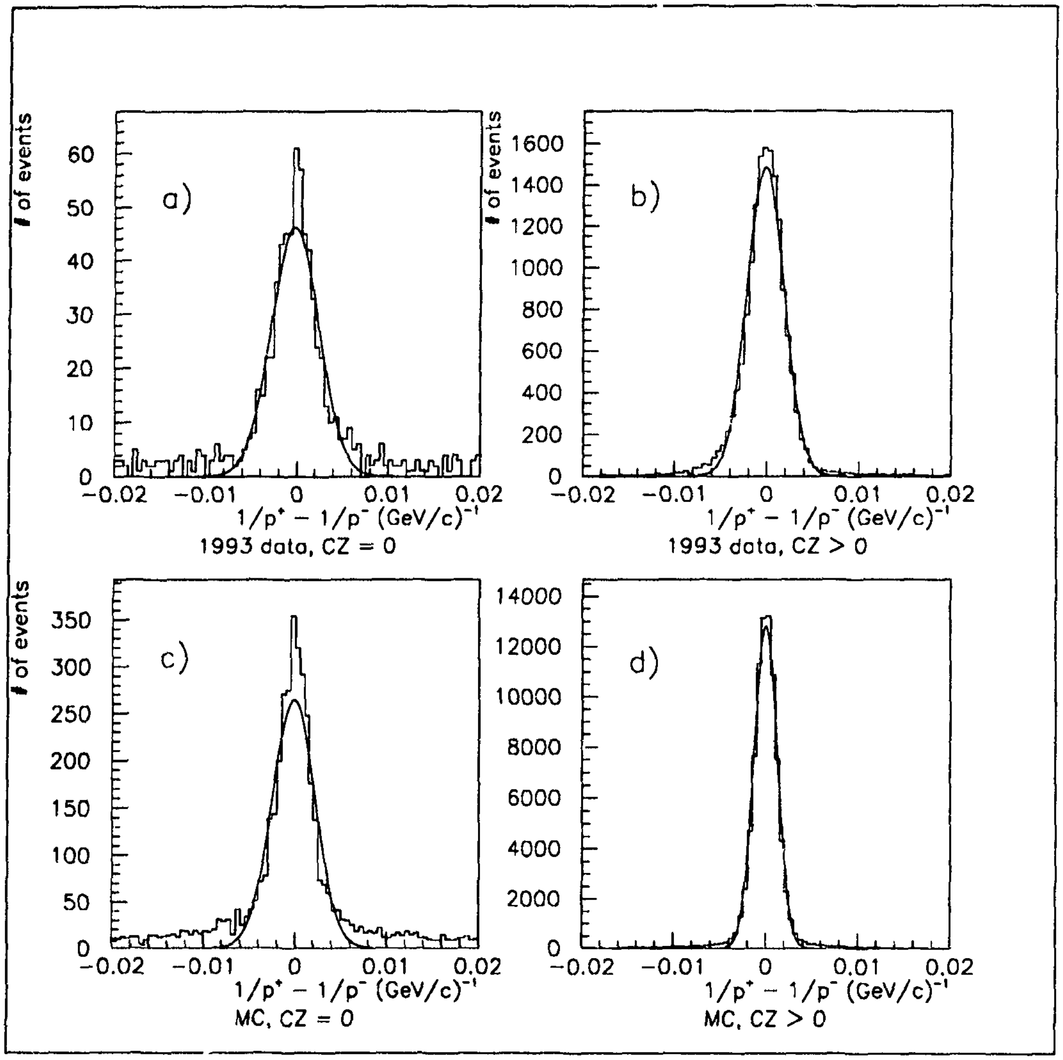

Figure 4.7: *The distribution* $\left(\frac{1}{p}\right)_{\mu^+} - \left(\frac{1}{p}\right)_{\mu^-}$ *for a) the 1993 data with no CZ information (CZ=0), b) the 1993 data with CZ information (CZ>0), c) the Monte Carlo with CZ=0, and d) the Monte Carlo with CZ>0 extracted from* $e^+e^- \to \mu^+\mu^-$ *events. The standard deviations of these distributions are* $\sqrt{2} \times \sigma_p/p^2$.

energy and the momentum ($E - p$) of $\tau^{\pm} \to e^{\pm}\nu_{\tau}\nu_{e}$ events in seven separate momentum bins measuring the ($E - p$) resolution, σ_{E-p}. Figure 4.8 shows the $E - p$ distributions for each momentum bin for the 1993 data. The quantity $E - p$ is not Gaussian but can be reasonably well approximated as such. The $E - p$ distributions are fit to a Gaussian using an iterative Gaussian fit to reduce the effects of the non-Gaussian tails. The resulting width and mean of the first Gaussian fit are used to make a second Gaussian fit of the data within ±3 standard deviations of the mean of the first fit. The calculated momentum resolution of equation 4.4 is subtracted quadratically from $\sigma(E - p)$ to isolate the energy resolution in each momentum bin

$$\sigma(E) = \sqrt{\sigma(E - p)^2 - \sigma(p)^2}. \tag{4.5}$$

Figure 4.9a shows the plot of $\sigma(E)/E$ vs. $1/\sqrt{E}$ for the 1993 data where E is given by the midpoint of each momentum bin plus any shift in the mean of the Gaussian fit to the $E - p$ peak to correct the calibration. Figure 4.9b shows the equivalent plot using the $\tau^{\pm} \to e^{\pm}\nu_{\tau}\nu_{e}$ events from Monte Carlo run 1513. Both plots in figure 4.9 show the expected form for the resolution of the ECAL: $A + B/\sqrt{E}$. The energy resolutions for all data taking years are consistent within the errors so all the data years are combined to give a global ECAL energy resolution for the data of

$$\sigma(E)/E = (1.1 \pm .3)\% + (18.8 \pm 1.1)\%/\sqrt{E} \tag{4.6}$$

where the energy is given in GeV. The Monte Carlo ECAL energy resolution is

$$\sigma(E)/E = (.1 \pm .1)\% + (17.0 \pm .4)\%/\sqrt{E}. \tag{4.7}$$

These results show that the Monte Carlo energies need very little additional smearing to match the energy resolution extracted from the data. The quadratic difference between these two resolutions is used as the additional smearing factor for the Monte Carlo ECAL energies.

The ρ selection

The information given in the last four sections is used to process both the data and the Monte Carlo before a ρ selection can be made. The ECAL clustering algorithm described

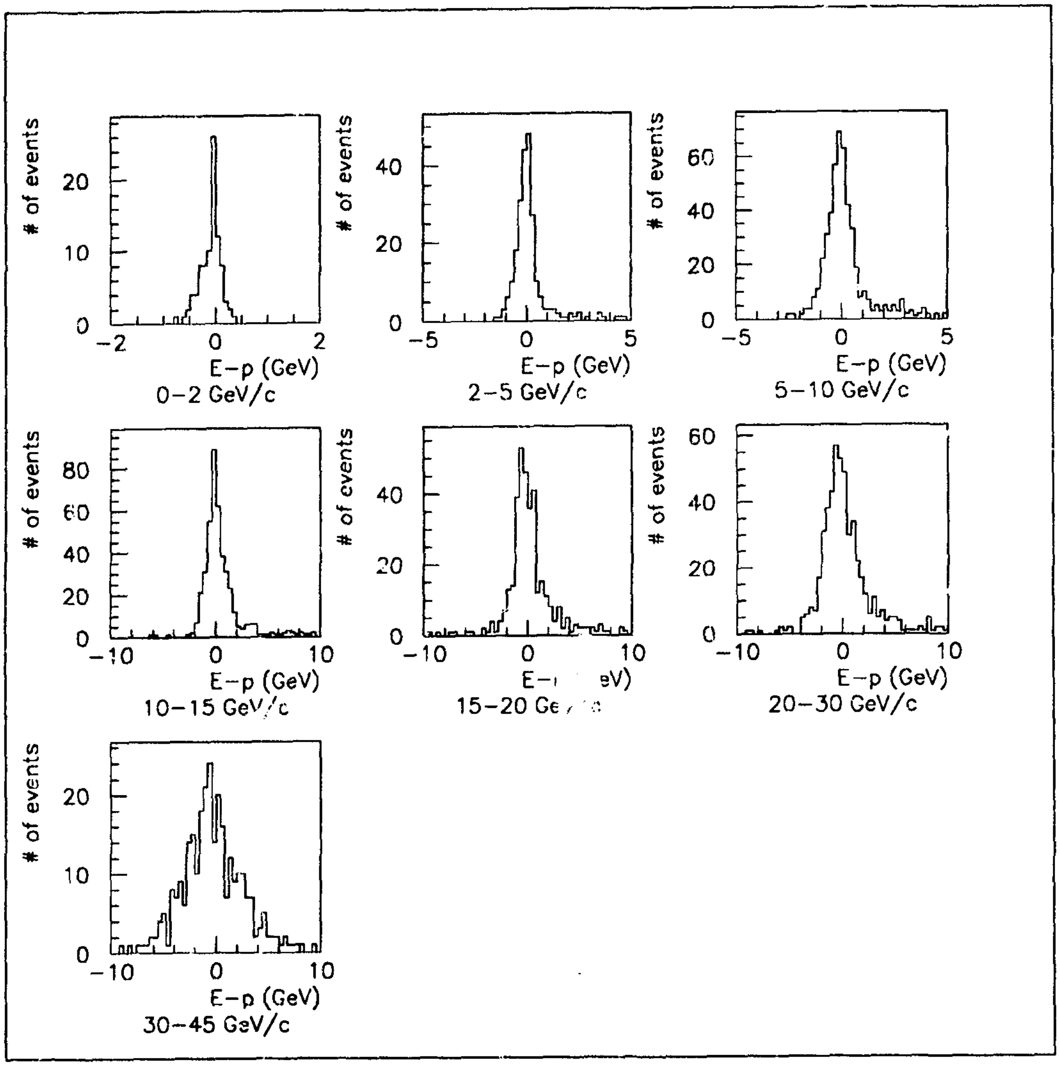

Figure 4.8: *The $E-p$ distributions of electrons coming from the 1993 $\tau^{\pm} \rightarrow e^{\pm}\nu_{\tau}\nu_{e}$ data sample for different momentum bins.*

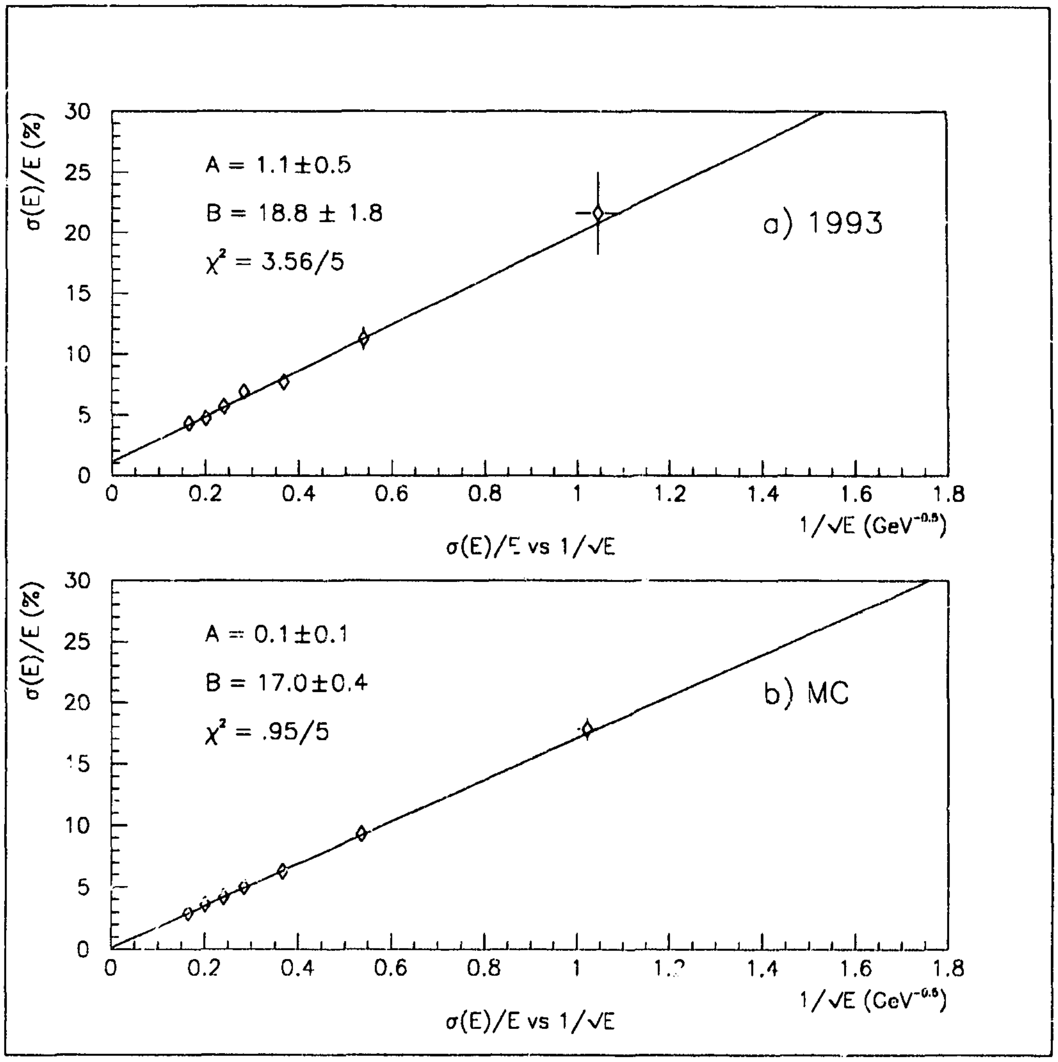

Figure 4.9: *The energy resolution, $\sigma(E)/E$, of the barrel ECAL extracted from a) the 1993 data and b) the Monte Carlo. Both plots show the expected $A + B/\sqrt{E}$ dependence.*

in a previous section is applied to all events satisfying the tau preselection. The track-cluster association is used to classify ECAL clusters as hadronic clusters, if they satisfy the association criterion, or as a neutral cluster coming from the decay of the π^0 to two photons. The energy correction scheme of table 4.3 is used to correct all neutral cluster energies and the tracking and energy resolutions of the Monte Carlo data are adjusted to match those of the OPAL data.

Up to three charged tracks are accepted if the extra tracks are consistent with being a conversion of a photon to an electron-positron pair. Any ECAL clusters associated with the tracks from a conversion are not classified as neutral clusters. The energies of the extra tracks coming from the conversions are used to determine the energy of the photons that converted. The converted photons then become candidate photons coming from the decay of the π^0 and are considered as "neutral clusters" in the discussion that follows.

The following selection criteria are used to enhance the $\tau^{\pm} \rightarrow \rho^{\pm}\nu_{\tau}$ signal.

- The ECAL energy associated with the $\pi^{\pm}$ track divided by its momentum (E/p) must be less than 0.9 to minimize electron contamination which peaks at E/p = 1.

- If only one neutral cluster is found, then it must have a minimum energy of 1 GeV. This requirement reduces the background coming from the decay of a tau to a pion where either the pion shower is large enough in the ECAL that the clustering algorithm reconstructs several clusters which are associated with the charged pion (known as hadronic splatter) or a photon was radiated during the process and produced a cluster in the ECAL. The one neutral cluster becomes a candidate π^0. Figure 4.10a shows the energy distribution of π^o's for this topology.

- If two neutral clusters are found, then the energy of each cluster must be at least 400 MeV and the reconstructed mass of the two clusters has to be consistent with the mass of the π^o (the reconstructed mass has to be less than 0.28 GeV/c^2) to become the candidate π^o. Figure 4.10b shows the sum of the energies of the two clusters and figure 4.11a shows the reconstructed mass of the two neutral clusters calculated with the relation

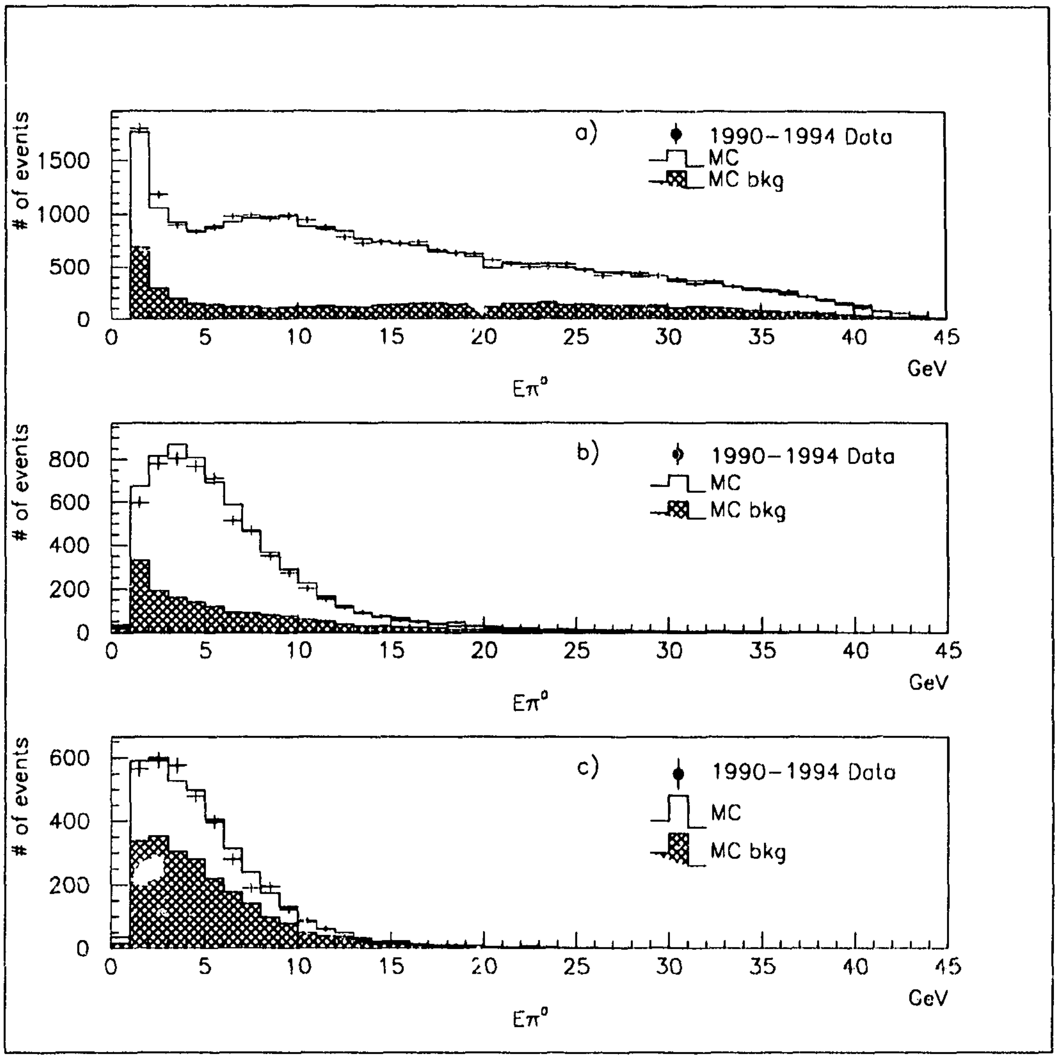

Figure 4.10: *This figure shows the energy of the candidate π^0's when a) only one neutral cluster is found, b) two neutral clusters are found, and c) more than two neutral clusters are found. The points represent the 1990-94 OPAL data. The histogram gives the Monte Carlo estimation of the energy of the candidate π^0 while the hatched histogram shows the energy distribution of the background events in the Monte Carlo $\tau^\pm \to \rho^\pm \nu_\tau$ sample.*

$$M_{\pi^0} = \Big([E_1 + E_2]^2 - [(E_1 \sin\theta_1 \cos\phi_1 + E_2 \sin\theta_2 \cos\phi_2)^2 +$$

$$(E_1 \sin\theta_1 \sin\phi_1 + E_2 \sin\theta_2 \sin\phi_2)^2 + (E_1 \cos\theta_1 + E_2 \cos\theta_2)^2]\Big)^{\frac{1}{2}} \qquad (4.8)$$

where E_1, θ_1, ϕ_1 and E_2, θ_2, ϕ_2 are the ECAL energy, θ and ϕ coordinates of the two neutral clusters. If a candidate π^0 satisfies the mass criterion, its momentum is adjusted such that the π^0 has its nominal mass of 135 MeV/c^2.

- An allowance is made for the possibility of a $\tau^\pm \to \rho^\pm \nu_\tau$ decay with more than two neutral clusters due to hadronic splattering or radiative photons produced in the decay. If more than two neutral clusters are found, then the three highest energy clusters are considered. All must have a minimum energy of 400 MeV. The reconstructed mass of each pair of clusters is calculated and the pair with the mass closest to the mass of the π^o becomes the candidate π^o if its reconstructed mass is less than 0.28 GeV/c^2. Figure 4.10c shows the sum of the energies of the two clusters and figure 4.11b shows the reconstructed mass of the two clusters.

- Tracking information from the candidate charged pion is used with ECAL information from the candidate neutral pion to reconstruct the ρ resonance. The mass of the ρ can be reconstructed through the relation

$$M_\rho = \sqrt{(m^2_{\pi^\pm} + m^2_{\pi^o}) + 2(E_{\pi^\pm} E_{\pi^o} - p_{\pi^\pm} p_{\pi^o} \cos\alpha)} \qquad (4.9)$$

where $m_{\pi^\pm}, E_{\pi^\pm}, p_{\pi^\pm}$ and $m_{\pi^o}, E_{\pi^o}, p_{\pi^o}$ are the mass, energy, and momentum of the charged pion and neutral pion respectively and α is the opening angle between the charged pion and neutral pion in the laboratory frame. A candidate ρ event must lie within the mass range $0.6 \leq M_\rho \leq 2.0$ GeV/c^2 to finally be accepted as a ρ event. The resulting M_ρ distribution before applying the mass requirement is shown in figure 4.12. The mass of the $\rho^\pm$(770) resonance is 769.9 ± 0.08 MeV/c^2 and has a full width of 151.2 ± 1.2 MeV/c^2 [3]. However, the reconstruction of the $\rho^\pm$ increases the full width to approximately 250 MeV/c^2.

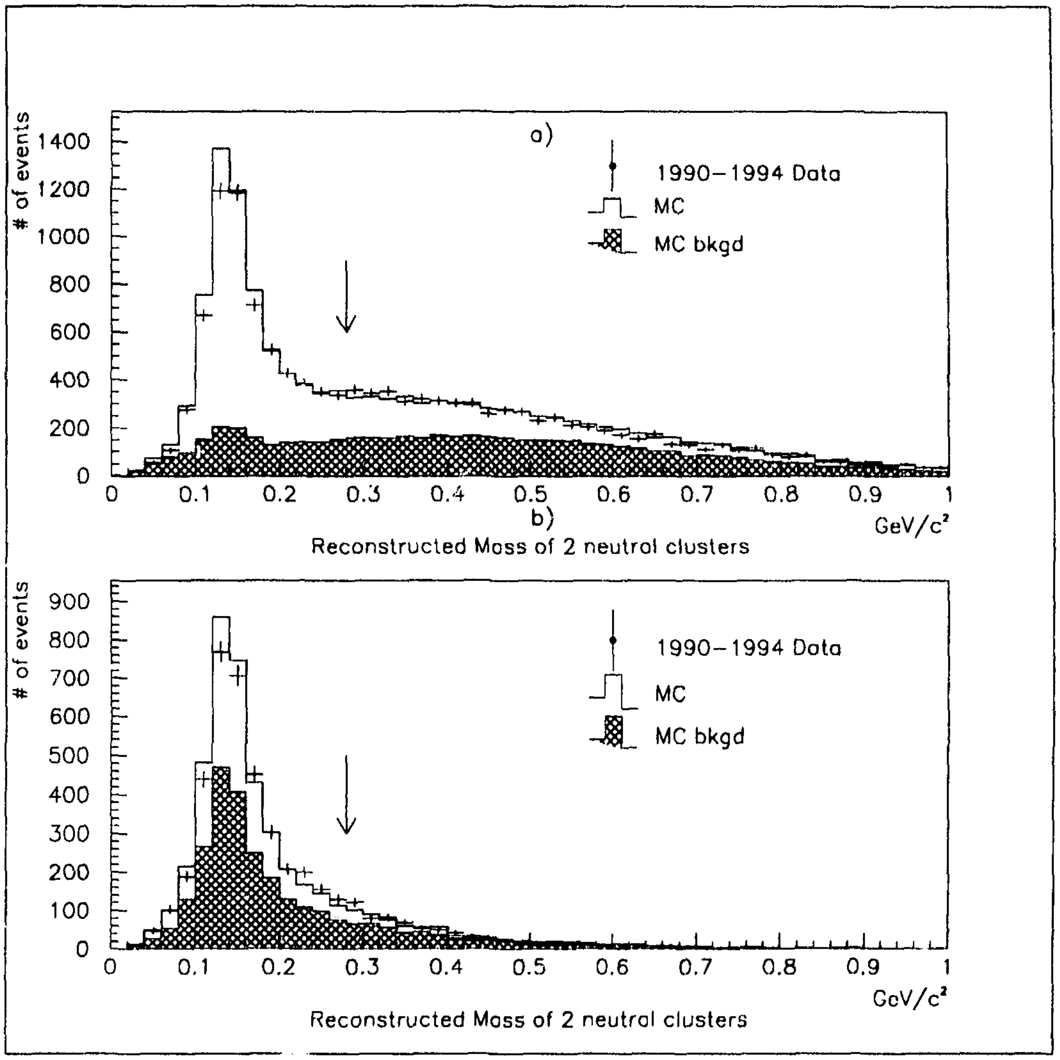

Figure 4.11: *This figure shows the reconstructed mass of candidate π^0's when a) two neutral clusters are found and b) more than two neutral clusters are found.*

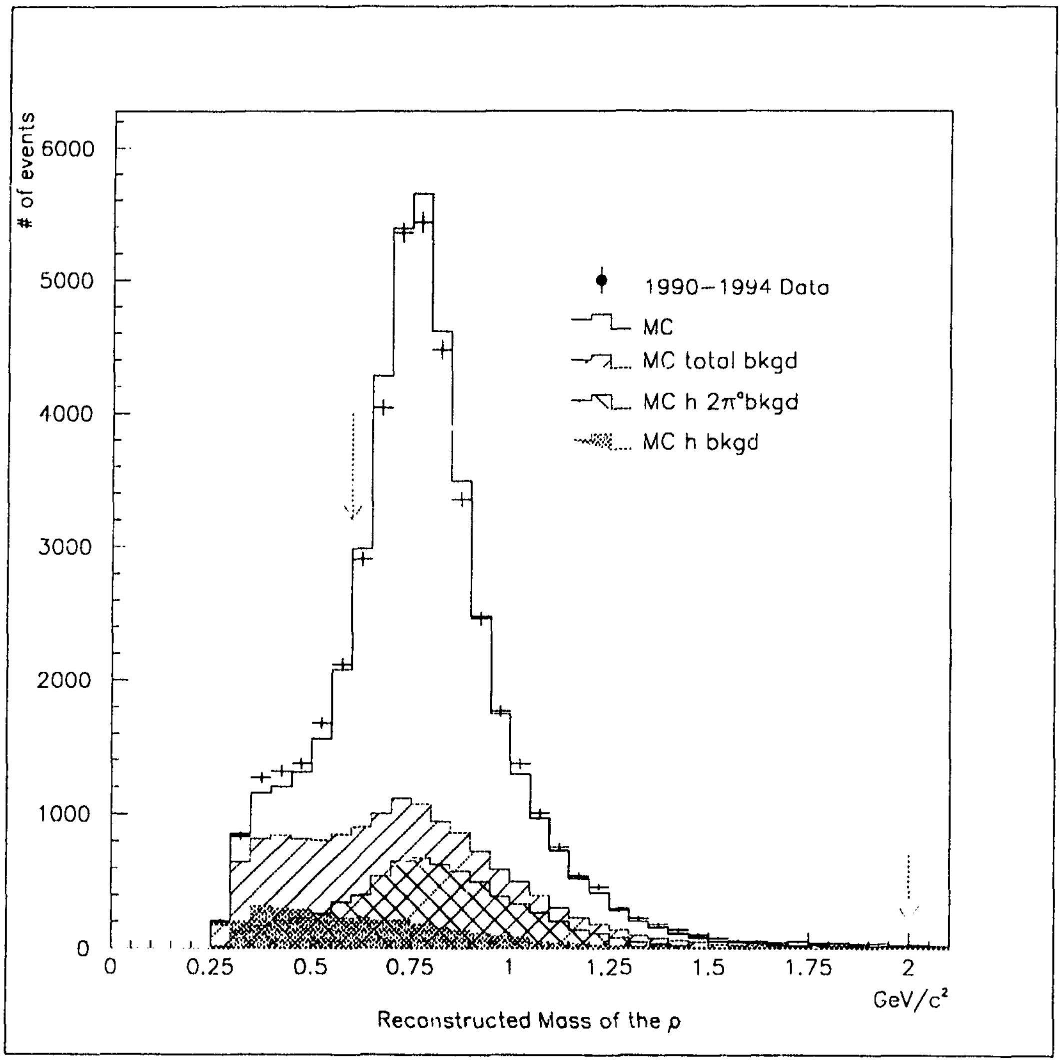

Figure 4.12: *This figure shows the reconstructed mass of the ρ candidates. The arrows indicate the placement of the ρ mass cuts.*

Background channel	Background (percent)
$\tau \to h2\pi^o\nu$	15.90
$\tau \to h\nu$	4.90
$\tau \to h3\pi^o\nu$	2.30
$\tau \to K^*\nu$	1.62
$\tau \to \mu\nu\bar{\nu}$	1.09
$\tau \to e\nu\bar{\nu}$	0.43
$\tau \to 3hn\pi^o\nu$	0.22
TOTAL	26.46

Table 4.4: *Breakdown of non-ρ background existing in the $\tau^\pm \to \rho^\pm\nu_\tau$ selected events.*

Figure 4.13 shows the fraction of π^o in the $\tau^\pm \to \rho^\pm\nu$ candidates where only one and where more than one neutral cluster is found in the ECAL. This figure shows that two photon separation is possible up to energies of approximately 15 GeV. Figure 4.14 shows that the angle between the track and the nearest neutral cluster is well modeled. A total of 35370 $\tau^\pm \to \rho^\pm\nu$ candidates are selected from the 90-94 τ pair data and 153986 candidates are selected from the τ Monte Carlo. The selection efficiency as estimated by the Monte Carlo is 62.2% with a non-ρ background of 26.5% within the fiducial acceptance of the analysis. The two major sources of background are from $\tau^\pm \to \pi^\pm 2\pi^o\nu$ and $\tau^\pm \to \pi^\pm\nu$ events. Table 4.4 shows the breakdown of the background contributions.

Equations 2.47 and 2.48 can be used to reconstruct the quantities $\cos\theta^*$ and $\cos\psi$ in five equal bins over the region $-0.68 \le \cos\theta \le 0.68$ for all data and Monte Carlo events passing the $\tau^\pm \to \rho^\pm\nu_\tau$ selection. Figure 4.15 shows the reconstructed $\cos\theta^*$ in five bins of reconstructed $\cos\psi$ and summed over the $\cos\theta$ bins. Events whose reconstructed $\cos\theta^*$ are greater than 1 or less than -1 are assigned a value of $\cos\theta^*$=1 and $\cos\theta^*$=-1 respectively. Figure 4.16 shows the ρ selection efficiencies of these quantities. The loss of efficiency at $\cos\psi = 1$ is due to the 400 MeV neutral cluster threshold in the $\tau^\pm \to \rho^\pm\nu_\tau$ selection. Otherwise, the efficiency is approximately uniform over the full acceptance.

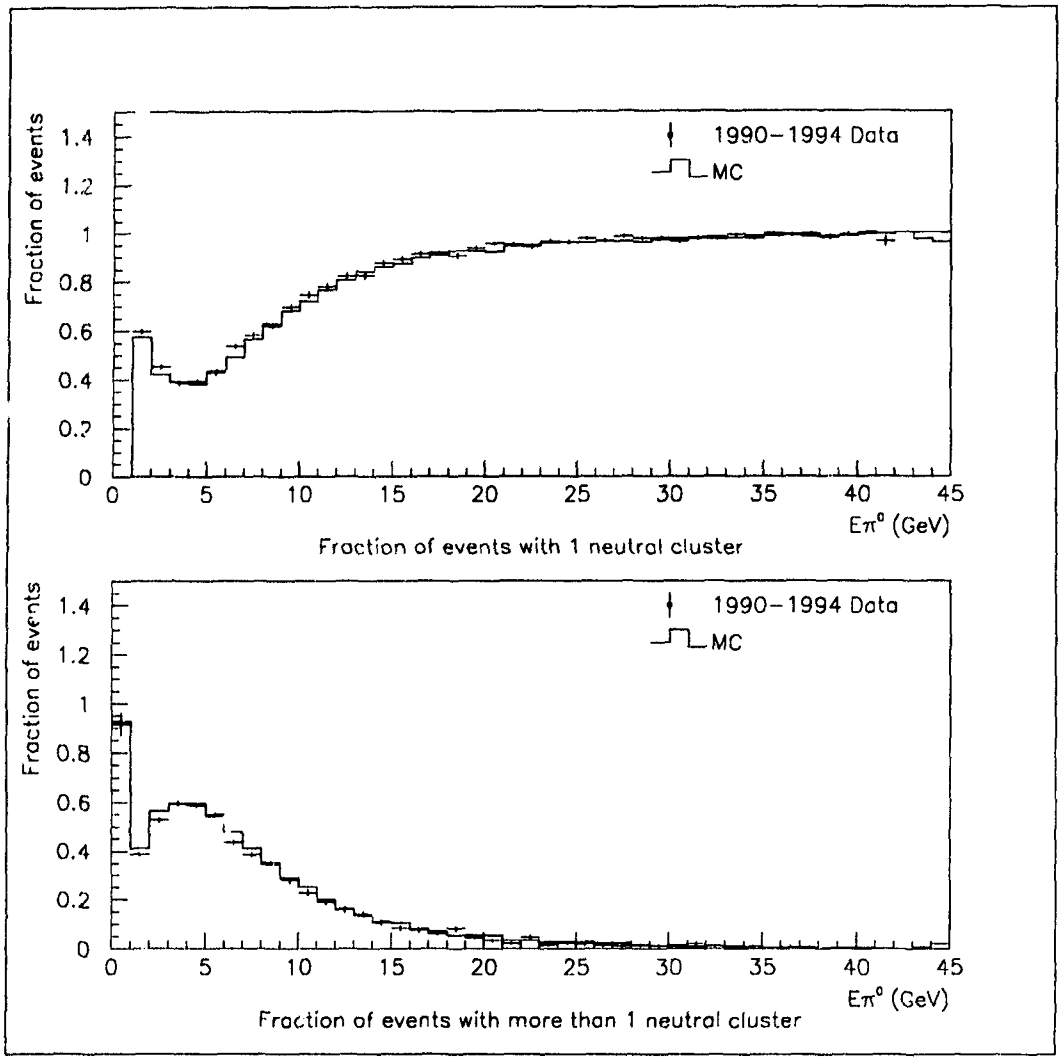

Figure 4.13: *This figure represents the fraction of reconstructed events with one and more than one neutral cluster.*

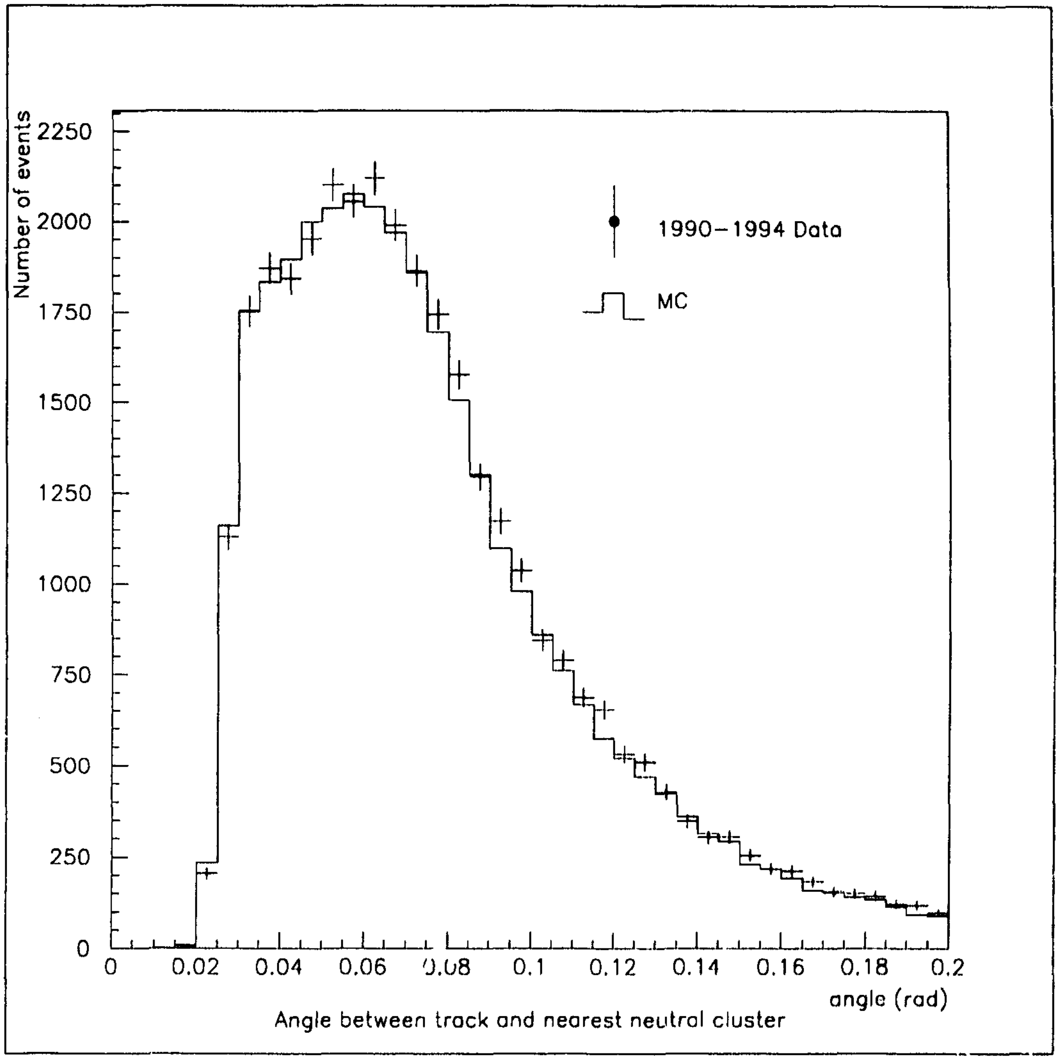

Figure 4.14: *This figure represents the angle between the track and the nearest neutral cluster for both data and Monte Carlo.*

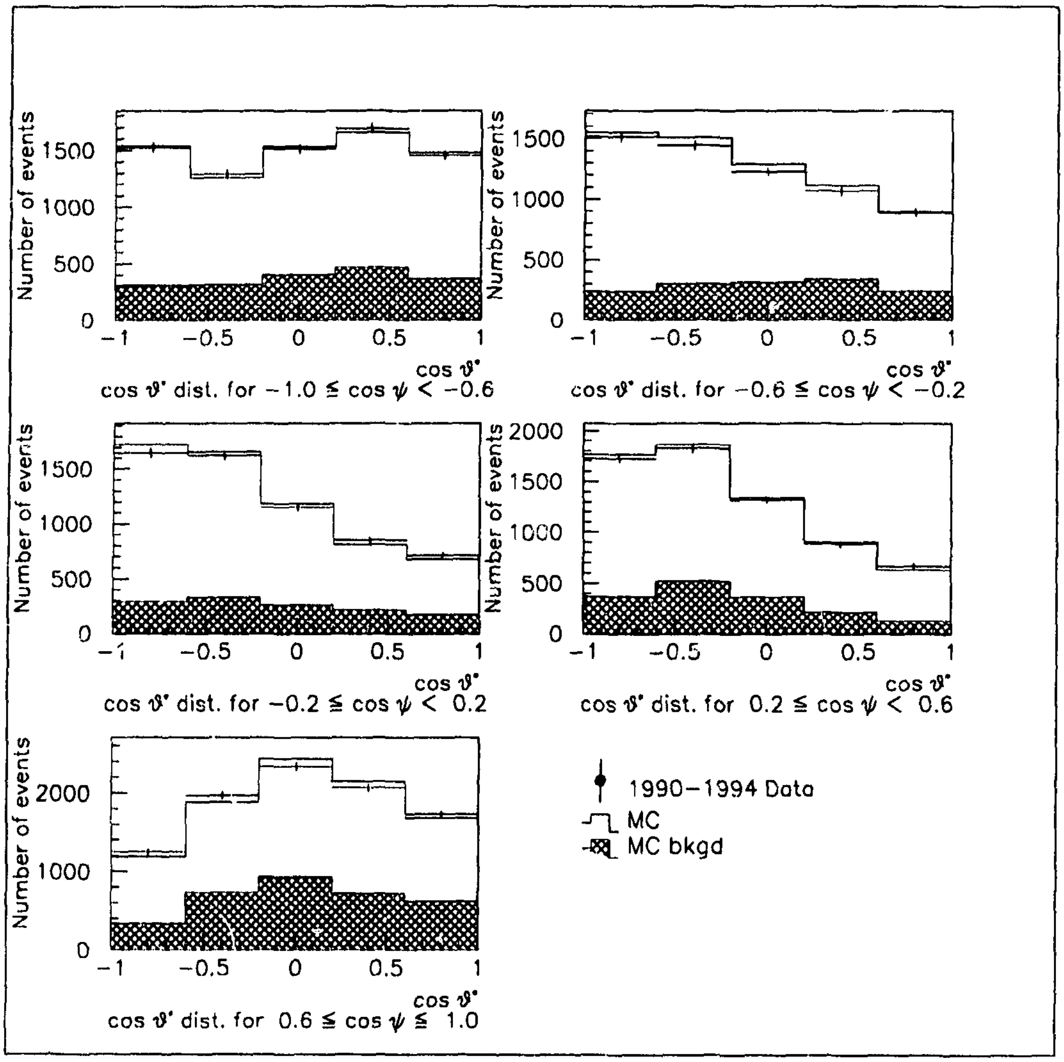

Figure 4.15: *This figure shows the reconstructed quantity* $\cos\theta^*$ *in five bins of reconstructed* $\cos\psi$ *for both data and Monte Carlo* ρ *candidates.*

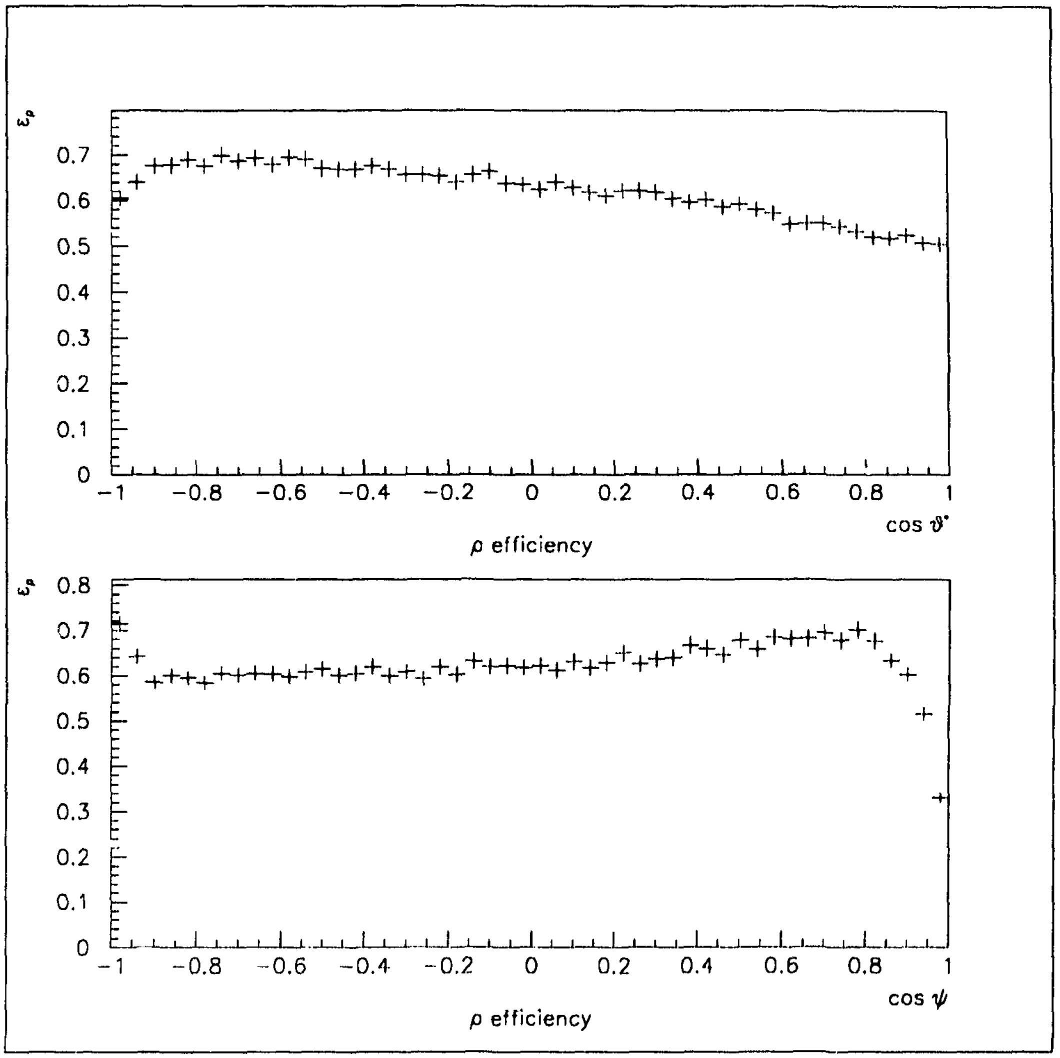

Figure 4.16: *The ρ selection efficiencies are given here as a function of* $\cos\theta^*$ *and* $\cos\psi$.

Chapter 5

A Measurement of $\langle \mathrm{P}_\tau \rangle$ and $\mathrm{A}_{\mathrm{pol}}^{\mathrm{FB}}$

The $\tau^\pm \rightarrow \rho^\pm \nu_\tau$ selection criteria presented in the previous chapter are applied to the OPAL 1990-94 tau data sample and Monte Carlo tau data sample to identify the $\rho^\pm(770)$ resonance. The variables $\cos\theta^*$ and $\cos\psi$ are reconstructed for each selected ρ through the application of equations 2.47 and 2.48. The resulting reconstructed $f(\cos\theta^*, \cos\psi)$ distributions for both data and Monte Carlo are presented in figure 4.15. These distributions represent a sample of the expected distribution given by equation 2.46, $W^\pm(\cos\theta^*, \cos\psi)$. However, equation 2.46 does not take into account the effects of the ρ selection efficiency, non-ρ background, detector resolution effects, or radiation. This chapter demonstrates how to deal with these effects and shows how to calculate the average tau polarization, $\langle \mathrm{P}_\tau \rangle$, from the distribution $f(\cos\theta^*, \cos\psi)_{DATA}$ from the data. $\langle \mathrm{P}_\tau \rangle$ is measured in five equal sized bins in the range $-0.68 \leq \cos\theta \leq 0.68$. The resulting $\langle \mathrm{P}_\tau \rangle$ vs $\cos\theta$ distribution is fitted to the function $P_\tau(\cos\theta)$ in equation 2.14 to determine the average tau polarization and forward-backward polarization asymmetry from the 1990-94 OPAL data sample. Sources of systematic errors to these measurements are considered.

5.1 Extracting $\langle \mathrm{P}_\tau \rangle$ from the Distribution $f(\cos\theta^*, \cos\psi)$

The average tau polarization can be calculated from $\tau^\pm \rightarrow \rho^\pm \nu_\tau$ events through the relation

$$\langle \mathrm{P}_\tau \rangle = \frac{N^{+\rho} - N^{-\rho}}{N^{+\rho} + N^{-\rho}} \tag{5.1}$$

where $N^{\pm\rho}$ are the number of ρ events that decayed from positive/negative helicity taus such that the total number of $\tau^{\pm} \rightarrow \rho^{\pm}\nu_{\tau}$ events is $N^{\rho} = N^{+\rho} + N^{-\rho}$. However, the ρ selection criteria of the previous chapter do not isolate ρ's with a 100% efficiency nor 100% purity nor without detector resolution effects. The number of ρ's selected from positive or negative helicity taus with the selection criteria of the previous chapter, $N^{\pm\rho sel}$, is only a fraction, $\epsilon^{\pm}$, of the total number of ρ's available in the data sample

$$N^{\pm\rho sel} = \epsilon^{\pm} N^{\pm\rho} \qquad \text{where} \qquad N^{+\rho sel} + N^{-\rho sel} = N^{\rho sel}. \tag{5.2}$$

A further problem is that the helicity of the data tau events cannot be measured on an event-by-event basis. Instead, the distribution in $f(\cos\theta^{*}, \cos\psi)$, sensitive to $\langle \mathrm{P}_{\tau} \rangle$, is used to extract the polarization. It is possible to separate the tau helicity states of the Monte Carlo data so the average tau polarization is extracted by comparing the data $f(\cos\theta^{*}, \cos\psi)_{DATA}$ distribution of $\tau^{\pm} \rightarrow \rho^{\pm}\nu_{\tau}$ selected events to linear combinations of positive and negative helicity Monte Carlo $f(\cos\theta^{*}, \cos\psi)_{MC}$ distributions, $f(\cos\theta^{*}, \cos\psi)^{\pm}_{MC}$, of $\tau^{\pm} \rightarrow \rho^{\pm}\nu_{\tau}$ selected events:

$$f(\cos\theta^{*}, \cos\psi)_{DATA} = (1 + \langle \mathrm{P}_{\tau} \rangle) f(\cos\theta^{*}, \cos\psi)^{+}_{MC} + (1 - \langle \mathrm{P}_{\tau} \rangle) f(\cos\theta^{*}, \cos\psi)^{-}_{MC}.$$

The $f(\cos\theta^{*}, \cos\psi)$ distributions are divided into 5×5 bins. The number of selected Monte Carlo ρ's from positive/negative helicity tau events in bin i, j of the $f(\cos\theta^{*}, \cos\psi)^{\pm}_{MC}$ distribution, $(N^{\pm\rho sel}_{i,j})_{rec}$, can be related to the total number of Monte Carlo ρ events generated in that bin, $(N^{\pm\rho}_{i,j})_{4v}$, through the relation

$$(N^{\pm\rho sel}_{i,j})_{rec} = C^{\pm}_{i,j}(N^{\pm\rho}_{i,j})_{4v} \qquad \text{where} \qquad N^{\pm\rho sel} = \sum_{i,j} C^{\pm}_{i,j}(N^{\pm\rho}_{i,j})_{4v} = \epsilon^{\pm} N^{\pm\rho}. \tag{5.3}$$

The distinction is made between the $f(\cos\theta^{*}, \cos\psi)_{MC}$ distribution of ρ events created with the Monte Carlo generator level quantities ($4v$) and the reconstructed quantities of the ρ selection (rec). $C^{\pm}_{i,j}$ is a bin-by-bin correction for ρ efficiency, $e^{\pm}_{i,j}$; non-ρ background, $f^{\pm}_{i,j}$; and detector effects, $d^{\pm}_{i,j}$

$$C^{\pm}_{i,j} = \frac{e^{\pm}_{i,j}}{d^{\pm}_{i,j}(1 - f^{\pm}_{i,j})}. \tag{5.4}$$

- The efficiency, $e^{\pm}_{i,j}$, is the number of selected ρ's in bin i,j which truly are ρ's, $N^{\pm\rho sel}(\rho)_{i,j}$, divided by the total number of ρ's in that bin, $N^{\pm\rho}_{i,j}$:

$$e^{\pm}_{i,j} = \left(\frac{N^{\pm\rho sel}(\rho)_{i,j}}{N^{\pm\rho}_{i,j}}\right)_{4v} . \tag{5.5}$$

- The background, $f^{\pm}_{i,j}$, is the number of selected ρ's in bin i,j which are non-ρ background, $N^{\pm\rho sel}(\overline{\rho})_{i,j}$, divided by the number of selected ρ's in that bin, $N^{\pm\rho sel}_{i,j}$:

$$f^{\pm}_{i,j} = \left(\frac{N^{\pm\rho sel}(\overline{\rho})_{i,j}}{N^{\pm\rho sel}_{i,j}}\right)_{rec} . \tag{5.6}$$

- The detector effects factor, $d^{\pm}_{i,j}$, quantifies the fraction of ρ events which have migrated out of bin i,j due to poor reconstruction:

$$d^{\pm}_{i,j} = \frac{(N^{\pm\rho sel}(\rho)_{i,j})_{rec}}{(N^{\pm\rho sel}(\rho)_{i,j})_{4v}} . \tag{5.7}$$

Substituting $e^{\pm}_{i,j}$, $f^{\pm}_{i,j}$, and $d^{\pm}_{i,j}$ in equation 5.4 yields the bin-by-bin correction which is the number of selected ρ's in bin i,j divided by the total number of ρ's in that bin

$$C^{\pm}_{i,j} = \frac{(N^{\pm\rho sel}_{i,j})_{rec}}{(N^{\pm\rho}_{i,j})_{4v}} . \tag{5.8}$$

Equations 5.1, 5.3, and 5.8 show that the normalized reconstructed $f(\cos\theta^*, \cos\psi)_{MC}$ distribution of selected Monte Carlo $\tau^{\pm} \to \rho^{\pm}\nu_{\tau}$ events in bin i,j is

$$\left(\frac{N^{\rho sel}_{i,j}}{N^{\rho sel}}\right)_{rec} = \left(\frac{N^{+\rho sel}_{i,j}}{N^{\rho sel}}\right)_{rec} + \left(\frac{N^{-\rho sel}_{i,j}}{N^{\rho sel}}\right)_{rec} =$$

$$\frac{\left[(1 + \langle P_{\tau}\rangle)C^{+}_{ij}\left(\frac{N^{+\rho}_{i,j}}{N^{+\rho}}\right)_{4v} + (1 - \langle P_{\tau}\rangle)C^{-}_{ij}\left(\frac{N^{-\rho}_{i,j}}{N^{-\rho}}\right)_{4v}\right]}{(1 + \langle P_{\tau}\rangle)\epsilon^{+} + (1 - \langle P_{\tau}\rangle)\epsilon^{-}} \tag{5.9}$$

where $\left(\frac{N^{\pm\rho}_{i,j}}{N^{\pm\rho}}\right)_{4v} = W^{\pm}_{ij}$ is generated from the $W^{\pm}$ distribution given by equation 2.46 and $\epsilon^{\pm}$ is defined in equation 5.3. The average tau polarization, $\langle P_{\tau}\rangle$, can be extracted from the OPAL data by comparing the reconstructed $f(\cos\theta^*, \cos\psi)_{DATA}$ distribution of the data with that of the Monte Carlo as given in equation 5.9 through a χ^2-like statistic

$$\chi^2 = \sum_{i,j=1}^{5} \frac{\left[\left(\frac{N^{\rho sel}_{i,j}}{N^{\rho sel}}\right)_{DATA} - \left(\frac{N^{\rho sel}_{i,j}}{N^{\rho sel}}\right)_{MC}\right]^2}{\sigma^2_{DATA} + \sigma^2_{MC}}. \tag{5.10}$$

The errors given in the denominator of the expression for χ^2 are derived in appendix B.

The $C^{\pm}_{i,j}$ are calculated from events generated from the KORALZ generator with the full OPAL detector simulation as discussed in the previous chapter. The $W^{\pm}_{i,j} = \left(\frac{N^{\pm\rho}_{i,j}}{N^{\pm\rho}}\right)_{4v}$ are calculated from events also generated with KORALZ including radiative corrections but without detector simulation. Detector simulation is not necessary because the $W^{\pm}_{i,j}$ are generator-level quantities. Tau events without detector simulation are not time consuming to generate so the $W^{\pm}_{i,j}$ are created from a special sample of 10^6 Monte Carlo ρ events thereby reducing the error from the finite size of the Monte Carlo sample.

Tau-pair events which are found to have a $\tau^{\pm} \rightarrow \rho^{\pm}\nu_{\tau}$ decay in both tau jets are each given a weight of one half in the χ^2 statistic.

5.2 Results

The average tau polarization, $\langle P_{\tau} \rangle$, is extracted from the OPAL 1990-94 data set by minimizing the χ^2 of equation 5.10. The on-peak data (at an energy of 91.3 GeV) as well as at ±2 GeV from the Z^0 peak (93.0 GeV and 89.4 GeV) are used to measure $\langle P_{\tau} \rangle$. To gain maximal statistical power, the off peak and on peak data are combined to extract $\langle P_{\tau} \rangle$ given in table 5.1 from the 1990-94 OPAL data set. Approximately the same amount of statistics were taken at both off peak energy points making up only 7 percent of the total data statistics recorded. Therefore, the weighted average of $\langle P_{\tau} \rangle$ over all three energy points can be approximated by the value of $\langle P_{\tau} \rangle$ at the peak energy. The value of $\langle P_{\tau} \rangle$ at the three energy points are combined as if all statistics were taken at the peak energy.

The average tau polarization is also extracted in five equally sized bins in the range $-0.68 \leq \cos\theta \leq 0.68$ also listed in table 5.1. The χ^2 of these fits have probabilities

$\cos\theta$ bin	$\langle P_\tau \rangle$	χ^2/dof
all $\cos\theta$	$-.1235 \pm .0145 \pm .0071$	22.96/24
$-0.680 \leq \cos\theta \leq -0.408$	$-.0195 \pm .0316 \pm .0147$	14.40/24
$-0.408 \leq \cos\theta \leq -0.136$	$-.0344 \pm .0337 \pm .0166$	15.40/24
$-0.136 \leq \cos\theta \leq 0.136$	$-.1506 \pm .0352 \pm .0169$	19.74/24
$0.136 \leq \cos\theta \leq 0.408$	$-.2360 \pm .0327 \pm .0161$	31.88/24
$0.408 \leq \cos\theta \leq 0.680$	$-.1922 \pm .0295 \pm .0137$	27.50/24

Table 5.1: *The resulting $\langle P_\tau \rangle$ and χ^2's per degree of freedom of the data over the entire $\cos\theta$ range are presented in this table. Values are also given in each $\cos\theta$ bin. The first error is data statistics and the second error is Monte Carlo statistics.*

ranging between 15 and 95% indicating that these χ^2 fits are acceptable. The average tau polarization in each of the five $\cos\theta$ bins are plotted in figure 5.1. A χ^2 fit is made to this distribution with the $P_\tau(\cos\theta)$ function of equation 2.14 to extract the $\langle P_\tau \rangle$ and $A_{\text{pol}}^{\text{FB}}$ values of the 1990-1994 OPAL data set

$$P_\tau(\cos\theta) \approx -\left[\frac{\mathcal{A}_\tau(1+\cos^2\theta) + 2\mathcal{A}_e\cos\theta}{1+\cos^2\theta + \frac{8}{3}A^{\text{FB}}\cos\theta}\right] \approx \left[\frac{\langle P_\tau \rangle(1+\cos^2\theta) + 2\left(\frac{4}{3}A_{\text{pol}}^{\text{FB}}\right)\cos\theta}{1+\cos^2\theta + \frac{8}{3}A^{\text{FB}}\cos\theta}\right] \tag{5.11}$$

where $P_\tau(\cos\theta)$ has been rewritten explicitly in terms of $\langle P_\tau \rangle$, $A_{\text{pol}}^{\text{FB}}$, and the forward-backward asymmetry, A^{FB}. The OPAL A^{FB} value is [39]

$$A^{\text{FB}} = 0.0005 \pm 0.0084 \tag{5.12}$$

for the appropriate mixture of on peak and off peak data. The results of the χ^2 fit are

$$\langle P_\tau \rangle = -0.1243 \pm 0.0145 \pm 0.0069 \tag{5.13}$$

$$A_{\text{pol}}^{\text{FB}} = -0.0931 \pm 0.0169 \pm 0.0079 \tag{5.14}$$

where the first error is from data statistics and the second error is from Monte Carlo statistics. The χ^2 per degree of freedom of this fit is 4.03/3. The statistical correlation coefficient of the two measurements is -0.05.

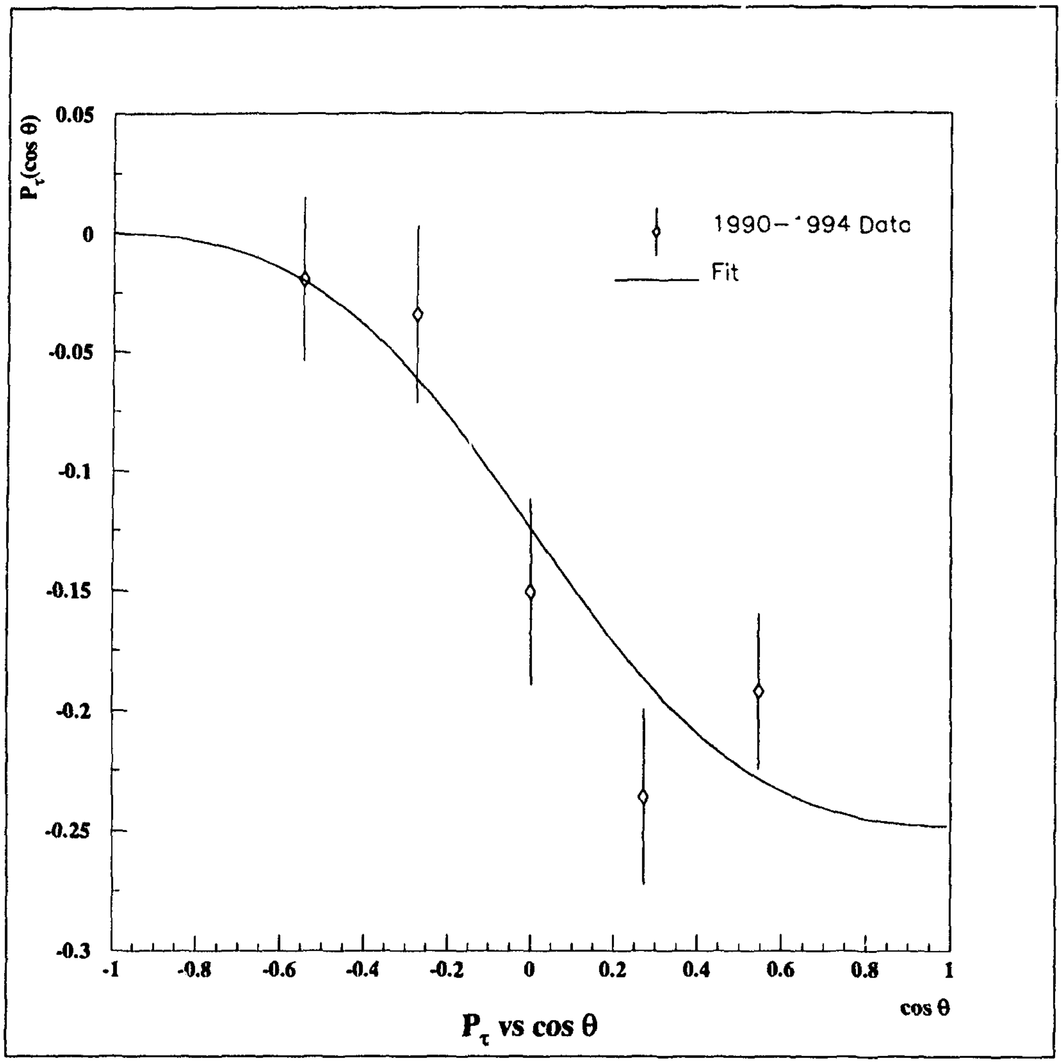

Figure 5.1: *The points are the results of the extraction of* $\langle P_\tau \rangle$ *in the five* $\cos\theta$ *bins. The solid line represents the fit to these points.*

Systematic errors	$\delta < P_\tau >^+$	$\delta < P_\tau >^-$	δA_{pol}^{FB+}	δA_{pol}^{FB-}
MC statistics	.0069	.0069	.0079	.0079
Energy scale	.0044	.0029	.0001	.0018
Energy resolution	.0000	.0006	.0000	.0009
Momentum scale	.0027	.0025	.0000	.0009
Momentum resolution	.0009	.0006	.0004	.0005
Decay radiation	.0000	.0005	.0000	.0006
ρ BR error	.0053	.0056	.0002	.0002
non-ρ BR error	.0080	.0081	.0008	.0007
a_1 shape	.0029	.0025	.0018	.0015
A^{FB} error	.0006	.0006	.0012	.0012
Shower shape	.0020	.0009	.0007	.0005
Total systematic	.0134	.0129	.0083	.0085

Table 5.2: *Contributions to the systematic error on the measurements of* $\langle P_\tau \rangle$ *and* A_{pol}^{FB}.

5.3 Systematic Errors

The systematic errors associated with the measurements of $\langle P_\tau \rangle$ and A_{pol}^{FB} are summarized in table 5.2 and are described below. The systematic errors are summed in quadrature to produce the total systematic error of the measurements.

Detector response

Uncertainties in the energies from the electromagnetic calorimeter of the Monte Carlo data exist due to inadequate modeling of the ECAL energy and its resolution. The energy from the electromagnetic calorimeter is corrected with a $\tau \to e\nu\bar{\nu}$ sample by forcing the Monte Carlo generated ECAL energy associated with the electron divided by the electron momentum (E/p) to match the data as a function of E as discussed in the previous chapter. A systematic error is assigned to this correction by calculating $\langle P_\tau \rangle$ and A_{pol}^{FB} without the correction. The corrected E/p distribution has an uncertainty of 0.3% due to the uncertainty in the track momentum. Hence, a systematic error is assigned to the overall scale of the momentum by varying the Monte Carlo track momentum by ± 0.3% (listed as the "Momentum scale" systematic in table 5.2) and to the overall scale of the ECAL energy by varying the Monte Carlo cluster energies by ± 0.4% to take into account the 0.3% uncertainty in E/p and the 0.28% statistical error associated with the E/p correction. These last two systematic errors are combined in the "Energy scale" entry of table 5.2.

The resolutions of ECAL energies for both data and Monte Carlo were discussed in the previous chapter. A systematic error is assigned by calculating $\langle \mathrm{P}_\tau \rangle$ and $\mathrm{A}_{\mathrm{pol}}^{\mathrm{FB}}$ without any additional smearing to the Monte Carlo energies and is given in the "Energy resolution" entry of table 5.2.

A systematic error is assigned to the tracking resolution by varying by plus and minus one sigma the extra smearing imposed on the Monte Carlo momenta needed to match with the tracking resolution of the data. It is tabulated as the "Momentum resolution" systematic error in table 5.2.

Radiative corrections

The spectra of the τ decay products are affected by initial and final state radiation as well as radiation during the τ decay. Spectra with radiative events (but without detector simulation) for both positive and negative helicity states are generated with the KORALZ 4.0 Monte Carlo generator for the $\tau^\pm \to \rho^\pm \nu$ decay channel. For these radiative corrections, the QED $\mathcal{O}(\alpha)$ corrections to the semi-leptonic τ decays are only included to the leading log approximation. This constitutes the leading uncertainty to the radiative corrections. Hence, a systematic error is assigned to $\langle \mathrm{P}_\tau \rangle$ and $\mathrm{A}_{\mathrm{pol}}^{\mathrm{FB}}$ by taking the difference in the results with and without radiation in the decay of the semi-leptonic modes multiplied by the factor $1/\ln(m_\tau/m_\rho)$ as suggested in reference [40]. This systematic contribution is given in the "Decay radiation" entry of table 5.2.

Background

Each source of non-tau background (electron pair, μ–pair, and multihadronic events) is estimated to be less than 0.2%. A study is made of the effect of the non-tau background on the extraction of the tau polarization. Twenty five events are inserted in the most sensitive area of the distribution $f(\cos\theta^*, \cos\psi)$ (at $\cos\theta^*$=1) and evenly distributed over $\cos\psi$

to see the effect of having non-tau background in the $f(\cos\theta^*, \cos\psi)$ distribution. The difference in the extracted value of the average tau polarization is negligible.

The uncertainties associated with the modeling of the non$-\rho$ background are assessed by varying the τ branching fractions by plus and minus two standard deviations of the measured values (given in appendix A) and summing in quadrature the variations in $\langle P_\tau \rangle$ and A^{FB}_{pol}. The variation of the branching ratios was taken to be two standard deviations to take into account the differences between different measurements of the same branching ratio. These systematic errors are listed in table 5.2 as "ρ BR error" for the variation of the $\tau^\pm \rightarrow \rho^\pm \nu_\tau$ branching ratio and "non-ρ BR error" for the variation of the remaining tau branching ratios. An additional systematic error is assigned due to the uncertainties in the modeling of the $a_1 \rightarrow \pi 2\pi^o$, the major source of background in the $\tau^\pm \rightarrow \rho^\pm \nu$ selection. All a_1 events in the Monte Carlo are reweighted to have a mass and width which are ± 25 MeV/c^2 and ± 100 MeV/c^2 [41] of the nominal values of $m_{a_1} = 1256$ MeV/c^2 and $\Gamma_{a_1} = 599$ MeV/c^2 and the resulting variation in $\langle P_\tau \rangle$ and A^{FB}_{pol} are used as the a_1 modeling uncertainty systematic errors given as "a_1 shape" in table 5.2.

Shower shape

A systematic error is assigned to the inadequate modeling of electromagnetic and hadronic showers in the Monte Carlo. This systematic error is assessed by comparing, for $\tau \rightarrow e\nu\overline{\nu}$ and $\tau \rightarrow \pi\nu$ events, the number of ECAL blocks in both the data and Monte Carlo that have an energy above the block minimum energy threshold of 20 MeV. A better agreement is found for electromagnetic showers if the data threshold is raised to 22 MeV. Hence, the systematic error on electromagnetic shower modeling is the difference in $\langle P_\tau \rangle$ and A^{FB}_{pol} as this data block minimum energy threshold is raised from 20 MeV to 22 MeV. For hadronic showers, better agreement is found if the Monte Carlo minimum block energy threshold is raised to 30 MeV so the difference in results between 20 MeV and 30 MeV is used as the systematic error on hadronic shower modeling These contributions to the systematic error are combined under the heading "Shower shape" in table 5.2.

Other systematic errors

One of the largest systematic errors of this analysis is due to the effect of the limited Monte Carlo statistics used to estimate the efficiencies and backgrounds of the $\tau^{\pm} \rightarrow \rho^{\pm}\nu$ selection on the fit (equation 5.10). This error is assessed by taking the quadratic difference in the errors of $\langle \mathrm{P}_{\tau} \rangle$ and $\mathrm{A}^{\mathrm{FB}}_{\mathrm{pol}}$ with and without σ_{MC} in the denominator of equation 5.10. This error is listed as "MC statistics" in table 5.2.

There is an uncertainty of 0.0084 associated with the forward-backward asymmetry, A^{FB}, used in equation 2.49. A^{FB} is varied in equation 2.49 by plus and minus one standard deviation of its value and given as the "A^{FB}" error in table 5.2.

5.4 Additional Verifications

Three procedures are followed to confirm the validity of the results.

First, the validity of the extraction method is verified. $\langle \mathrm{P}_{\tau} \rangle$ and $\mathrm{A}^{\mathrm{FB}}_{\mathrm{pol}}$ are extracted from each Monte Carlo set as well as from both the positive and negative helicity Monte Carlo events separately. All results are consistent with the expected values for each Monte Carlo set. As well, each Monte Carlo set is used separately to extract $\langle \mathrm{P}_{\tau} \rangle$ and $\mathrm{A}^{\mathrm{FB}}_{\mathrm{pol}}$ from the 1990-94 data sample. The results from using each Monte Carlo set separately are consistent within the Monte Carlo statistical errors. Another test is performed to verify the validity of the fitting procedure. The Monte Carlo is split into 24 equal sized samples. The polarization of each of the 24 Monte Carlo samples is extracted using the full Monte Carlo set. The resulting 24 polarization values (shown in figure 5.2) produce a mean polarization of -0.1346 which is consistent with the value of the polarization of the Monte Carlo (-0.1356 ± 0.0023). Furthermore, the standard deviation of the 24 polarization values ($s = 0.0303$) is consistent with the error on the measurements. $\langle \mathrm{P}_{\tau} \rangle$ and $\mathrm{A}^{\mathrm{FB}}_{\mathrm{pol}}$ are also measured from the 1990-94 data set using the fully reconstructed Monte Carlo set to generate the quantity $C^{\pm}_{i,j}W^{\pm}_{i,j} = \frac{(N^{\pm\rho sel}_{i,j})_{rec}}{(N^{\pm\rho})_{4v}}$ instead of using a separate Monte Carlo with only generator level quantities. The results of the fit are

$$\langle \mathrm{P}_{\tau} \rangle = -0.1219 \pm 0.0161$$

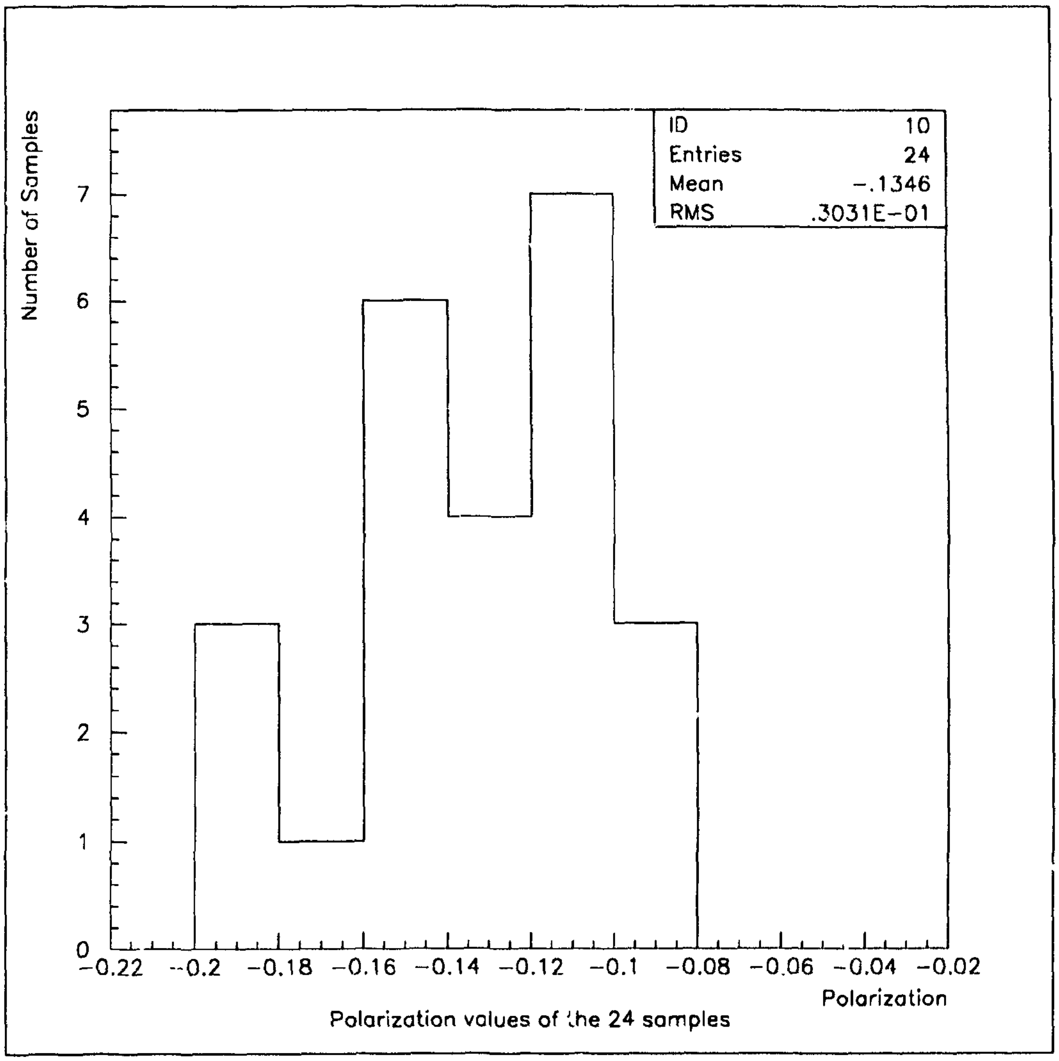

Figure 5.2: *The polarization of each of the 24 Monte Carlo samples is shown in this figure.*

$$A_{pol}^{FB} = -0.0883 \pm 0.0187$$

where both data and Monte Carlo statistics are included in the error. The χ^2 per degree of freedom of this fit is 3.00/3. Finally, the χ^2 criterion of equation 5.10 is combined with $P_\tau(\cos\theta)$ of equation 2.49 to measure $\langle P_\tau \rangle$ and A_{pol}^{FB} in one step instead of the two step procedure described in this chapter. $\langle P_\tau \rangle$ and A_{pol}^{FB} are measured from

$$5 \text{ bins in } \cos\theta^* \times 5 \text{ bins in } \cos\psi \times 5 \text{ bins in } \cos\theta = 125 \text{ bins}$$

resulting in

$$\langle P_\tau \rangle = -0.1250 \pm 0.0161$$

$$A_{pol}^{FB} = -0.0947 \pm 0.0188$$

where both data and Monte Carlo statistics are included in the error. The χ^2 per degree of freedom of this fit is 112.87/123.

Secondly, the consistency of the data is verified. $\langle P_\tau \rangle$ and A_{pol}^{FB} are extracted from the 90-92, 93, and 94 data separately and are shown in figure 5.3 to be consistent with the results from the combined 1990-94 data.

Finally, it is shown that there are no biases in the $\tau^\pm \to \rho^\pm\nu$ selection. The $\tau^\pm \to \rho^\pm\nu_\tau$ selection criteria are varied from their nominal values as listed table 5.3 and the results are shown in figure 5.4. All results of these checks are highly correlated. The data is also split into mostly uncorrelated samples listed in table 5.4 with the results shown in figure 5.5. No biases are seen.

5.5 Summary of the Measurements

This analysis measures the average tau polarization, $\langle P_\tau \rangle$, and the forward-backward polarization asymmetry, A_{pol}^{FB}, from the $\tau^\pm \to \rho^\pm\nu_\tau$ channel of the OPAL 1990-94 tau-pair sample collected at the Z^0 pole. The measured values are

$$\langle P_\tau \rangle = -0.1243 \pm 0.0145 \pm 0.0069^{+0.0115}_{-0.0109} \tag{5.15}$$

$$A_{pol}^{FB} = -0.0931 \pm 0.0169 \pm 0.0079^{+0.0024}_{-0.0031} \tag{5.16}$$

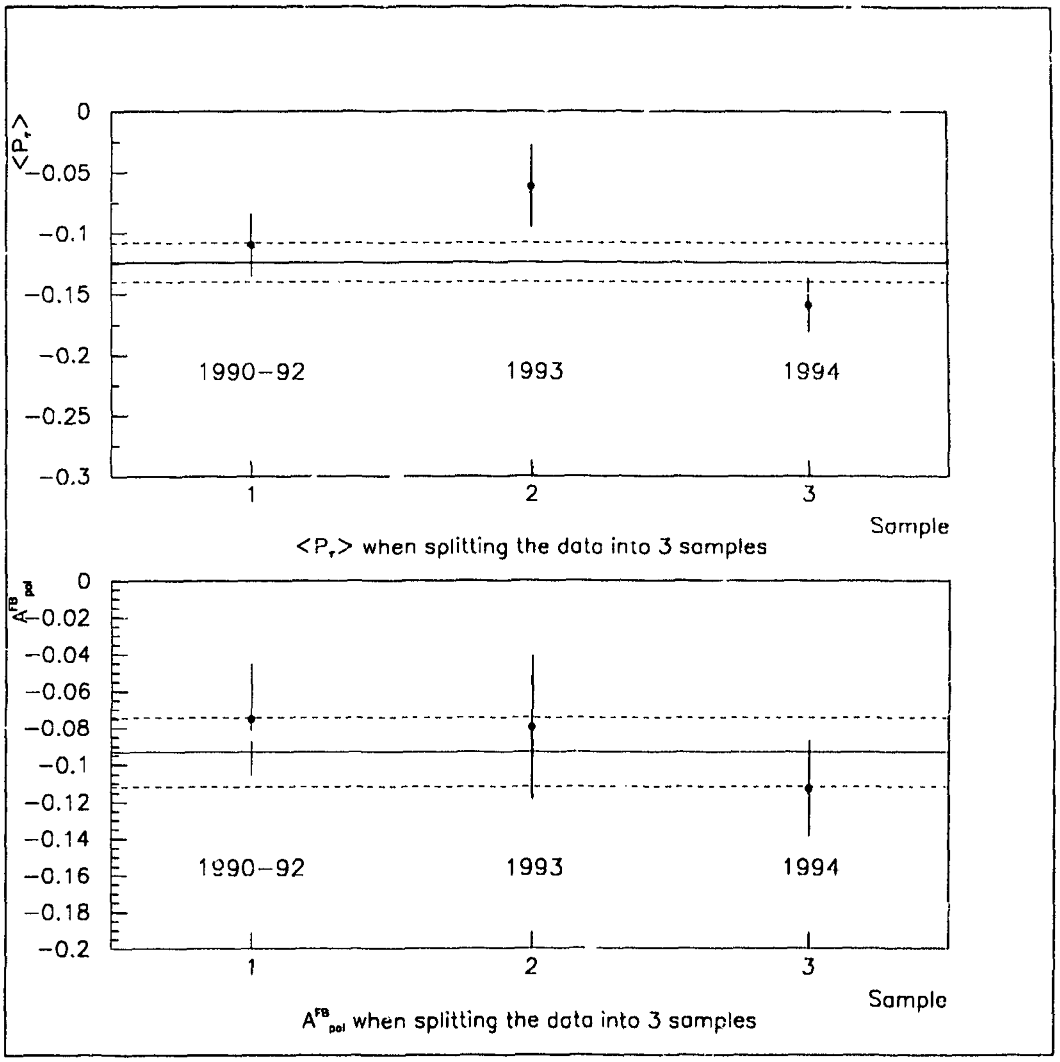

Figure 5.3: *This figure shows* $\langle P_\tau \rangle$ *and* A^{FB}_{pol} *when the data samples are split into 3 sets: 1990-92, 1993, and 1994. The solid lines show the nominal values* $\langle P_\tau \rangle$ *and* A^{FB}_{pol} *extracted from this analysis and the dotted lines show the statistical errors of these values.*

Check number	Systematic check
1	M_{π^0} cut lowered to 0.26
2	M_{π^0} cut raised to 0.30
3	lower M_ρ cut lowered to 0.4
4	lower M_ρ cut raised to 0.7
5	higher M_ρ cut lowered to 1.8
6	higher M_ρ cut raised to 2.2
7	single neutral cluster energy cut lowered to 0.8 GeV
8	single neutral cluster energy cut raised to 1.2 GeV
9	$\cos\theta$ range increased to $\lvert\cos\theta\rvert \leq 0.72$
10	truncate $\cos\theta^*$ at ±1 instead of accepting events with $\lvert\cos\theta^*\rvert > 1$
11	neutral cluster energy threshold lowered to 350 MeV

Table 5.3: *Table of systematic checks used to verify that there are no biases in the $\tau^\pm \to \rho^\pm\nu$ selection. The selection criterion are varied.*

Check number	Systematic check
1	select ρ events with only one neutral cluster
2	select ρ events with more than one neutral cluster
3	select ρ^+ events
4	select ρ^- events
5	select ρ events for which no cluster is associated with the track
6	select ρ events for which a cluster is associated with the track
7	select ρ events only in the first three bins of $\cos\psi$
8	select ρ events only in the last three bins of $\cos\psi$
9	select ρ events in the mass region $0.6 \leq M_\rho \leq 0.728$
10	select ρ events in the mass region $0.728 \leq M_\rho \leq 0.843$
11	select ρ events in the mass region $0.843 \leq M_\rho \leq 2.0$

Table 5.4: *Table of systematic checks used to verify that there are no biases in the $\tau^\pm \to \rho^\pm\nu$ selection. The data is split into mostly uncorrelated sets of samples.*

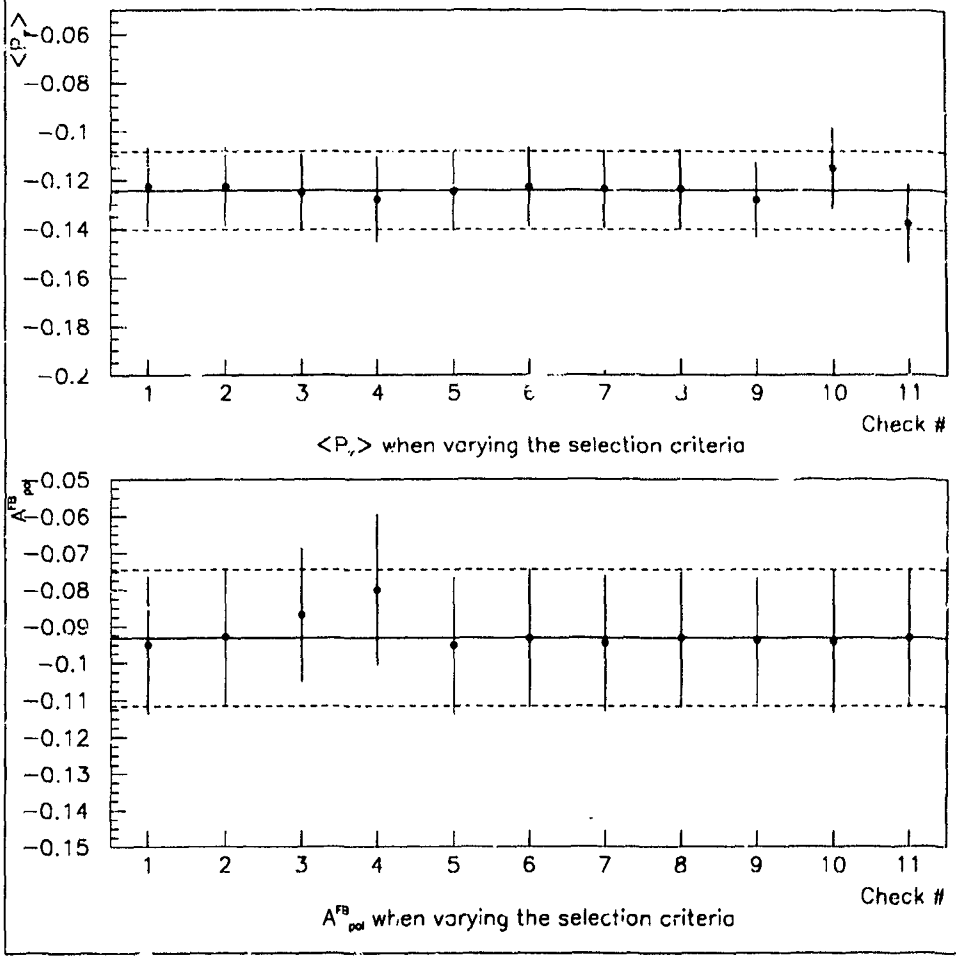

Figure 5.4: *This figure shows* $\langle P_\tau \rangle$ *and* A^{FB}_{pol} *extracted from the from the 1990-94 data sample when the the selection criteria are varied. The solid lines show the nominal values* $\langle P_\tau \rangle$ *and* A^{FB}_{pol} *extracted from this analysis and the dotted lines show the statistical errors of these values. The systematic checks shown in this figure are explained in table 5.3.*

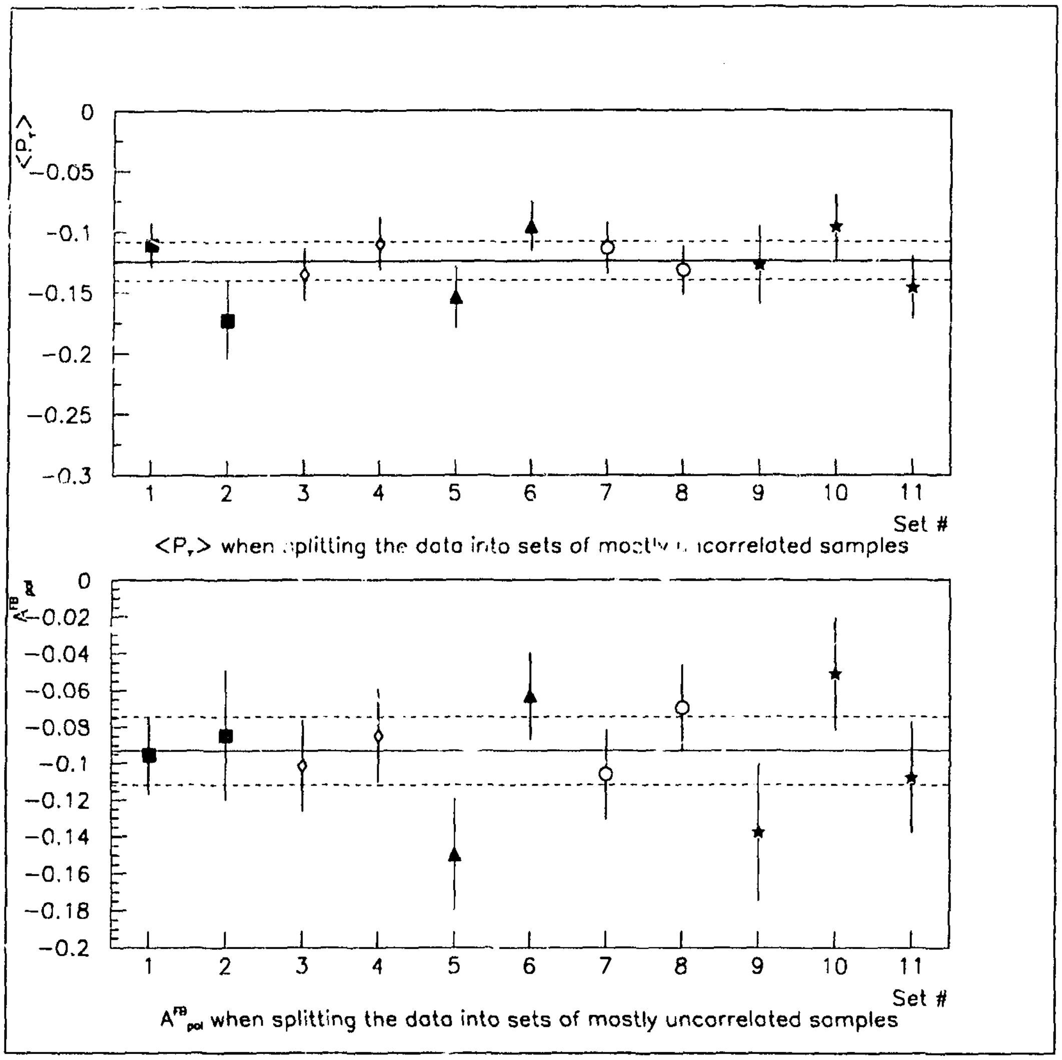

Figure 5.5: *This figure shows* $\langle P_\tau \rangle$ *and* $A_{\mathrm{pol}}^{\mathrm{FB}}$ *extracted from the from the 1990-94 data sample when the the data is split into mostly uncorrelated sets of samples. The solid lines show the nominal values* $\langle P_\tau \rangle$ *and* $A_{\mathrm{pol}}^{\mathrm{FB}}$ *extracted from this analysis and the dotted lines show the statistical errors of these values. The systematic checks shown in this figure are explained in table 5.4.*

where the first error is data statistics, the second error is Monte Carlo statistics, and the third error is an estimate of the systematic errors associated with these measurements. The systematic errors are listed in table 5.2.

Chapter 6

Interpretation of the Results

The average tau polarization, $\langle P_\tau \rangle$, and the forward-backward polarization asymmetry, A^{FB}_{pol}, are extracted from the OPAL 1990-94 $\tau^\pm \rightarrow \rho^\pm \nu_\tau$ data set by comparing the polarization sensitive distribution, $f(\cos\theta^*, \cos\psi)_{DATA}$, to linear combinations of positive and negative helicity tau Monte Carlo $f(\cos\theta^*, \cos\psi)_{MC}$ distributions. At the Z^0 pole, the measured values are

$$\langle P_\tau \rangle = -0.1243 \pm 0.0197 \tag{6.1}$$

$$A^{FB}_{pol} = -0.0931 \pm 0.0189 \tag{6.2}$$

where the errors include both statistical and systematic contributions combined in quadrature. $\langle P_\tau \rangle$ is also measured from the $\tau^\pm \rightarrow \rho^\pm \nu_\tau$ channel by the other LEP collaborations: ALEPH [42], DELPHI [43], and L3 [44]. The polarization measurements are compared in figure 6.1. The $\langle P_\tau \rangle$ extracted from this analysis is currently the best measurement of this quantity. Only this analysis and the DELPHI collaboration quote a measurement of A^{FB}_{pol} from the $\tau^\pm \rightarrow \rho^\pm \nu_\tau$ channel alone with a complete estimation of the associated systematic errors.

Due to its large branching ratio and high sensitivity to the tau polarization, the $\tau^\pm \rightarrow \rho^\pm \nu_\tau$ channel is the most important tau decay in the measurement of $\langle P_\tau \rangle$ and A^{FB}_{pol} as is shown in table 2.2. All LEP collaborations combine measurements of the tau polarization from the following tau decay channels

$$\tau^\pm \rightarrow e^\pm \nu_\tau \nu_e$$

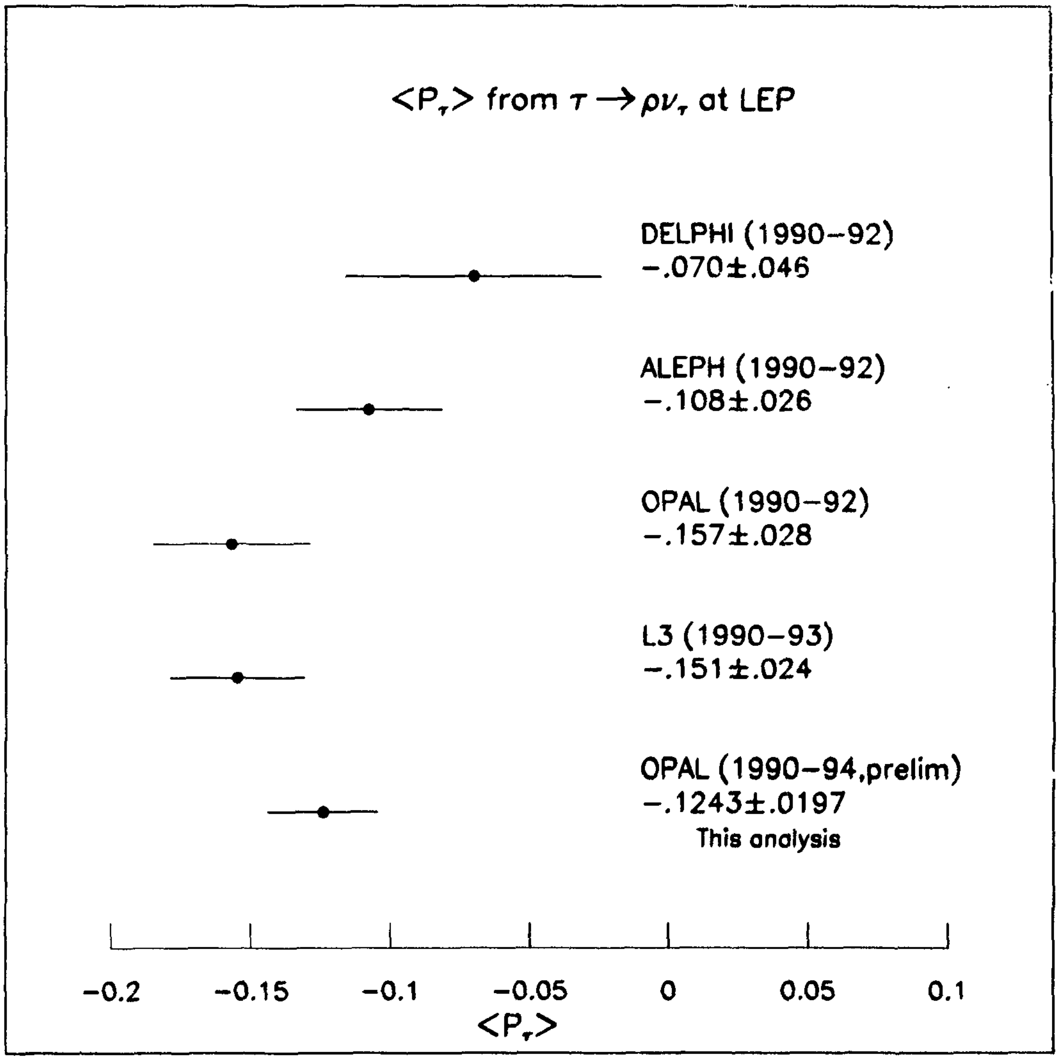

Figure 6.1: *A comparison of the measured* $\langle P_\tau \rangle$ *from the* $\tau^\pm \to \rho^\pm \nu_\tau$ *channel at the* Z^0 *pole by the LEP collaborations ALEPH [42], DELPHI [43], OPAL [45], and L3 [44] with the results of this analysis.*

$$\begin{aligned}
&\tau^{\pm} \longrightarrow \mu^{\pm}\nu_{\tau}\nu_{\mu} \\
&\tau^{\pm} \longrightarrow \pi^{\pm}\nu_{\tau} \\
&\tau^{\pm} \longrightarrow \rho^{\pm}\nu_{\tau} \\
&\tau^{\pm} \longrightarrow a_1^{\pm}\nu_{\tau}.
\end{aligned} \tag{6.3}$$

The results of the $\tau^{\pm} \longrightarrow \rho^{\pm}\nu_{\tau}$ channel from this analysis are used in the OPAL [46] combined measurement of $\langle \mathrm{P}_{\tau} \rangle$ and $\mathrm{A}_{\mathrm{pol}}^{\mathrm{FB}}$ from the channels given in equation 6.3 [47]. The OPAL combined measurements of $\langle \mathrm{P}_{\tau} \rangle$ and $\mathrm{A}_{\mathrm{pol}}^{\mathrm{FB}}$ from the five tau decay channels are

$$\langle \mathrm{P}_{\tau} \rangle = -0.131 \pm 0.013 \tag{6.4}$$

$$\mathrm{A}_{\mathrm{pol}}^{\mathrm{FB}} = -0.098 \pm 0.011 \tag{6.5}$$

where the errors have both statistical and systematic contributions. The combined measurements of $\langle \mathrm{P}_{\tau} \rangle$ and $\mathrm{A}_{\mathrm{pol}}^{\mathrm{FB}}$ made by all LEP collaborations are presented in figures 6.2 and 6.3. The OPAL results are currently the best measurement of these asymmetries.

The Standard Model predicts that $\langle \mathrm{P}_{\tau} \rangle$ and $\mathrm{A}_{\mathrm{pol}}^{\mathrm{FB}}$ are related to the coupling strength of the Z^0 to the tau lepton, $\mathcal{A}_{\tau}$, and the electron, $\mathcal{A}_{e}$, respectively. At the Z^0 pole

$$\langle \mathrm{P}_{\tau} \rangle \approx -\mathcal{A}_{\tau} \qquad \text{and} \qquad \mathrm{A}_{\mathrm{pol}}^{\mathrm{FB}} \approx -\frac{3}{4}\mathcal{A}_{e}.$$

A correction of 0.003 is added to $\mathcal{A}_{\tau}$ and $\mathcal{A}_{e}$ using the ZFITTER package [10] to correct for the effect of the photon propagator, $\gamma - Z^0$ interference, and photonic corrections [46]. This interpretation implies that the values for $\mathcal{A}_{\tau}$ and $\mathcal{A}_{e}$ from this analysis are

$$\begin{aligned}
\mathcal{A}_{\tau} &= 0.127 \pm 0.020 \\
\mathcal{A}_{e} &= 0.127 \pm 0.025
\end{aligned} \tag{6.6}$$

where both statistical and systematic contributions are included in the error. $\mathcal{A}_{\tau}$ and $\mathcal{A}_{e}$ are related to the ratio of the effective vector to axial vector couplings, $\hat{g}_v^{\tau}/\hat{g}_a^{\tau}$ and $\hat{g}_v^{e}/\hat{g}_a^{e}$, through the relationship

$$\mathcal{A}_{\ell} = \frac{2\hat{g}_v^{\ell}/\hat{g}_a^{\ell}}{1 + (\hat{g}_v^{\ell}/\hat{g}_a^{\ell})^2} \qquad \text{where} \qquad \ell = e, \tau.$$

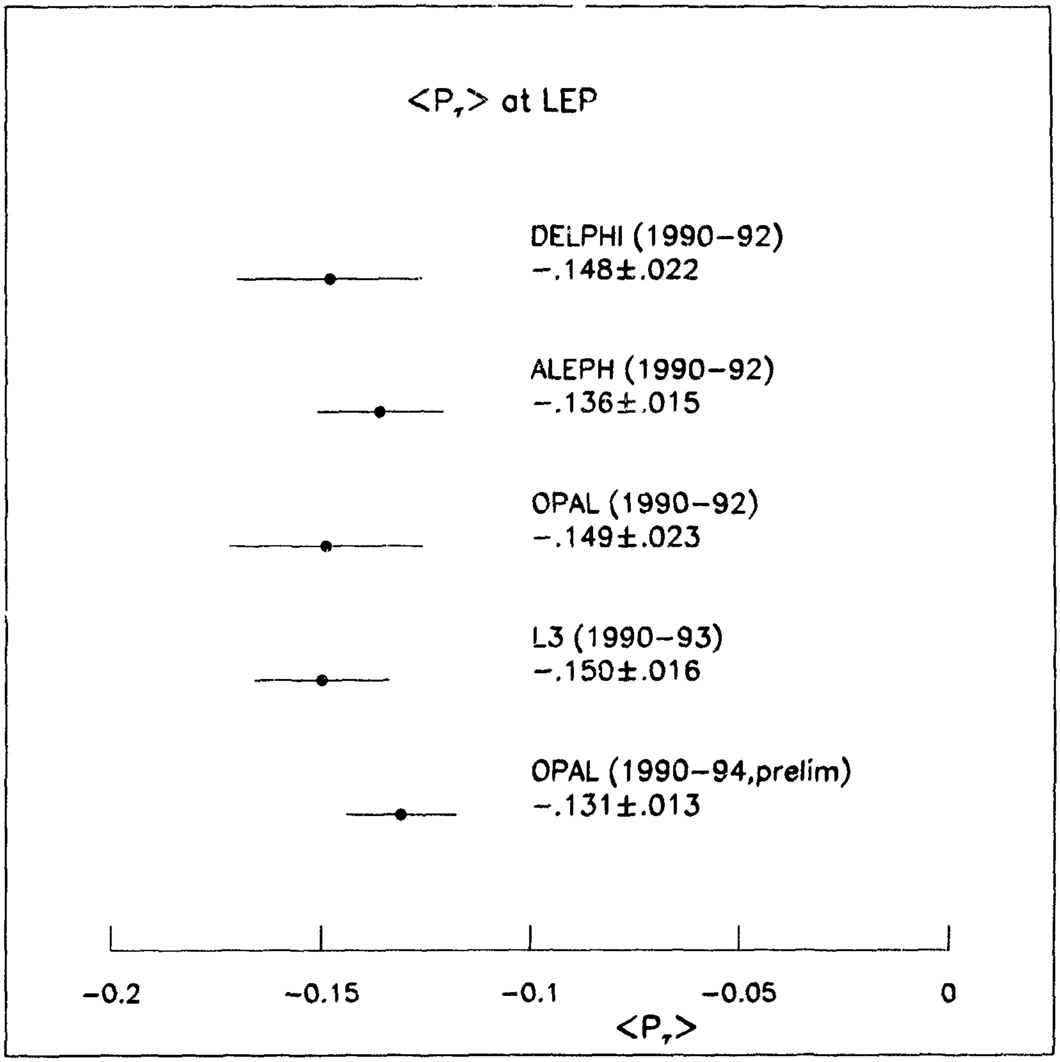

Figure 6.2: *A comparison between the global measurements of* $\langle P_\tau \rangle$ *from the five tau decay channels of equation 6.3 at the* Z^0 *pole by the LEP collaborations ALEPH [42], DELPHI [43], OPAL [45], L3 [44], and OPAL preliminary results [46].*

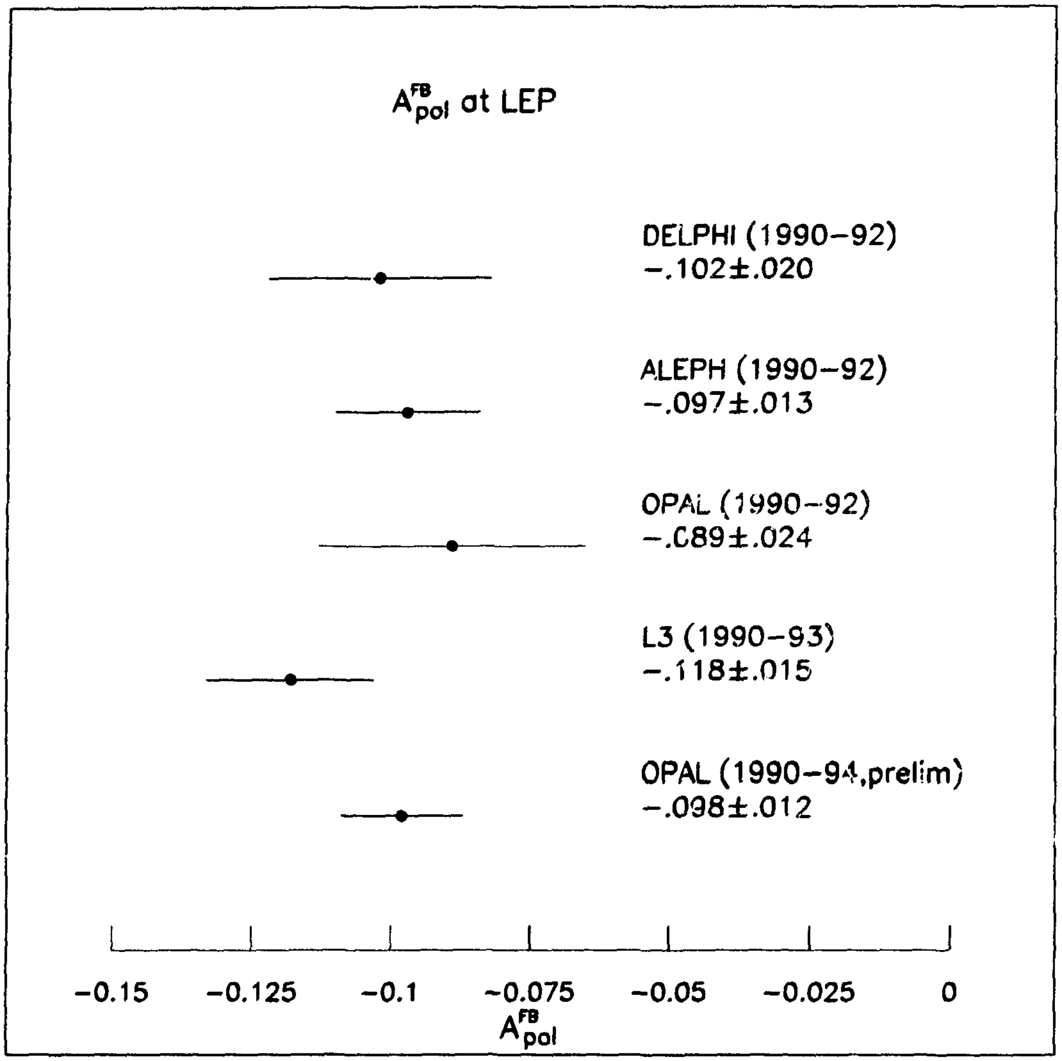

Figure 6.3: *A comparison between the global measurements of* A^{FB}_{pol} *from the five tau decay channels of equation 6.3 at the* Z^0 *pole by the LEP collaborations ALEPH [42], DELPHI [43], OPAL [45], L3 [44], and OPAL preliminary results [46].*

The results from the analysis of the OPAL 1990-94 $\tau^\pm \to \rho^\pm \nu_\tau$ channel are

$$\hat{g}_v^\tau/\hat{g}_a^\tau = 0.0639 \pm 0.0100 \tag{6.7}$$

$$\hat{g}_v^e/\hat{g}_a^e = 0.0639 \pm 0.0127 \tag{6.8}$$

including both statistical and systematic errors. The difference between the results given in 6.7 and 6.8 is

$$\hat{g}_v^\tau/\hat{g}_a^\tau - \hat{g}_v^e/\hat{g}_a^e = 0.0000 \pm 0.0162 \tag{6.9}$$

indicating that lepton universality as measured through the ratio of the vector to axial-vector couplings of neutral currents is valid at the ±0.02 level. $\tau - e$ universality states that the coupling of the Z^0 to electrons should be identical to the coupling of the Z^0 to taus

$$\mathcal{A}_\tau = \mathcal{A}_e \qquad \text{or} \qquad \langle \mathrm{P}_\tau \rangle = \frac{4}{3}\mathrm{A}_{\mathrm{pol}}^{\mathrm{FB}}.$$

Making the substitution $\langle \mathrm{P}_\tau \rangle = \frac{4}{3}\mathrm{A}_{\mathrm{pol}}^{\mathrm{FB}}$ in equation 2.49, the fit of the distribution $P_\tau(\cos\theta)$ is again performed to result in the value for $\langle \mathrm{P}_\tau \rangle$ under the assumption of $\tau - e$ universality. The resulting coupling based on the universality assumption is

$$\mathcal{A}_{\tau-e}(univ) = 0.127 \pm 0.012 \pm .010 \tag{6.10}$$

where both statistical and systematic errors are given. The result of this fit and the value of the ratio given in equation 6.9 show that the assumption of $\tau - e$ universality is valid. The weighted average of $\mathcal{A}_\tau$ and $\mathcal{A}_e$ from the $\tau^\pm \to \rho^\pm \nu_\tau$ channel of this analysis is

$$\mathcal{A}_{\tau-e}(avg) = 0.127 \pm 0.016 \tag{6.11}$$

where both statistical and systematic errors are combined. The value of $\mathcal{A}_{\tau-e}(avg)$ is calculated for each systematic test so that the systematic correlation between the measurements $\langle \mathrm{P}_\tau \rangle$ and $\mathrm{A}_{\mathrm{pol}}^{\mathrm{FB}}$ are taken into account properly. However, the systematic correlation is negligible. It is estimated that the systematic correlation coefficient is less than 0.02. The ratio of the effective vector to axial vector coupling under the assumption of lepton universality is

$$\hat{g}_v^{\tau-e}/\hat{g}_a^{\tau-e} = 0.0639 \pm 0.0080. \tag{6.12}$$

This ratio is related to the effective Weinberg angle, $\sin^2\theta_{eff}^{lept}$, by

$$\hat{g}_v^{\tau-e}/\hat{g}_a^{\tau-e} = 1 - 4\sin^2\theta_{eff}^{lept}.$$

The value for $\sin^2\theta_{eff}^{lept}$ measured from $\tau^\pm \to \rho^\pm\nu_\tau$ channel in this thesis based on a measurement of $\langle P_\tau\rangle$ and $A_{\rm pol}^{\rm FB}$ is

$$\sin^2\theta_{eff}^{lept} = 0.2340 \pm 0.0020. \tag{6.13}$$

A measurement of $\sin^2\theta_{eff}^{lept}$ is made by all LEP collaborations by measuring $\langle P_\tau\rangle$ and $A_{\rm pol}^{\rm FB}$ from the combined tau decay channels of equation 6.3. The resulting $\sin^2\theta_{eff}^{lept}$ are compared in figure 6.4. The average $\sin^2\theta_{eff}^{lept}$ from these measurements at LEP is

$$\sin^2\theta_{eff}^{lept} = 0.2323 \pm 0.0008. \tag{6.14}$$

The effective Weinberg, $\sin^2\theta_{eff}^{lept}$, is measured at LEP using other forward-backward asymmetries such as the b quark, c quark, lepton, and average quark charge forward-backward asymmetries. However, the average tau polarization has the greatest theoretical sensitivity to a measurement of the Weinberg angle as shown in figure 6.5. When all methods of measuring $\sin^2\theta_{eff}^{lept}$ from all four LEP collaborations are combined, the resulting effective Weinberg angle at LEP is [14]

$$\sin^2\theta_{eff}^{lept} = 0.23206 \pm 0.00028^{+0.00008}_{-0.00017}. \tag{6.15}$$

The effective Weinberg angle is also measured at the SLD experiment at SLAC [48] from an evaluation of the left-right asymmetry, A^{LR}. A^{LR}, like $A_{\rm pol}^{\rm FB}$ measures the electron coupling, $\mathcal{A}_e$. The measurement of A^{LR} results in a Weinberg angle of 0.23049 ± 0.00050 [14]. The LEP results combined with the SLAC results measure an effective Weinberg angle of [14]

$$\sin^2\theta_{eff}^{lept} = 0.23166 \pm 0.00025^{+0.00006}_{-0.00013}. \tag{6.16}$$

A consequence of symmetry breaking in a renormalizable theory is that the physics depends on particle masses larger than the energy scale of the observed processes. The

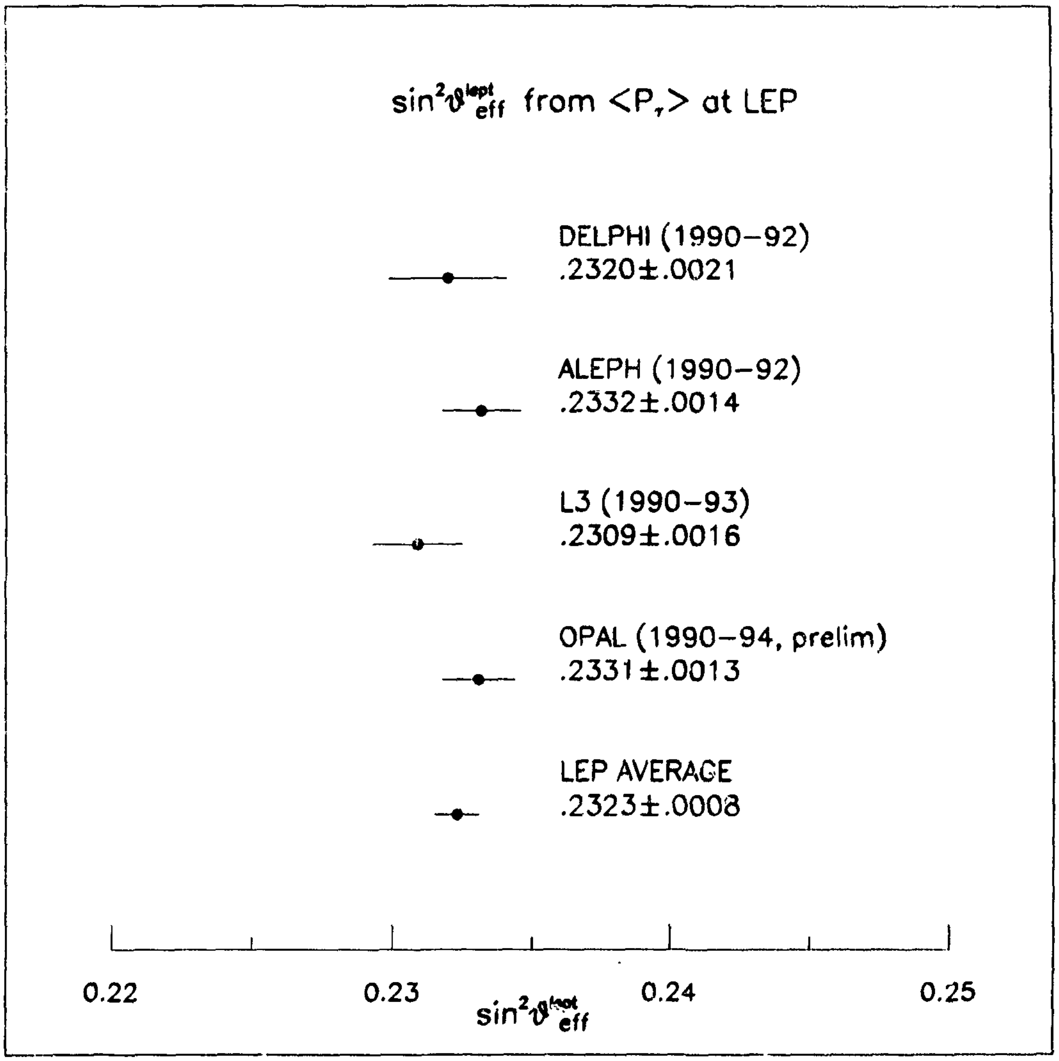

Figure 6.4: *A comparison between the measurements of* $\sin^2\theta^{lept}_{eff}$ *from the five tau decay channels of equation 6.3 at the* Z^0 *pole by the LEP collaborations ALEPH [42], DELPHI [43], L3 [44], and OPAL preliminary results [46].*

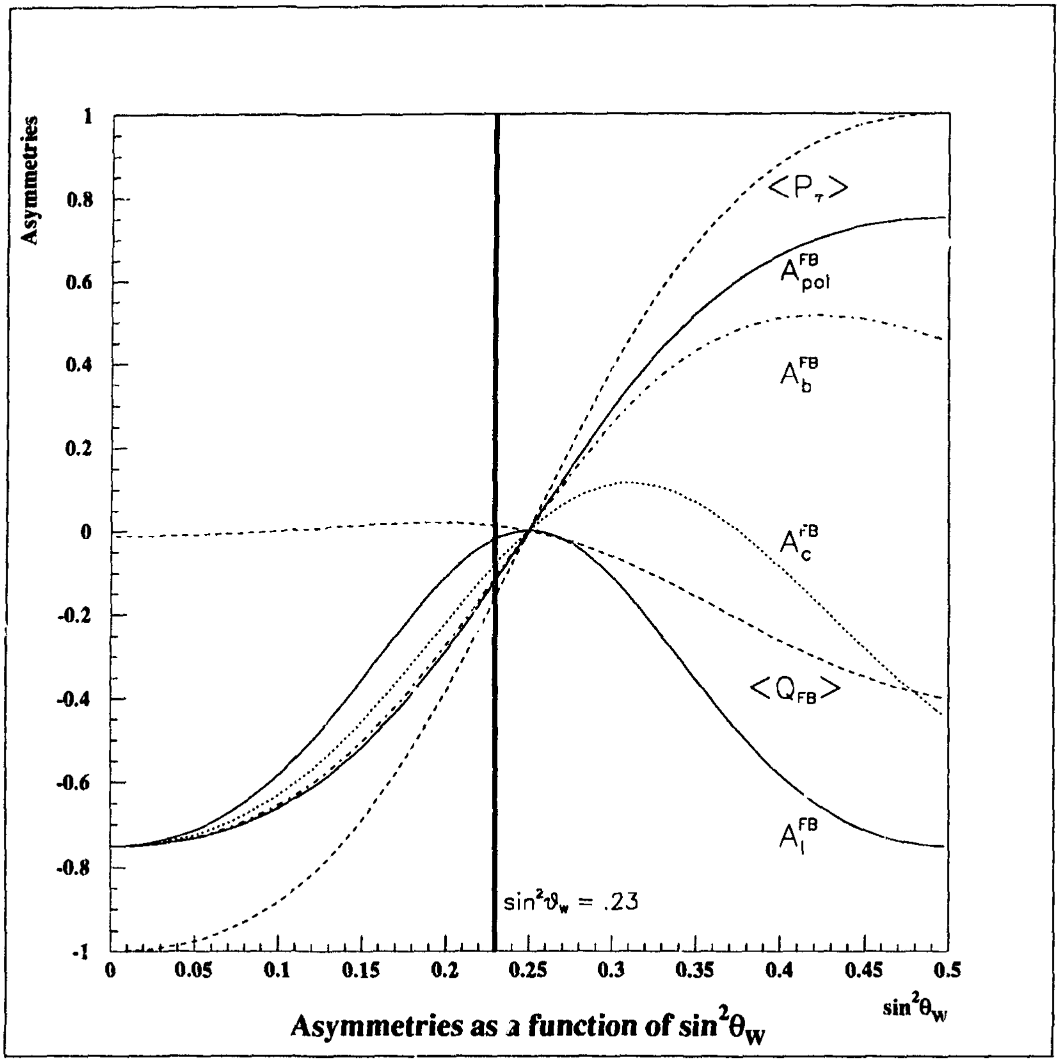

Figure 6.5: *This figure shows the sensitivity of the average tau polarization,* $\langle P_\tau \rangle$*; the forward-backward polarization asymmetry,* A^{FB}_{pol}*; the b quark forward-backward asymmetry,* A_b^{FB}*; the c quark forward-backward asymmetry,* A_c^{FB}*; the forward-backward charge asymmetry,* $\langle Q_{FB} \rangle$*; and the lepton forward-backward asymmetry,* A_ℓ^{FB} *to a measurement of the Weinberg angle,* $\sin^2\theta_W$*. The average tau polarization has the greatest theoretical sensitivity to a measurement of* $\sin^2\theta_W$*.*

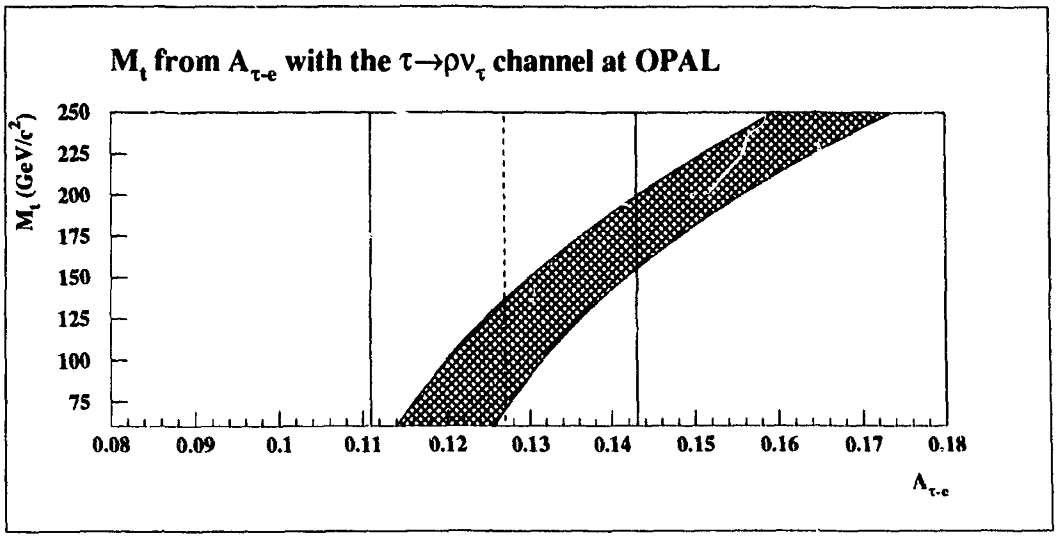

Figure 6.6: *This figure shows the variation of the mass of the top quark,* M_t, *with a measurement of* $\mathcal{A}_{\tau-e}$. *The shaded area shows the electroweak prediction of the top quark mass for a Higgs boson with mass between* 60 *GeV/c*^{2} $\leq M_H \leq$ 1000 *GeV/c*^{2}. *The dotted line shows the measurement of* $\mathcal{A}_{\tau-e}$ *from this analysis while the solid line shows the extend of the one standard deviation error on this measurement.*

LEP electroweak results were used to predict the mass of the top quark, M_t, before the top quark was directly observed by the CDF [15] and D0 [16] collaborations. A measurement of $\mathcal{A}_{\tau-e}$ from a tau polarization measurement with the $\tau^\pm \to \rho^\pm\nu_\tau$ channel as performed using the analysis described here begins to place limits on M_t as shown in figure 6.6. The measurements performed in this analysis are an important part of the measurement by OPAL of the tau polarization from all five decay channels in equation 6.3 which can begin to place a significant upper limit on M_t as shown in figure 6.7a. The combined tau polarization measurements from the LEP collaborations place important lower and upper limits on M_t as shown in figure 6.7b.

Electroweak measurements at LEP and SLAC predict the mass of the top quark to be [14]

$$M_t = 180^{+8+17}_{-9-20}\ \mathrm{GeV/c^2}. \qquad (6.17)$$

The top quark has recently been observed by both the CDF [15] and D0 [16] collaborations

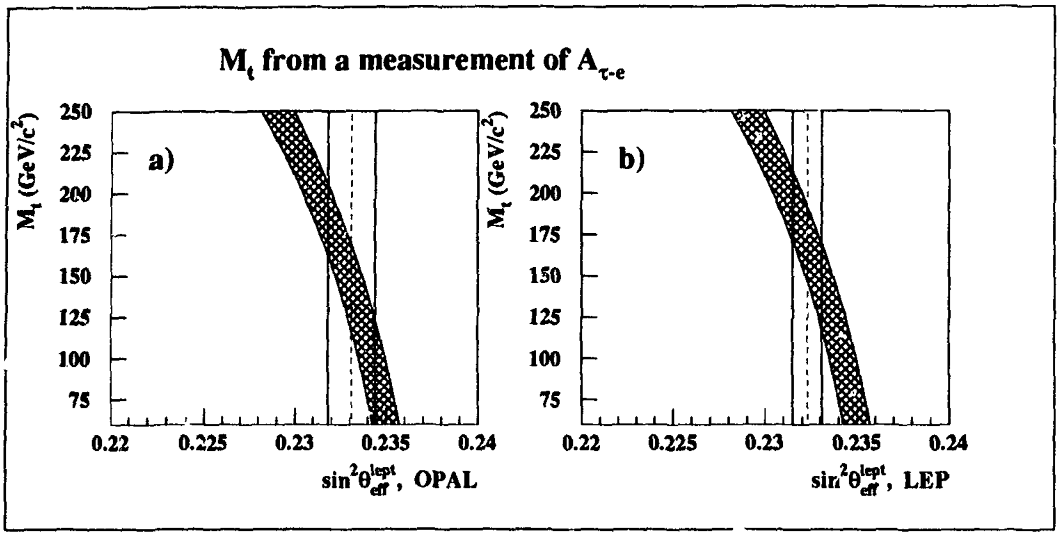

Figure 6.7: *This figure shows the variation of the mass of the top quark, M_t, with a measurement of* $\sin^2\theta^{lept}_{eff}$ *based on measurements of* $A_{\tau-e}$. *The shaded area shows the electroweak prediction of the top quark for a Higgs boson with mass between 60 GeV/c*$^2 \leq M_H \leq 1000$ *GeV/c*^{2}. *The dotted lines show the measurements of* $\sin^2\theta^{lept}_{eff}$ *based on a measurement of* $A_{\tau-e}$ *at a) OPAL and b) LEP while the solid line show the extend of the one standard deviation errors on these measurements.*

with an average mass of [3]

$$M_t = 180 \pm 12\ \mathrm{GeV/c^2} \tag{6.18}$$

in excellent agreement with the electroweak prediction based on the measurements made at LEP and SLAC.

The next step is to use the measured mass of the top quark to extract information about the Higgs boson mass. The electroweak measurements made at LEP in conjunction with the measurement of the mass of the top quark from CDF [15] and D0 [16] have set a limit of 750 GeV/c^2 [14] at the 95 percent confidence level on the mass of the Higgs boson within the context of the Standard Model. The measurements made in this thesis are an important contribution to this indirect limit of the mass of the Higgs boson.

Chapter 7

Conclusion

Parity violating effects of the weak neutral current are presented in this thesis. The ratios of the effective vector to axial-vector couplings of the process $e^+e^- \to \tau^+\tau^-$ are extracted from the decay $\tau^\pm \to \rho^\pm\nu_\tau$ with the OPAL detector at the LEP accelerator by measuring the polarization asymmetries $\langle \mathrm{P}_\tau \rangle$ and $\mathrm{A}^{\mathrm{FB}}_{\mathrm{pol}}$. These measured asymmetries are

$$\langle \mathrm{P}_\tau \rangle = -0.1243 \pm 0.0197 \qquad \mathrm{A}^{\mathrm{FB}}_{\mathrm{pol}} = -0.0931 \pm 0.0189 \tag{7.1}$$

where the errors have both statistical and systematic contributions. The ratios of the effective vector to axial-vector couplings are deduced from these polarization asymmetries

$$\hat{g}^{\tau}_{v}/\hat{g}^{\tau}_{a} = 0.0639 \pm 0.0100 \qquad \hat{g}^{e}_{v}/\hat{g}^{e}_{a} = 0.0639 \pm 0.0127 \tag{7.2}$$

where both statistical and systematic contributions are included in the error. A comparison of these two ratios indicates that lepton universality as measured through the ratio of the vector to axial-vector couplings of weak neutral currents is confirmed at the ±0.02 level. The assumption of lepton universality is used to calculate the weighted average of these ratios

$$\hat{g}^{\tau-e}_{v}/\hat{g}^{\tau-e}_{a} = 0.0639 \pm 0.0080 \tag{7.3}$$

and the effective Weinberg angle

$$\sin^2 \theta^{lept}_{eff} = 0.2340 \pm 0.0020. \tag{7.4}$$

This analysis measures the Weinberg angle with a precision of 0.8 percent. The measurements made in this thesis are an important contribution to the combined determination of the Weinberg angle from the tau polarization at OPAL [46]. This measurement is in excellent agreement with similar measurements made by the other LEP collaborations.

The measurements made in this analysis are combined with other electroweak measurements made at LEP and SLAC [14] to make an indirect measurement of the mass of the top quark

$$M_t = 180^{+8+17}_{-9-20}\ \mathrm{GeV/c^2}, \tag{7.5}$$

which is in excellent agreement with recent direct measurements made at CDF [15] and D0 [16].

This analysis also contributes to the recent estimation of the upper bound on the mass of the Higgs boson of 750 GeV/c^2 at the 95 percent confidence level [14] within the context of the Standard Model.

Appendix A

The Tau Decay Branching Ratios

Tau decay to	MC1508 tau branching ratios	MC1513, 1515, 1516 tau branching ratios	Measured tau branching ratios
$e\nu_e\nu_\tau$	.18250	.17870	.17900 ± .00170
$\mu\nu_\mu\nu_\tau$	.17720	.17330	.17440 ± .00230
$\pi\nu_\tau$	.11730	.11110	.11800 ± .00402
$\pi\pi^o\nu_\tau$	.24160	.25390	.24880 ± .00505
$3\pi\nu_\tau$	.08440	.08930	.07650 ± .00415
$\pi 2\pi^o\nu_\tau$	.09840	.08930	.08955 ± .00403
$K\nu_\tau$	.00840	.00730	.00670 ± .00230
$K^*\nu_\tau \rightarrow K^-\pi^o\nu_\tau$	.00590	.00473	.00520 ± .00070
$K^*\nu_\tau\pi \rightarrow K^o\nu_\tau$	.01170	.00947	.00880 ± .00160
$3\pi\pi^o\nu_\tau$	.05900	.04790	.04910 ± .00633
$\pi \geq 3\pi^o\nu_\tau$	.01220	.01260	.01800 ± .00500
$5\pi\nu_\tau$	.00070	.00108	.00071 ± .00009
$5\pi\pi^o\nu_\tau$	.00070	.00027	.00021 ± .00008
$2K\pi\nu_\tau$		.00108	.00160 ± .00070
$\pi K^o K^{oB}\nu_\tau$		.00108	.00108 ± .00108
$KK^o\pi^o\nu_\tau$		.00009	.00160 ± .00070
$K2\pi^o\nu_\tau$		.00107	.00045 ± .00034
$K2\pi\nu_\tau$		.00570	.00190 ± .00085
$\pi K^{oB}\pi^o\nu_\tau$		.00580	.00190 ± .00085
$3\pi 2\pi^o\nu_\tau$		.00480	.00450 ± .00050
$3\pi 3\pi^o\nu_\tau$		.00027	.00021 ± .00021
$\pi\pi^o 2\gamma\nu_\tau$		.00066	.00066 ± .00012
$\pi\pi^o 3\pi^o\nu_\tau$		.00054	.00054 ± .00010
$\pi\pi^o 2\pi\gamma\nu_\tau$		.00008	.00008 ± .00001
$\pi\pi^o\gamma\nu_\tau$		.00060	.00057 ± .00057
$KK^o\nu_\tau$		.00000	.00290 ± .00120

Table A.1: *Table of the branching ratios of generated tau Monte Carlo events. Also listed are the measured branching ratios from [17] and [3]. The measured branching ratios are reweighted in the analysis to meet the unitarity constraint. The π's and K's with no superscript imply both charge conjugate states.*

Appendix B

Derivation of Errors for the χ^2 Criterion

This appendix gives the derivation of the errors of the χ^2 criterion of equation 5.10.

σ_{DATA} is the binomial error

$$\sigma^2_{DATA} = \left(\frac{N^{\rho sel}_{i,j}}{N^{\rho sel}}\right)_{DATA} \left(1 - \left(\frac{N^{\rho sel}_{i,j}}{N^{\rho sel}}\right)_{DATA}\right) \frac{1}{N^{\rho sel}_{DATA}}.$$

σ_{MC} is found by taking the partial derivative of $\left(\frac{N^{\rho sel}_{i,j}}{N^{\rho sel}}\right)_{MC}$ with respect to $C^{\pm}_{i,j}$ and $W^{\pm}_{i,j}$

$$\sigma^2_{MC} = \left[\frac{1 - \left(\frac{N^{\rho sel}_{i,j}}{N^{\rho sel}}\right)_{MC}}{(1 + \langle \mathrm{P}_\tau \rangle)\epsilon^+ + (1 - \langle \mathrm{P}_\tau \rangle)\epsilon^-}\right]^2 \sum_{+,-} \left[(1 \pm \langle \mathrm{P}_\tau \rangle) C^{\pm}_{i,j} W^{\pm}_{i,j}\right]^2 \times$$

$$\left[\frac{\sigma^2(C^{\pm}_{i,j})}{(C^{\pm}_{i,j})^2} + \frac{\sigma^2(W^{\pm}_{i,j})}{(W^{\pm}_{i,j})^2}\right]$$

where the slight correlation between $C^{\pm}_{i,j}$ and $W^{\pm}_{i,j}$ is ignored. $\sigma(W^{\pm}_{i,j})$ is the binomial error

$$\sigma^2(W^{\pm}_{i,j}) = \left(\frac{N^{\pm\rho}_{i,j}}{N^{\pm\rho}}\right)_{4v} \left(1 - \left(\frac{N^{\pm\rho}_{i,j}}{N^{\pm\rho}}\right)_{4v}\right) \frac{1}{N^{\pm\rho}_{4v}}.$$

$\sigma(C^{\pm}_{i,j})$ is found by explicitly writing the number of selected ρ's in bin (i, j), $(N^{\pm\rho sel}_{i,j})_{rec}$, in terms of signal plus background, $(N^{\pm\rho sel}(\rho)_{i,j})_{rec} + (N^{\pm\rho sel}(\overline{\rho})_{i,j})_{rec}$, where the signal contains ρ events that exist in bin i, j at the four-vector level, $N^{\pm\rho sel}(\rho, unmig)_{i,j}$, and ρ

events which have migrated into bin i,j due to poor reconstruction, $N^{\pm\rho sel}(\rho, mig)_{i,j}$:

$$(N^{\pm\rho sel}_{i,j})_{rec} = (N^{\pm\rho sel}(\rho)_{i,j})_{rec} + (N^{\pm\rho sel}(\overline{\rho})_{i,j})_{rec} =$$

$$N^{\pm\rho sel}(\rho, unmig)_{i,j} + N^{\pm\rho sel}(\rho, mig)_{i,j} + N^{\pm\rho sel}(\overline{\rho})_{i,j}$$

giving the error

$$\sigma^2(C^{\pm}_{i,j}) = \frac{[N^{\pm\rho sel}(\rho, unmig)_{i,j}]_{rec}}{(N^{\pm\rho}_{i,j})^2_{4v}} \left(1 - \frac{[N^{\pm\rho sel}(\rho, unmig)_{i,j}]_{rec}}{(N^{\pm\rho}_{i,j})_{4v}}\right) +$$

$$\left(\frac{[N^{\pm\rho sel}(\rho, mig)_{i,j} + N^{\rho sel}(\overline{\rho})_{i,j}]_{rec}}{(N^{\pm\rho}_{i,j})_{4v}}\right)^2 \left[\frac{1}{(N^{\pm\rho sel}(\rho, mig)_{i,j} + N^{\pm\rho sel}(\overline{\rho})_{i,j})_{rec}} + \frac{1}{(N^{\pm\rho}_{i,j})_{4v}}\right]$$

The error on $C^{\pm}_{i,j}$ dominates over the error on $W^{\pm}_{i,j}$.

Bibliography

[1] D. H. Perkins, *Introduction to High Energy Physics*, Addison-Wesley Publishing Company, Inc. (1987).

[2] F. Halzen and A. D. Martin, *Quarks and Leptons: An Introductory Course in Modern Particle Physics*, John Wiley & Sons (1984).

[3] L. Montanet *et al.*, *Review of Particle Properties*, Physical Review **D50** (1994) 1173 and 1995 off-year partial update for the 1996 edition available on the PDG WWW pages (URL: http://pdg.lbl.gov/).

[4] S. Glashow, *Nuclear Physics*, **B22** (1961) 579.

[5] S. Weinberg, *Physical Review Letters*, **19** (1967) 1264.

[6] A. Salam, & J. C. Ward *Physics Letters*, **13** (1964) 168.

[7] D. J. Griffiths, *Introduction to Elementary Particle Physics*, John Wiley & Sons Inc. (1987).

[8] Z Physics at LEP I: Volume I, ed. G. Altarelli *et al.* **CERN 89-08**.

[9] D. Schaile, *CERN Preprint* **CERN PPE/93-213**.

[10] Results from the ZFITTER program.
D. Bardin *et al.*, *Zeitschrift für Physik* **C44** (1989) 493;
Computational Physics Communications **59** (1990) 303;
Nuclear Physics **B351** (1991) 1;

Physics Letters **B255** (1991) 290;
CERN Preprint **CERN-TH/92-6443**.

[11] H. Burkhart *et al.*, *Zeitschrift fur Physik* **C43** (1989) 497.

[12] R.D. Peccei, Electroweak Interactions, *Proceedings of the Fifth Lake Louise Winter Institute* (Lake Louise,1990), eds. A. Astbury *et al.*, World Scientific (1990) 1.

[13] G. Altarelli *et al.*, *Nuclear Physics* **B369** (1992) 3.

[14] Results presented at the Brussels EPS-HEP conference in July, 1995 and the Beijing Lepton-Photon Symposium in August, 1995.

[15] CDF Collaboration, *Physical Review Letters* **74** (1995) 2626.

[16] D0 Collaboration, *Physical Review Letters* **74** (1995) 2632.

[17] *Proceedings of the Third Worshop on Tau Lepton Physics Montreux, Switzerland*, ed. L. Rolandi, *Nuclear Physics* **B40** (Proc. Suppl.) (1995).

[18] K. Hagiwara *et al.*, *Physics Letters* **B235** (1990) 198.

[19] A. Rougé, Tau decays as polarization analysers, *Workshop on Tau Lepton Physics* (Orsay, 1990), eds. M. Davier and B. JeanMarie, Editions Frontiers (1991) 213.

[20] LEP Design Report, Vol. I **CERN-LEP/TH/83-29**, Vol. II **CERN-LEP/84-01**.

[21] The ALEPH Collaboration, *Nuclear Instruments and Methods* **A294** (1990) 121.

[22] The DELPHI Collaboration, *Nuclear Instruments and Methods* **A303** (1991) 233.

[23] The L3 Collaboration, *Nuclear Instruments and Methods* **A289** (1990) 35.

[24] The OPAL Collaboration, *Nuclear Instruments and Methods* **A305** (1991) 275.

[25] L. Arnaudon *et al.*, *CERN SL Division* **CERN-SL/94-71**.

[26] A. A. Sokolov and I. M. Ternov, *Soviet Physics Doklady* **8** (1964) 1203.

[27] OPAL collaboration, *OPAL Internal Physics Note* **PN126**, March 1994.

[28] S. Jadach *et al.*, *Computational Physics Communications* **64** (1991) 275.
S. Jadach *et al.*, *Computational Physics Communications* **66** (1991) 276 (KORALZ 3.8).
S. Jadach *et al.*, *Computational Physics Communications* **79** (1994) 503 (KORALZ 4.0).

[29] T. Sjöstrand, *Computational Physics Communications* **39** (1986) 347.
M. Bengtsson and T. Sjöstrand, *Computational Physics Communications* **43** (1987) 367.
M. Bengtsson and T. Sjöstrand, *Nuclear Physics* **B289** (1987) 810 (JETSET 7.3 and 7.4).

[30] The OPAL Collaboration, *Zeitschrift fur Physik* **C58** (1993) 387.

[31] M. Bohm *et al.*, *Nuclear Physics* **B304** (1988) 687.
F. A. Berends *et al.*, *Nuclear Physics* **B304** (1988) 712.

[32] J. Allison *et al.*, *Nuclear Instruments and Methods* **A317** (1992) 47.

[33] R. Brun *et al.*, **CERN DD/EE/84-1** (1987).

[34] The OPAL Collaboration, *Zeitschrift fur Physik* **C66** (1995) 543.

[35] A. Astbury *et al.*, *OPAL Internal Technical Note* **TN139**.
R. Sobie, *OPAL Internal Technical Note* **TN186**.

[36] Private Communication with M. Sasaki.

[37] Private Communication with C. Lewis.

[38] M. G. Vincter, *OPAL Internal Technical Note* **TN274**.

[39] Private Communication with T. J. Smith.

[40] E. Barberio, B. van Eijk and Z. Was, *Computational Physics Communications* **66** (1991) 115.

[41] OPAL Collaboration. *Zeitschrift fur Physik* **C67** (1995) 45.

[42] ALEPH Collaboration, *CERN Preprint* **CERN PPE/95-023**.

[43] DELPHI Collaboration, *CERN Preprint* **CERN PPE/95-030**.

[44] L3 Collaboration, *Physics Letters* **B341** (1994) 245.

[45] OPAL Collaboration, *Zeitschrift fur Physik* **C65** (1995) 1-16.

[46] OPAL Collaboration, *OPAL Internal Physics Note* **OPAL PN172** (1995) 1.

[47] These results were presented at the 30th Rencontres de Moriond: Electroweak Interactions and Unified Theories in March 1995, the Brussels EPS-HEP Conference in July 1995, and the Beijing Lepton-Photon Symposium in August 1995.

[48] SLD Collaboration, *Physical Review Letters* **74** (1994) 25.
SLD Collaboration, Contributed Paper to EPS-HEP-95 Brussels.

VITA

Surname: Vincter
Given Names: Manuella Greta
Place of Birth: Lasalle, Quebec, CANADA
Date of Birth: April 3, 1968

Educational Institutions Attended:

University of Victoria, Canada	1990 to 1996
McGill University, Canada	1987 to 1990

Degrees Awarded

B.Sc. (Honours)	McGill University, Canada	1990
M.Sc.	University of Victoria, Canada	1993

Honours and Awards

FCAR Fellowship	1990 to 1992
University of Victoria MacDonnell Award	1990 to 1991
NSERC Postgraduate Scholarship	1993 to 1994
University of Victoria President's Award	1993 to 1994
Graduate Teaching Fellowship	1995

PARTIAL COPYRIGHT LICENSE

Title of Dissertation:

A Precision Measurement of the Ratio of the Effective Vector to Axial-Vector Couplings of the Weak Neutral Current at the Z^{o} Pole

Author ______________________________
Manuella Greta Vincter
March 26, 1996